UNIVERSITY OF CALIFORNIA SAN DIEGO

A 0-D Scaling Approach to the DIII-D L-H Power Threshold in the Presence of Resonant Magnetic Perturbations

A Thesis submitted in partial satisfaction of the requirements for the degree
Master of Science

in

Mechanical Engineering

by

Michael Hanson

Committee in charge:

George Tynan, Chair
Dmitri Orlov, Co-Chair
Alexey Arefiev

2022

The thesis of Michael Hanson is approved, and it is acceptable in quality and form for publication on microfilm and electronically.

University of California San Diego

2022

Dedication

I dedicate this work to my parents, family, and friends. Your guidance, sacrifice, and patience has been invaluable.

Epigraph

So do we continue to consume without sentiment or regret, as nature sometimes teaches us?

Or do we attempt to live in a symbiotic balance with the world, as nature also teaches us?

Caryn Davidson

Table of Contents

List of Figures

List of Tables

Acknowledgements

I would like to acknowledge the co-authors of this work: Dmitri Orlov, Brian Grierson, and the late Todd Evans. Your willingness to support and mentor me has greatly impacted my life.

I would also like to acknowledge the committee members: Dr. George Tynan and Dr. Alexey Arefiev. Dr. Tynan, thank you for your invaluable insight. The PISCES lab and it's scientists have proven to be the spark to my passion for plasma and fusion. Dr. Arefiev, your classes have been my favorite to date. Dr. Orlov, thank you for your years of mentorship and persistence through my growth.

I'd like to acknowledge Brian Sammuli for help with database filtering using TokSearch, Bill Heidbrink, Mike Van Zeeland, and Kathreen Thome for discussions on fast ion losses, Oak Nelson for discussions on RABBIT, Lothar Schmitz for L-H discussion and general guidance, Sterling Smith, Tim Slendebroek, and the OMFIT team for creating an environment to do this work efficiently, and many others for fruitful conversations that furthered this project.

ABSTRACT OF THE THESIS

A 0-D Scaling Approach to the DIII-D L-H Power Threshold in the Presence of Resonant Magnetic Perturbations

By

Michael Hanson

Master of Science in Mechanical Engineering

University of California San Diego, 2022

Professor George R. Tynan, Chair

Dr. Dmitri Orlov, Co-chair

We report a DIII-D database study of the H-mode power threshold over a wide range of plasma conditions and in the presence of resonant magnetic perturbations (RMPs). This database consisting of global (i.e. averaged) quantities is first compared to the 2008 ITPA database and the resulting L-H power scaling [38]. Since ELM control is critical for ITER, and applied 3D fields will likely be present prior to the transition into the H-mode, this study is important for assessing the impact of RMP ELM suppression on the L-H power threshold. The L-H transition has been studied extensively and is dependent on the physical and magnetic divertor geometry, shear flows, and drifts, among other parameters, some of which are altered by RMP fields. In

order to understand the effects of RMPs on the L-H threshold, we attempt to make a robust empirical model, using only DIII-D data, that includes magnitudes and the toroidal modes of various resonant and non-resonant 3D fields. In addition, we assess the validity of previous assumptions about fast ion losses, as well as the usefulness of 0-D database regressions for extrapolation to ITER. Results from this database study show the standard 0-D parameters to be insufficient for capturing the complex L-H transition physics at a level high enough to provide an extrapolation to ITER with reasonable certainty.

Motivation

If humans are to remain on the earth and retain some resemblance of our current comforts, many things will have to change. Among those things, a carbon-free energy source must be developed to meet the exponential growth of the world's energy demand. The Energy Information Administration (EIA) provides data on historical and projected energy consumption. Using this data, US energy consumption shows a growth rate of ~3% per year [1]. This growth translates to a doubling of energy consumption approximately every 10 years. Investments in renewable technology and subsidies in their applications have resulted in their rapid adaptation to the global energy supply. Many of these renewable sources, unfortunately, are subject to varying weather patterns, and with energy storage technology lagging behind the energy supply, there still exists a need for baseline dispatchable power production. Excluding carbon-producing sources like coal, nuclear fission is a possible supplier but faces many socioeconomic barriers. Nuclear fusion, however, is currently unburdened by these barriers. With its high power density, abundant fuel that is nearly limitless on humanity's timescale, and low-level, relatively short-lived nuclear waste, fusion energy will be a crucial piece of our future energy portfolio.

Introduction

Nuclear Fusion

Fusion is the process by which the nuclei of two atoms combine into a single heavier particle. For particles heavier than Fe^{56}, this process requires more energy than it releases. However, in elements lighter than Fe^{56}, this process releases energy. Future nuclear fusion plants will focus on fusing nuclei lighter than Fe^{56}, and more specifically, the Deuterium-Deuterium (D-D) and Deuterium-Tritium (D-T) reactions. These two reactions are the focus of future plants due to the relative ease of the reaction and the large release of energy produced in the fusion. The reaction equations for both D-D and D-T fusion are shown below [2**]**.

$$D + D \rightarrow \ 3He + n + 3.2\ MeV \text{ (1.a)}$$

$$D + D \rightarrow T + p + 4.0\ MeV \text{ (1.b)}$$

$$D + T \rightarrow \ 4He + n + 17.6\ MeV \text{ (1.c)}$$

This excess energy on the right-hand side of equations 1.a/b/c can be traced back to the mass differences of the reactants and products. With the reactants being more massive than the products, the difference in mass is converted to energy via $E = \Delta mc^2$, with Δm being the mass difference and c being the speed of light. These nuclei must first overcome the Coulomb barrier before the strong nuclear force can take over and fuse the two. For hydrogen particles, this typically means they must have an energy of ~1 MeV [3]. With the ionization energy for hydrogen and its isotopes on the order of tens of eV, the fuel for these reactions is fully ionized and in the plasma state [3]. Plasma at the relevant energies for fusion (hundreds of millions of kelvin) cannot be contained by any known material without destroying it. Therefore, fusion

reactors can exploit the charged nature of the particles and use magnetic fields to manipulate and confine the plasma.

Lawson Criterion

The ability of a fusion device to produce net fusion energy can be gauged by the Lawson Criterion, also known as the fusion triple product [4]. This fusion triple product is a product of three quantities: the energy confinement time τ_E , density n, and temperature T. Lawson established that the product of n, T, and τ_E must reach a minimum threshold to release more energy than it consumes. This value also allows for the comparison between the power gained through the thermonuclear reactions and the power lost to the environment through various avenues. Once a threshold (the criteria) is exceeded, the plasma produces more power through these fusion reactions than is lost to the environment. This criterion is different based on the fuel being used and the temperature of the species.

The reaction with the lowest criteria for net energy production in magnetic fusion device (i.e. tokamaks. See following section) relevant temperature range of 5 – 20 keV is the Deuterium-Tritium reaction. This minimum occurs at a temperature of 14 keV with a triple product value of $\sim 3 * 10^{21} \frac{keVs}{m^3}$ [3]. Tritium is a radioactive isotope with a half-life of ~12.5 years and must be produced through presently expensive and potentially controversial means [5]. Future goals are to pivot to a D-D reactor, but due to the decrease in cross-section, this reaction will prove to be much more difficult. The current triple product record comes from a D-D plasma at the JT-60 tokamak and sits at $\sim 1.5 * 10^{21} \frac{keVs}{m^3}$ [6], which is still over an order of magnitude lower than needed for breakeven using the D-D fuel criteria. Currently, tokamaks are the most well-understood (and well-funded) magnetic confinement scheme. Tokamaks became the focus

of research efforts after the T3 tokamak became the first device to reach electron temperatures of 1 keV in 1969 [7].

The Tokamak

The largest currently operational magnetic confinement device in the United States is the DIII-D National User Facility, an Office of Science user facility operated by General Atomics in San Diego, California. DIII-D is one in a series of experimental devices, including but not limited to ASDEX in Germany, JET in the UK, JT-60SA in Japan, KSTAR in Korean, and EAST in China, serving to establish the scientific basis for future devices like ITER (est. 2025) and SPARC (est. 2025), which are discussed in the next section [8]. A tokamak is a "magnetic bottle" that uses helical magnetic fields, produced through a combination of an externally applied toroidal component and a poloidal component produced by the plasma current, to confine plasma away from the walls of the device. These helical fields work to cancel vertical ∇B drifts that are a result of the toroidal geometry and that would otherwise cause the plasma to drift out of the device. In the center of the toroid, there is a solenoid that is used to drive current in the plasma through transformer action by inducing an electro-motive force (EMF). This EMF initially breaks down the gas to form a plasma before continuing to ohmically heat and drive current in the plasma (Ip) up to a point where ohmic heating is no longer possible. A general schematic of a tokamak is shown in figure 1, and a poloidal cross-section of DIII-D is shown in figure 2 to give an idea of a potential magnetic equilibrium.

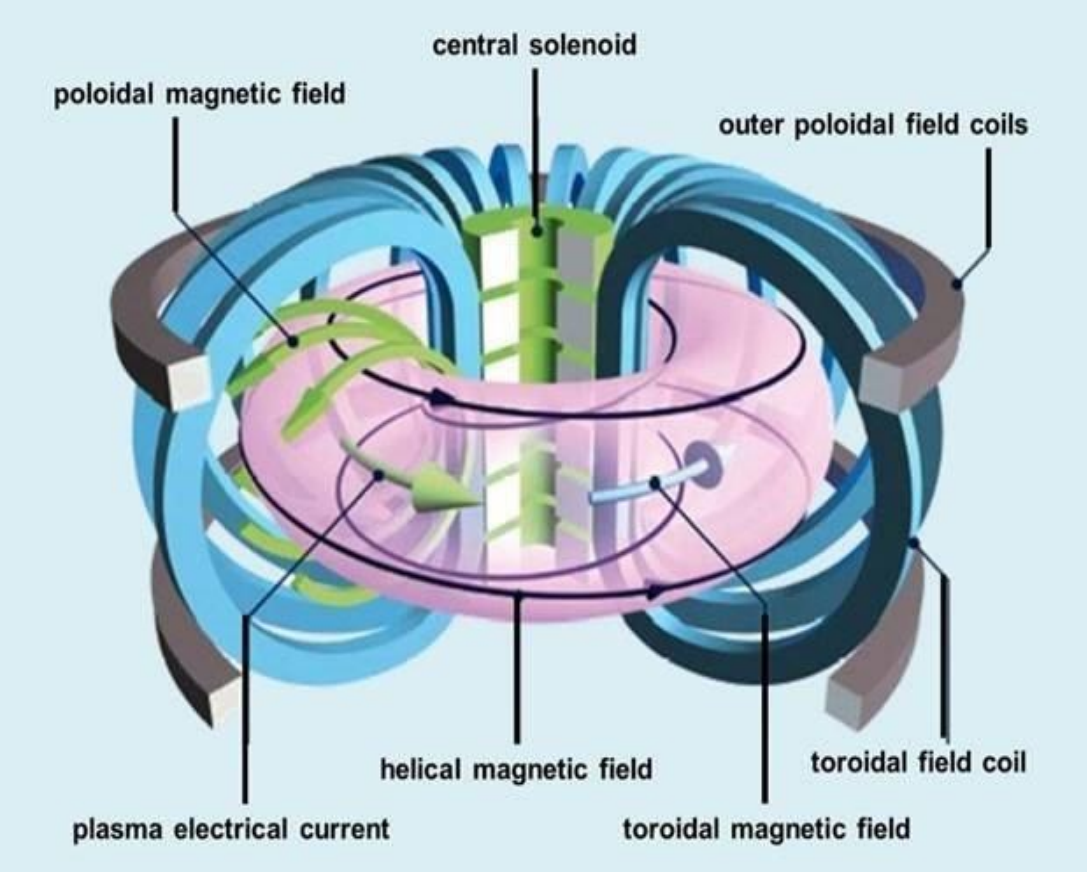

Figure 1: General schematic of a tokamak showing the toroidal and poloidal field coils in blue and gray, respectively. The central solenoid is shown in green, with the total helical magnetic field shown in black. Courtesy of EUROfusion.

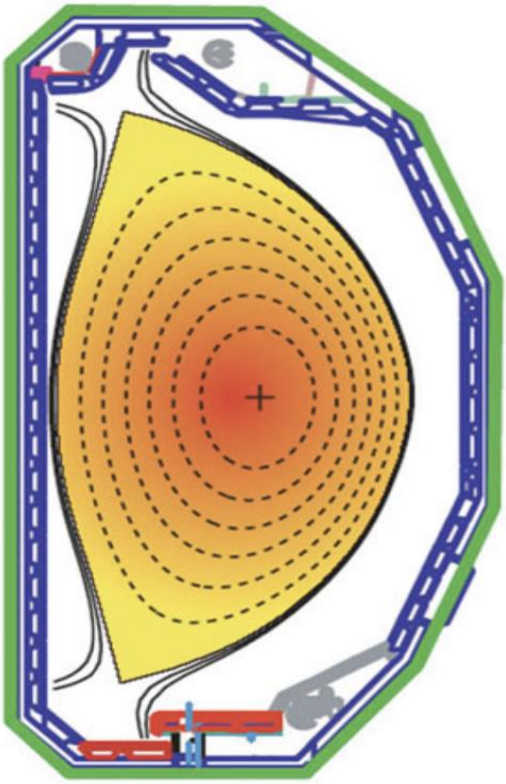

Figure 2: Poloidal cross-section of the DIII-D tokamak in a "double-null" configuration. The dashed lines are magnetic flux surfaces, and the cross is the magnetic axis.

Future Tokamaks

ITER is a tokamak being built in France and represents the largest international scientific endeavor in history, with 35 countries participating in its construction. The goal of ITER will be to demonstrate a fusion gain of Q=10 (Q=fusion power/input power). This has the possibility to be the first example of net fusion energy, producing 500 MW from 50 MW of input, and is set to do so sometime after 2035 [9]. SPARC, on the other hand, is a compact, high-field tokamak currently under construction by Commonwealth Fusion Systems and similarly looks to be the first to produce net fusion power, with a projected gain of Q=11 [10]. Future fusion power plants, built on the lessons learned from devices like SPARC and ITER, will operate with a

"burning" plasma with densities and temperatures well above any existing device. In burning plasmas, the heating from the alpha particles (as a result of the fusion reactions) is sufficient to replace the power lost through radiation and conduction and, therefore, is self-sustaining. Since a future fusion power plant would need to operate in or near this regime to account for various losses in the energy-producing process, increasing the triple product is an important research goal.

The High Confinement Mode

In tokamaks, the focus is on achieving high temperatures while operating at relatively low densities when compared to inertial schemes. In 1998, an empirical limit on the density in tokamak plasmas was determined using a database analysis similar to the one done in this thesis [11]. This "Greenwald limit", $n_G = \frac{I_P}{\pi a^2}$, is a dimensional quantity that defines a maximum for the line-averaged electron density in tokamaks. Here, n_G is the density in $10^{20} m^{-3}$, I_P is the plasma current in MA, and a is the minor radius in m. Above this limit, the plasma will become unstable and potentially disrupt. Therefore, for a tokamak fusion reactor, with the temperature set by the maximum of the reactivity and the density limited by the Greenwald equation, the energy confinement time is the only remaining variable to increase. The energy confinement time is a measure of the rate at which the device loses energy through the separatrix.

One way to increase τ_E is by operating in the high confinement mode. When magnetically confined plasmas are heated past a threshold heating power level, they can transition from a low confinement (L) mode to a high confinement (H) mode in a process referred to as the L-H transition. The H-mode was first discovered in 1982 at ASDEX and later created in Doublet III in 1986 [12,13]. H-mode plasmas are characterized by an increase in the

energy confinement time, usually by a factor of two, when compared to their L-mode counterparts. This increase in confinement is due to the formation of an edge transport barrier. However, the same process that results in better confinement for H-modes comes at a price. Due to the reduced heat and particle transport, pressure gradients grow at the edge until a limit is reached and the gradient collapses, releasing a burst of heat and particles, referred to as an edge-localized mode (ELM). In current experimental devices, these ELMs are of a manageable size and do not significantly erode plasma facing components (PFCs). When scaled up to an ITER-like machine, however, they will be large enough to damage the wall and divertor, depositing as much as 20 MJ per ELM [14].

Resonant Magnetic Perturbations

Externally applied 3D magnetic fields and, more specifically, resonant magnetic perturbations (RMPs), are one way to control these ELMs and reduce the heat flux to the plasma-facing components [15]. Non-axisymmetric magnetic perturbations are a small disturbance of the assumed axisymmetric magnetic field. When they have the same pitch as a target rational magnetic surface, they are said to be resonant. This pitch is defined as $q= m/n$ where m is the number of poloidal transits and n is the toroidal transits before a magnetic field line reconnects with itself. There are many sources of these 3D fields in tokamaks, intentional and otherwise. The two most significant sources of these 3D fields in DIII-D are shown in figure 3. The first are the ex-vessel correction (C) coils which are used to correct the non-axisymmetric irregularities of the machine's magnetic field, usually due to misaligned or imperfect coils and their bus-work [16]. In addition to the C-coils, DIII-D also has internal (I) coils used to stabilize edge

magnetohydrodynamic instabilities, namely ELMs. ITER will have 3D coils inside the vacuum vessel similar to the DIII-D I-coils, which will produce RMPs [14].

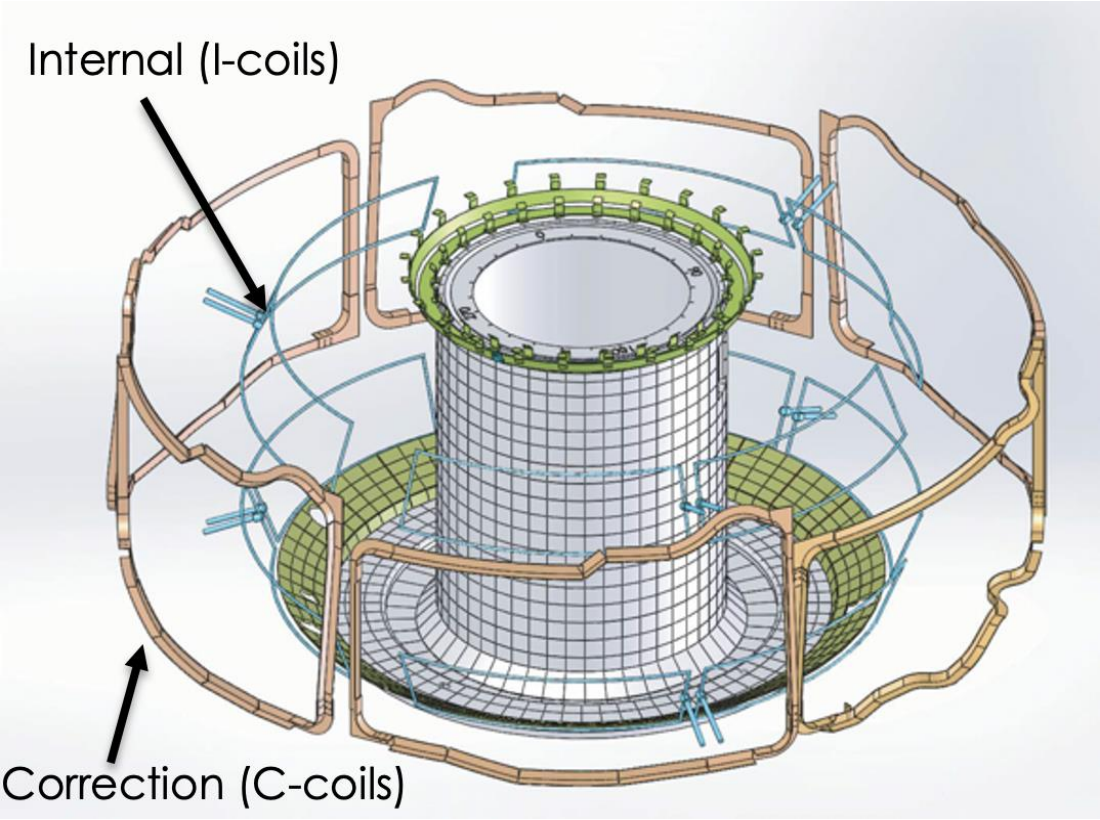

Figure 3: The DIII-D coil assembly with the C-coils used for error field correction and the I-coils used for ELM suppression.

The L-H transition is a complex phenomenon with several key control parameters, some of which are altered by RMP fields. In ITER, RMP fields will be present prior to the transition into H-mode to prevent the first and usually largest ELM. The purpose of this study is to assess the impact of both RMP and non-resonant (NRMP) components on the L-H power threshold over a range of DIII-D plasma conditions, which can eventually be projected to ITER. Because operating in H-mode is essential for ITER to achieve its mission goals of Q=10, ELM control for ITER, and likely future reactor-scale devices will be essential as well.

Previous Work

L-H Transition Theory

The H-mode is defined by a transport barrier near the last closed flux surface (LCFS) that increases confinement of heat and particles by reducing turbulence through shear suppression. One proposed physics-based mechanism is found in [17], and a non-exhaustive review of H-mode studies can be found in [18] and [19]. Connected by the toroidal velocity, poloidal velocity, and the pressure gradient, the radial electric field (E_r) profile induces the formation of this barrier via sheared ExB flows [20]. The radial force balance is shown in eq. 2.

$$E_r = \frac{\nabla P_i}{Z_i n_i} + v_\phi B_\theta - v_\theta B_\phi \quad \text{(eq. 2)}$$

E_r is the radial electric field, P_i is the ion pressure, Z_i is the ion charge, n_i is the ion density, v_ϕ and v_θ are the toroidal and poloidal velocities, and $B_\phi$and B_θ are the toroidal and poloidal components of the magnetic field. Work on ASDEX shows the ion heat flux near the LCFS playing a key role in triggering the L-H transition due to its large part in determining the ∇P_i term of equation 2 [21]. RMPs have been shown to modify the depth of this well and in some cases, even reverse the sign of the E_r field locally [22]. Figure 4 compares the ExB velocities for a variety of RMP magnitudes on DIII-D.

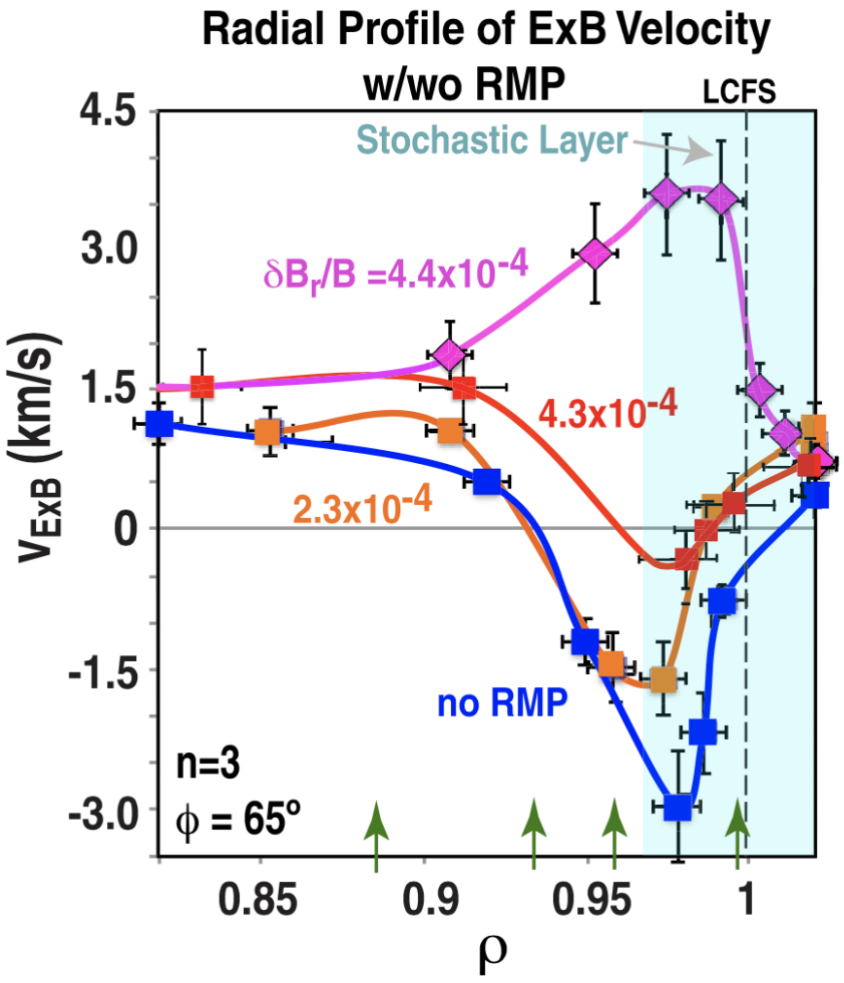

Figure 4: Comparison of ExB velocity profiles under various RMP strengths. It is shown that above some $\frac{\delta B_r}{B}$ value, the local value of E_r reverses for resonant n=3 fields [22]. Here, $\frac{\delta B_r}{B}$ is the value of the applied perturbation evaluated at the normalized radial coordinate ρ = 0.95 and normalized by the toroidal magnetic field on the equilibrium axis.

It is proposed that the increase in the L-H power threshold from RMPs is due to the combined effects of reduced ExB shear (from E_r reversal) and increased stochasticity at the edge causing poloidal/toroidal flow modulation [22]. A common metric to quantify the RMP strength is the relative magnitude, $\frac{\delta B_r}{B}$. δB_r is the magnitude of the applied perturbation evaluated at some radial location and B is the toroidal magnetic field on the equilibrium axis. In DIII-D, the critical

relative RMP strength to affect the power threshold is ~ $3x10^{-3}$, but this value varies slightly between machines [22,23].

Paper Review for Relevant L-H Transition Parameters

Over the last approximately 40 years, several physics and engineering parameters have been found to affect the transition into H-mode. Usually, these trends are studied by comparing pairs of discharges or small sets within an experiment. Some parameters considered for this study, as well as the motivating works, are: main ion species and Z_{eff} [24], q95 [25], injected torque/toroidal rotation [26,27], heating method [21,23], divertor magnetic geometry and plasma shaping (X-point height, strike point location, elongation, triangularity) [23, 28, 29, 30], ion ∇B drift direction [31,32], line-averaged electron density [33, 34, 23] and the resonance, magnitude, and phase of the externally applied perturbation [23,32, 22,35].

An Empirical Scaling for the L-H Power Threshold

Since the H-mode was discovered, there has been a great effort to better understand the physics behind the transition [19, 36, 37], with some simplified physics-based models being produced [17]. Given the stochastic nature of the transition, modeling all of the dynamics to the accuracy needed for prediction is difficult, and while most modern experimental machines have the excess power to overdrive plasmas into H-mode easily, the cost of ITER prohibits this luxury. To address this issue, work has been done to create databases of L-H transitions in an attempt to create a robust empirical scaling. Yves Martin et al. published an empirical scaling law in 2008 using a database of L-H transitions from multiple machines to predict the L-H power threshold [38]. This model was used to cite the heating system requirements for ITER and uses

the international global H-mode database (IGDBTH) created by the International Tokamak Physics Activity (ITPA) organization [39]. At the time of the analysis, the IGDBTH database consisted of 2667 time slices corresponding to L-H transitions across six tokamaks: DIII-D, Alcator C-Mod, ASDEX-U, JET, JFT-2M, and JT-60U. Here, time slices are snapshots of global plasma parameters tied to a specific time in the discharge, usually specified to the millisecond. In the 2008 study, the power at the L-H transition is quantified by the heat flux carried by thermal particles through the LCFS and referred to as the loss power "P_{Loss}", as a reference to the power loss through the boundary (eq. 3).

$$P_{Loss} = P_{Ohm} + P_{Abs} - \frac{dW}{dt} - P_{F,loss} \ [W] \text{ (eq.3)}$$

The ITPA database defines each of these terms: P_{Ohm} is the total ohmic power, P_{Abs} is the absorbed power consisting of the total injected neutral beam power minus shine through, dW/dt is the time rate of change of the total plasma stored energy as determined from MHD equilibrium reconstruction, and $P_{F,loss}$ is the fast ion power lost from the plasma through charge exchange and unconfined orbits. Even though the ITPA defines these terms, it is up to each individual machine on how they gather and report these values. For example, for the data on $P_{F,loss}$ given by DIII-D, these estimates are given by the empirical equation 4, where IP is the plasma current [40]:

$$P_{F,loss} = P_{Abs} * e^{(3.3-IP/10^6)/100} \ [W] \ \text{ (eq.4)}$$

Accompanying each of the time slices are global parameters such as line-averaged electron density, plasma surface area, elongation, etc. These time slices are then filtered to only contain ITER like plasmas using the following selection criteria:

> …single null configurations with ion grad B drift towards the X point, deuterium plasmas, and rejects time slices with too low plasma density (Alcator C-Mod: ne20(unit of $10^{20}m^{-3}$) < 0.8, ASDEX Upgrade: ne20 < 0.2, DIII-D: ne20 < 0.2, JET: ne20 < 0.1, JFT-2M: ne20 < 0.2, JT-60U: ne20 < 0.1), too low safety factor at the 95% flux surface (q95 < 2.5), too close to the beginning of heat pulse, too large counter-NBI fraction (Pctr/PNB > 0.8), too small gaps between plasma surface and wall (d < 5 cm), too high radiation losses (Prad/PL > 0.5). SELEC2007 furthermore rejects transitions obtained in Ohmic conditions since they are not relevant for ITER and also rejects Electron Cyclotron only heated discharges [38]

Applying this criterion leaves 1024 L-H transitions that are then fit to three global parameters that were reported to the database: line-averaged electron density, n_{e20} [10^{20} m^{-3}], toroidal magnetic field, B_T [T], and the plasma surface area, S [m^2]. Fitting a power law of these three variables via a least squares approach results in the Martin Scaling (eq 5).

$$P_{Thresh} = 0.0488e^{\pm 0.057} n_{e20}^{0.717 \pm 0.035} B_T^{0.803 \pm 0.032} S^{0.941 \pm 0.019} \; [MW] \; (eq. 5)$$

The format of figure 5 is used throughout this paper, with P_{Loss} on the y-axis and P_{Thresh} on the x-axis, both in logarithmic scale. Each of these points represents a L-H transition time slice from a machine as indicated by the legend. DIII-D is shown as the orange squares in the range of 1-3 MW of P_{Thresh} with a vertical spread from 1-3 MW of P_L. The black dashed line represents the 1:1 correlation between the actual power at the L-H transition and the Martin scaling's prediction. Any points above this dashed line represent transitions that took more power to enter H-mode, while any points below took less power than the scaling predicts.

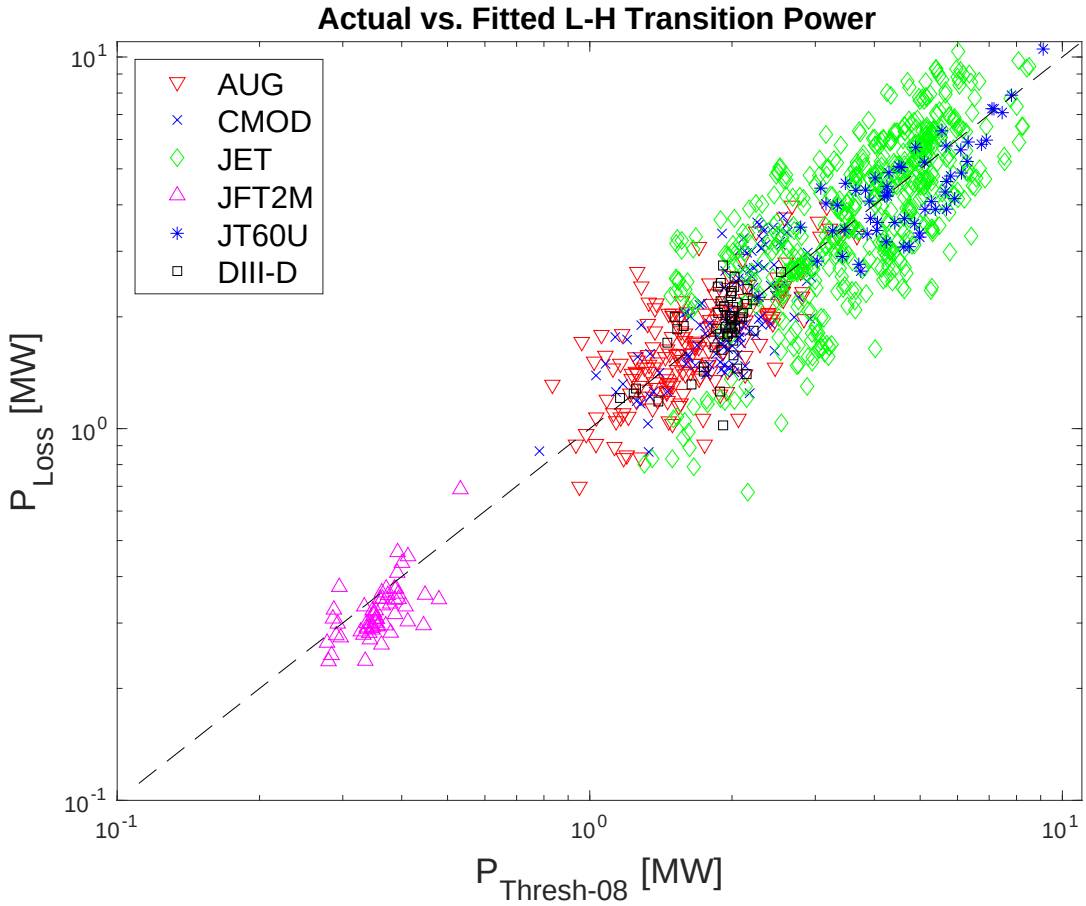

Figure 5: Recreation of the loss power vs. L-H threshold power plot from Martin's 2008 paper, omitting transitions not used in the regression, with an added black dashed line representing the 1:1 correlation between the predicted and measured L-H power threshold [38].

ITPA Database Advantages

Because of the number of machines that gave data, this database spans a wide range of parameter space in the fitted parameters (B_T, n_{e20}, S). This span, and the associated value provided by the ability to extrapolate, would not be possible if the study was restricted to one machine.

ITPA Database Disadvantages

Several sacrifices are made in order to construct such a wide database as seen in the ITPA study. One of the most criticized sacrifices is the exclusion of the power radiated from inside of the plasma from the P_L term. While some machines (AUG, C-Mod, DIII-D, JET, JT-60) were able to report this parameter via bolometry [41], others did not have the capability. Therefore, to retain as much data as possible, this term was not included in the loss power. Another disadvantage of this approach is the significant variability in how each device reports values to the database. For example, $P_{f,loss}$ is reported differently for each device used in this study: DIII-D uses an algebraic equation based on I_P (eq. 4), JET uses a different algebraic equation that is a function of I_P and line-averaged electron density, ASDEX uses fits from the neutral beam FREYA code [42], and JFT2M uses fits from a Monte Carlo simulation. As discussed in later sections (see section C of Results), this term can represent upwards of 30% of the absorbed power in DIII-D. This also occurs with other important values in P_L as well (P_{Ohm} and dW/dt). Finally, there are intrinsic differences between the machines in this database, independent of plasma conditions. Specifically, the variation in PFCs (metal vs. graphite) across devices is known to have a strong effect on the L-H power threshold [33, 43, 44]. This can be seen in figure 6, where every machine except for C-Mod has carbon walls. A small ($\sim B_T^{0.5}$) dependence is seen for C-Mod, while the other, carbon walled machines, show a much stronger B_T dependence ($\sim B_T^2$).

Updates to P_{Loss} and P_{Thresh}

In the 2008 ITPA scaling, the loss power is defined as equation 3. To be explicit, P_{Abs} is defined as $P_{Abs} = P_{NBI} + P_{ICH} + P_{ECH}$ where NBI is the neutral beam heating and ICH/ECH are

the ion/electron cyclotron heating terms. With evidence pointing to the L-H transition heavily involving edge physics, it is often noted that the core radiated power should be subtracted from P_{Loss} to more accurately define the relevant power. This term is left out of the 2008 study because not every machine in the database had the tools to report that value accurately. For this updated study, the power radiated from the core is included in P_{Loss} and is calculated via bolometers on DIII-D [41]. Subtracting the core radiated power "P_{Rad_core}" from P_{Loss} gives the updated definition as:

$$P_{Loss} = P_{Ohm} + P_{Abs} - dW/dt - P_{F,loss} - P_{Rad\_core} \quad [W] \quad (eq. 6)$$

In the 2008 study, DIII-D reports $P_{F,Loss}$ using an empirical algebraic equation that is a function of purely the plasma current I_P and the neutral beam injected power (eq. 4). The validity of this estimation is assessed using the time-dependent transport code TRANSP, as it is generally understood that eq. 4 underestimates these losses [45]. Previous studies have shown that proper calculation of these losses is computationally intensive, even for a single discharge, and so is outside the scope of this work [46, 47]. Simplified neutral beam codes like RABBIT give a reasonable prediction of these losses but only for the instances where there is co-current neutral beam injection [48]. When counter beams are active, these losses can drastically increase to 10-50%, depending on current, and simplified codes like RABBIT are no longer accurate [47]. On top of general underpredictions of these losses, RMPs have been shown to drastically increase neutral beam prompt losses by order of magnitude, and RMP ELM suppressed shots with n = 3 show up to 8.4% of injected power is lost, compared to 2.7% with axisymmetric fields only [47, 49]. These estimates do not include charge exchange losses. Instead of using equation 4, TRANSP results will be compared to eq. 4 to optimize the calculation of these losses for a database scale.

Lastly, an additional term is added to P_{Thresh} that allows for the quantification of the effects of the 3D fields on the L-H power threshold. This term, $(1+ \delta b/B_T * 10^4)$, represents the 3D perturbation evaluated on some magnetic flux surface, δb, normalized by the on axis magnetic field, B_T. Formatting the term in this way provides a comparison across various machines, independent of both the device's geometry and the presence of RMPs. I.e., if a particular discharge has no RMPs, the threshold power will not go to zero. For RMP ELM suppressed discharges, it typically has a minimum value of $\sim 10^{-4}$, with a maximum value on the order of $\sim 10^{-3}$. The multiplying factor of $1x10^4$ is to prevent numerical issues during a non-linear least squares regression.

Data Analysis

Creation of a L-H Transition Database

DIII-D's contribution to the ITPA L-H transition database consists of shots between 1993 and 1994 (shot numbers from 78,151 to 84,042). Since that time, the quality and availability of diagnostics have generally improved. To capitalize on the improvements in technology and understanding of the physics of the L-H transition, a new database consisting of only DIII-D discharges has been created.

Restricting this study to a database of DIII-D L-H transitions has its disadvantages. Contrasted with the 2008 ITPA study, this database can only span the parameter space of DIII-D. This restriction puts limitations on the line-averaged density, toroidal magnetic field, and plasma surface area. In general, DIII-D's plasma surface area varies from ~50-55 m^2, the toroidal magnetic field from 1-2.1T (with a heavy bias towards 1.8-2.1T), and the L-mode line average

density from 0.15 - 0.5x10^{20} m^{-3}. Figure 6 shows the span of B_T accessed for the ITPA study. Comparing that to the original span of the database, this will only access a subset. Because of this, the scaling from this database may need adjustments for use on other machines.

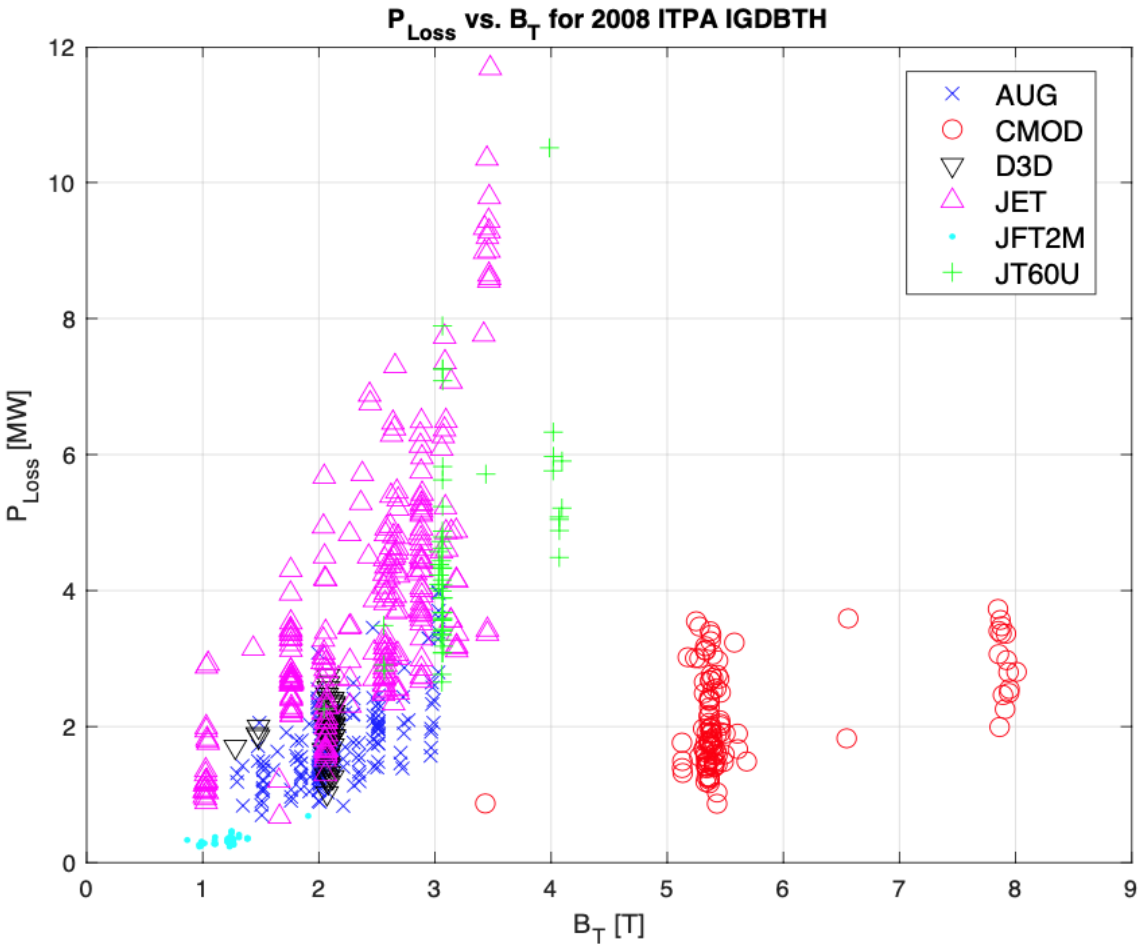

Figure 6: P_{Loss} vs. B_T for the 2008 ITPA L-H scaling law. The range in B_T spans from just under 1T to about 8T, with only C-Mod populating the points above 5T.

While the range in the 0-D parameter space is somewhat limited, a DIII-D specific database has its advantages. This database is well documented which allows for an understanding of the potential limitations and biases associated with the methods. In addition, DIII-D's advanced diagnostics allow for the exploration of important L-H parameters that may not be

available if other machines were included. By focusing on a single machine, the number of "hidden" parameters that change is limited.

Most transitions were added to the database through the workflow that is described in the following section. As an overview, a wide net was cast using TokSearch [50] implemented in OMFIT [51] to return a list of potential database cannidates. A brief introduction on these tools via excerpts from the corresponding papers can be found in the appendix. From this list, L-H transitions are identified by hand, and then discharges are passed through a series of filters designed to target transitions with the highest quality information on P_{Thresh}. Finally, the resulting transitions are assigned a confidence value based on the uncertainty in the loss power term.

Obtaining Potential L-H Transition Database Candidates

A SQL query is the first tool used to filter through DIII-D's approximately 190,000 discharges. This initial filter returns discharges that last longer than 1 second and have a toroidal magnetic field greater than 1T. This essentially only returns discharges where there might have been plasma produced with a transition. This trimmed list is then passed to TokSearch, a tool that can be used to do server-side filtering to process a large amount of DIII-D experimental data efficiently. The filters that are applied in this step primarily search for discharges with potential RMPs by looking at the I- and C- coil currents.

Specifically, derived signals with the format of I(U/L)N(1/2/3)BAMP and CN(1/2/3)BAMP are used for logical filtering. Both signal expressions represent the normal magnetic field component evaluated at the plasma limiter directly in front of the respective coil. E.g., IUN3BAMP gives the n=3 harmonic magnetic field amplitude from the upper I-coils. Determining the level that is considered noise (about 1G) gives a logical expression to look for

discharges with no potential RMPs. For example, if the maximum value of all BAMP signals within the selected time window is less than 1G, there is no applied 3D field and, therefore, no potential RMPs. Deliberate 3D perturbations are found to have an average value of at least 5G, and this gives an expression that can look for the presence of potential RMPs. Using these two cutoff criteria, different toroidal modes, as well as their sources, can be targeted or excluded. This ability allows for the targeting of potential shots that may fill in holes in the database. Because this filter only looks for the presence of 3D fields and not for L-H transitions, this list of shots is passed to the next step in the workflow where L-H transitions are manually identified.

Manually Identifying L-H Transitions

Experimentally, the transition from L- to H-mode can be seen in several diagnostics. First, filterscopes are used to capture visible light from atomic emissions coming from inside of the tokamak [52]. At the edge region, plasma temperature drops, and ions are able to recombine with electrons, resulting in photon emission. These photons have a wavelength that corresponds to the difference between the final and initial energy states of the electron, with the brightest of these being the Balmer-alpha line (D_{alpha}= 656nm). Due to the improved confinement of hydrogen ions in H-mode plasmas, the flux of D-alpha photons is reduced in the divertor region, and there is a drop in neutral particle recycling. Due to this reduction, filterscopes that are looking near the divertor will see a rapid drop in the D_{alpha} emissions at the L-H transition. Several filterscope cords in DIII-D are seen in figure 7.

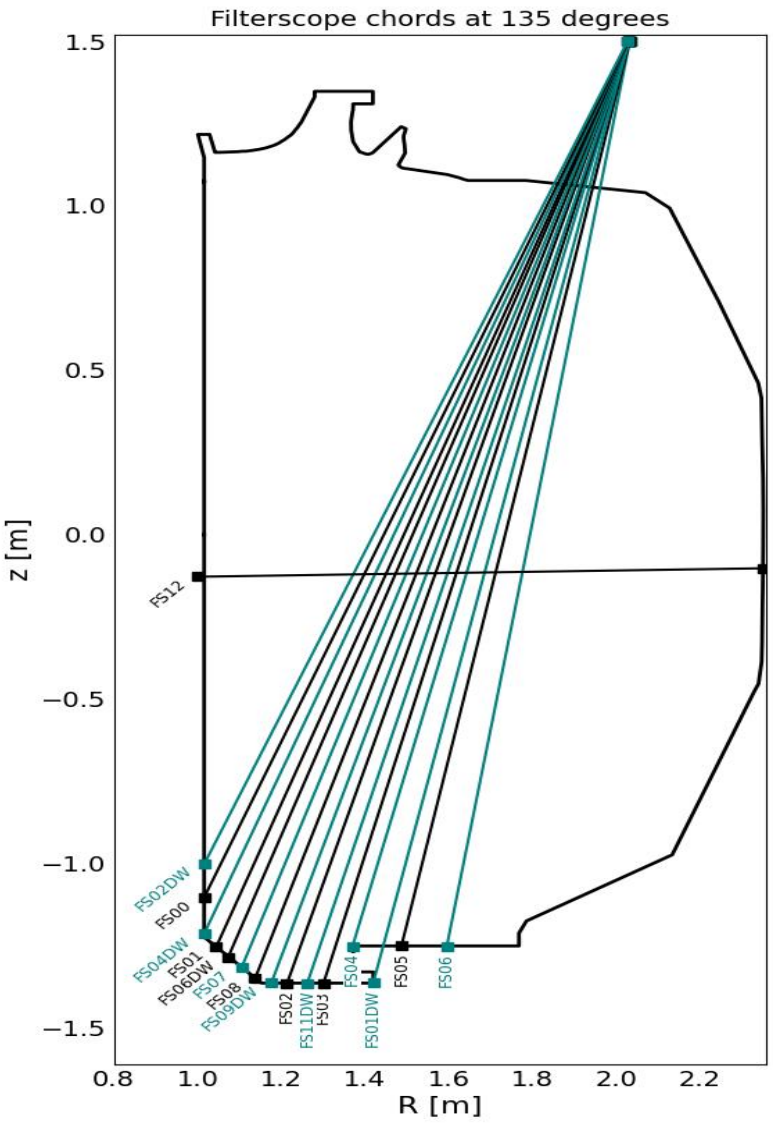

Figure 7: Lower filterscope cords of DIII-D are shown on a poloidal cross-section. These measurements are taken at a toroidal angle of 135 degrees and observe the lower divertor region.

The second signal used is the line averaged electron density, measured with interferometry. In the H-mode, the formation of the edge transport barrier leads to a rapid increase in density. Figure 8 shows time traces of these two signals. If a transition is identified, the time at which it happens is stored as a pair with the shot number.

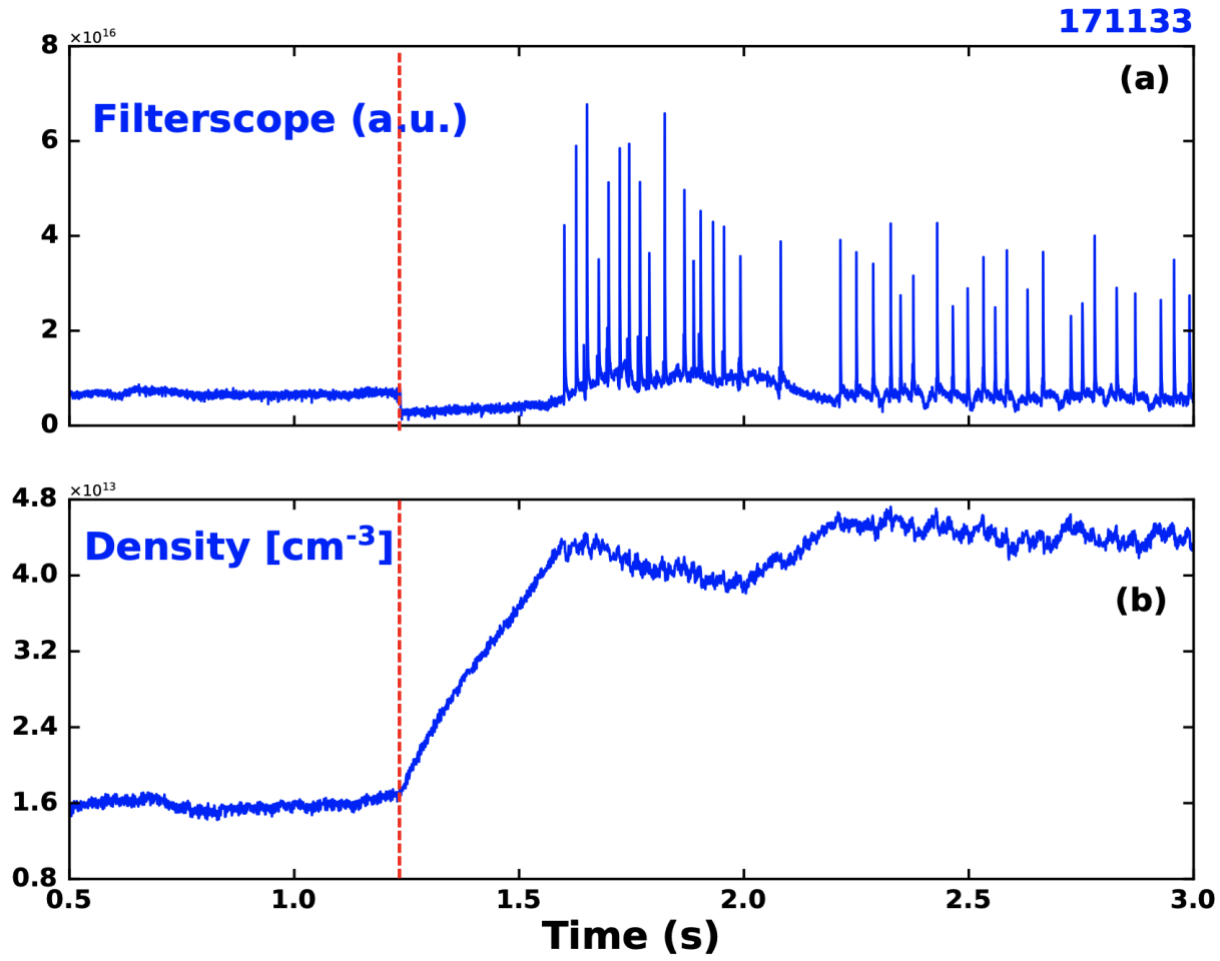

Figure 8: Time series showing the filterscope (a) and density (b) signals used to identify the L-H transition. The time of the transition can be seen around 1.25 seconds, marked with the red dashed line, with the simultaneous drop in the filterscope signal and rapid increase in density.

Filtering Algorithm to Increase Database Confidence

The next step in the workflow is applying filters that serve to reduce uncertainties in the database quantities, namely terms in P_{Loss}.

Removing Overdriven H-modes

For many DIII-D H-mode experiments, the focus is on studying the properties of the H-mode and not ascertaining the exact power threshold. Because of this, H-mode plasmas are

usually formed by supplying power well above that required to transition. Examples of overdriven H-modes are shown in figure 9. In both cases, the red vertical line marks the L-H transition. The plot on the left shows a large step in Electron Cyclotron Heating (ECH) just before the transition, and the right plot shows a similar case with NBI. Because injected power is not absorbed instantaneously by the plasma and depends on the fast ion slowing-down times (10-100ms), instances like this leave the power threshold ambiguous and bracketed by the pre- and post-ramp powers. For the NBI example in figure 9, the power at which the transition happened could be anywhere between 0-6 MW. Generally, the longer after the power ramp that the transition occurs, the closer to the threshold the post-step power is. For this reason, transitions with power ramps exceeding 1MW less than 200ms before the transition are excluded from this database to decrease the uncertainty in P_{Abs}. This filter removes ~50% of the potential candidate shots.

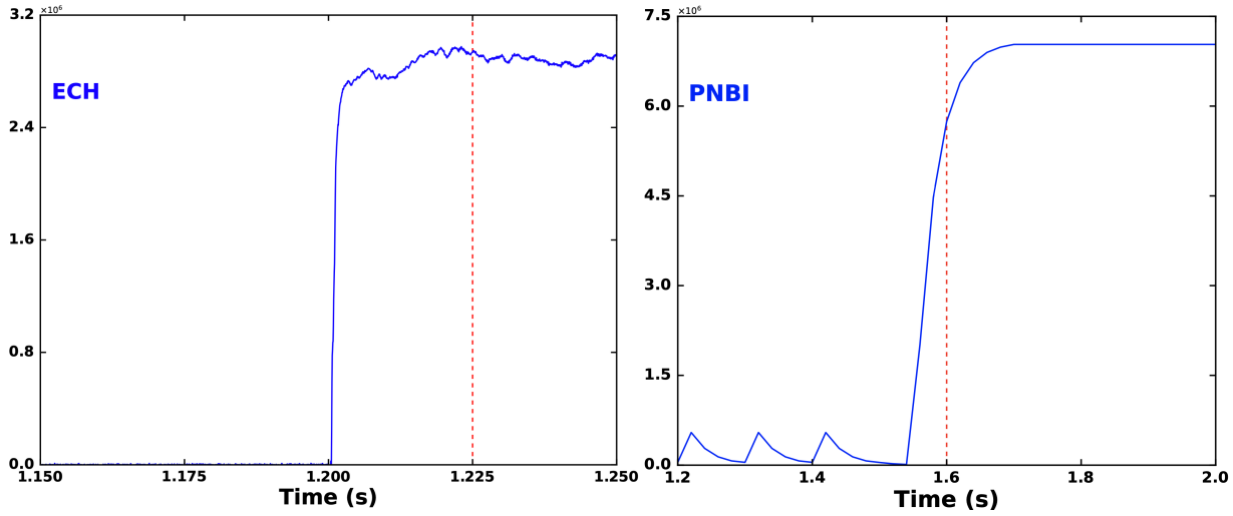

Figure 9: Signals showing a 3 MW step in ECH that triggers a L-H transition marked by the red vertical line (left). A 7MW NBI ramp that triggers an L-H transition, also marked with a red vertical line (right).

Flagging Shots with Counter-Current Neutral Beam Injection

The next filter places a tag on any shots where there was counter-current neutral beam injection during the transition. This filter increases our confidence on the $P_{F,loss}$ term that accounts for fast ion and shine through loss. Codes like RABBIT and TRANSP give a reasonable prediction of these losses but only for the instances where there is co-current injection. When counter beams are active, these losses can drastically increase, and these codes are no longer accurate. Careful calculation of these losses is computationally intensive, even for a single discharge [46, 47].

Removing Shots with Large Neutral Beam Modulation

The final filter excludes transitions that occurred during drastic neutral beam modulation. Neutral beam modulation is typically done to increase the quality of data from spectroscopic diagnostics or for feedback control on plasma parameters [53]. Similarly to the first filter, the power injected during the transition may not be the power that triggered the transition. A case with substantial modulation is shown in figure 10, where the beams are pulsed to 4 MW and then rapidly stepped down to 0 MW. In this example, the transparent trace is the instantaneous injected power, and the opaque trace is that signal with a 100ms causal smoothing to approximate the slowing-down time. Like the cases with large power ramps, the transition power is bracketed by the trough and peak of the power pulse. This modulation has a large impact on both the P_{NBI} and dW/dt terms of P_{Loss}, so shots with modulation amplitudes >1MW are excluded from the database. This filter removes ~25% of potential candidates.

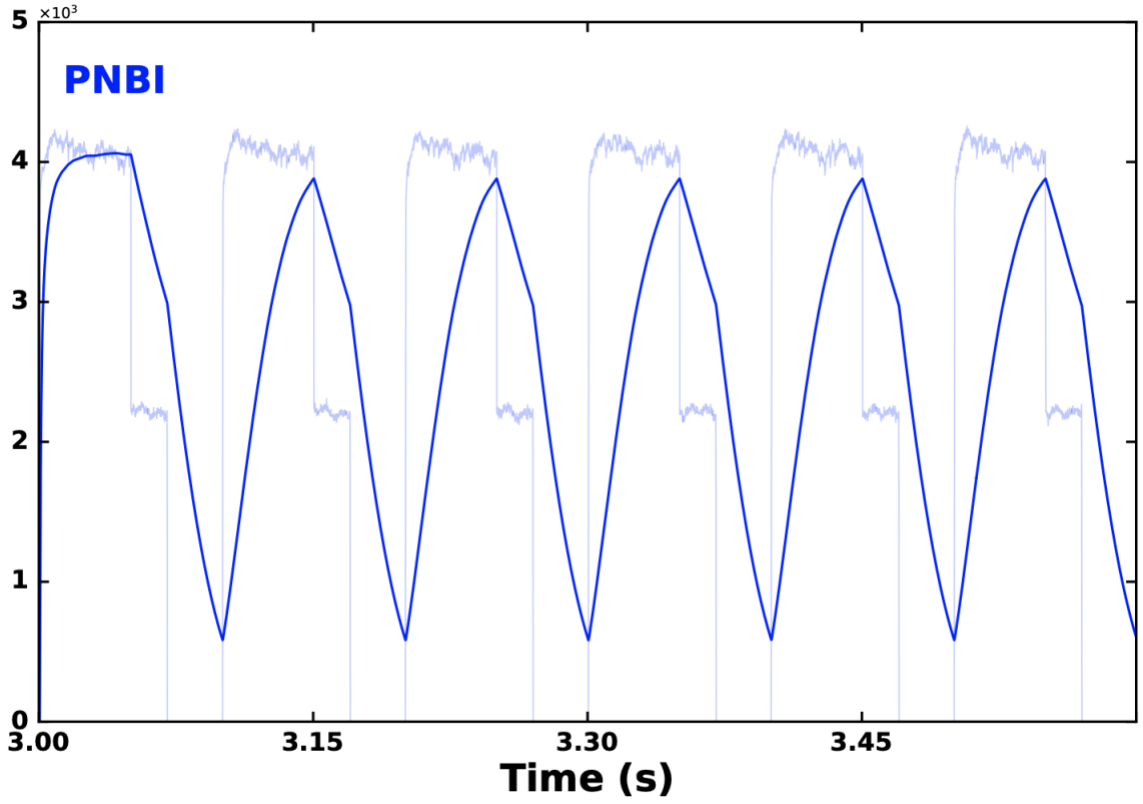

Figure 10: Time trace showing the power injected by neutral beams being modulated. The transparent trace is the raw signal, while the opaque is a result of a 100ms casual smoothing.

Assigning Confidence Values to L-H transitions

L-H transitions that make it through the above filters are assigned a value to note the uncertainty associated with P_{Loss}. The possible values range from 1 to 4, with 1 being the most confident and 4 being excluded from the database. A detailed description of each value is given in table 1. Defining the confidence value allows for a clear description of the database contents and quality. An example of a transition that would be assigned a confidence value of 1 is shown in figure 11.

Table 1: Descriptions of confidence values for L-H transitions in this database.

Confidence value	Description of L-H transition	Associated Uncertainty on P_{Abs}
1	Most confident: < 0.3MW of variance (Peak to trough) in the instantaneous injected power (non-varying w/100ms smoothing window) and no power steps < 200ms before transition.	< +/- 0.1 MW
2	Confident: < 0.5 MW of variance (Peak to trough) in the PNBI signal and no power steps < 200ms before transition.	+/- 0.25 MW
3	OK confidence: <1MW of variance in the PNBI signal but can include <1MW power steps < 200ms before transition.	+/- 0.5 MW
4	Poor confidence: >1MW of variance/large power ramps. Excluded from the database.	N/A

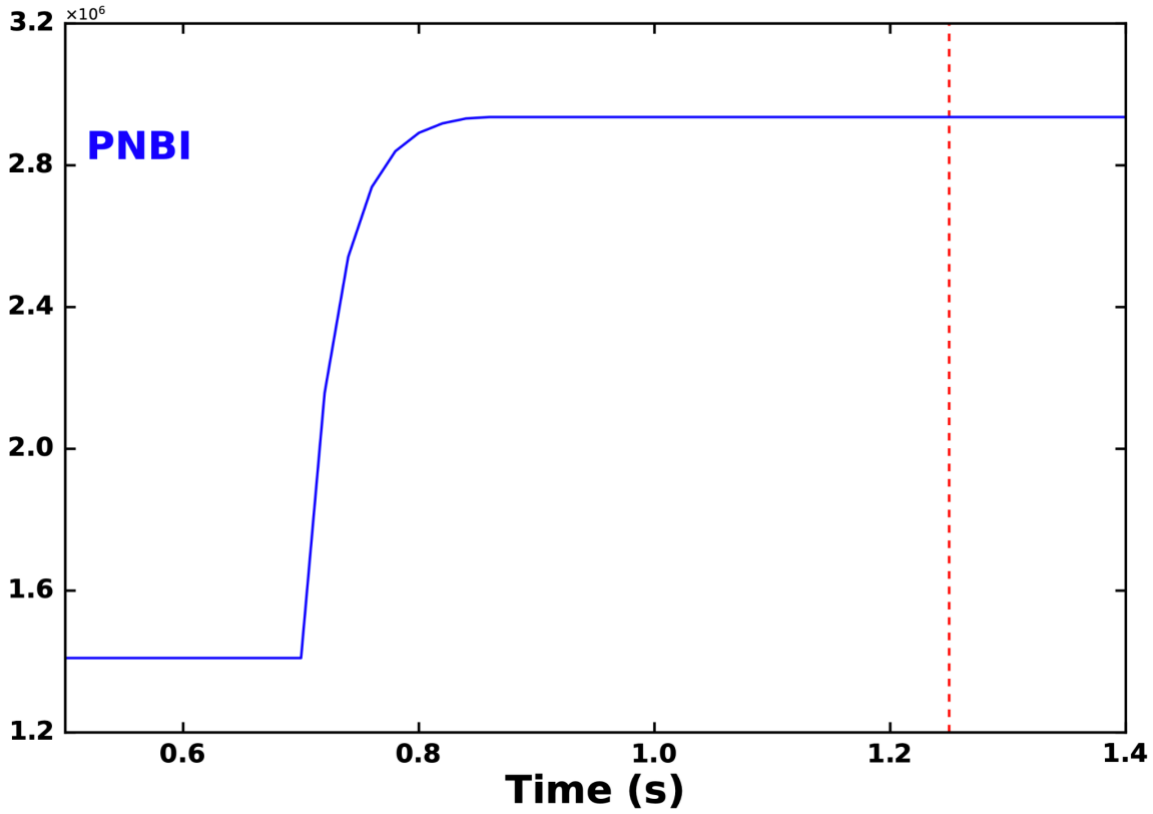

Figure 11: Example of an L-H transition (noted by the red vertical line) that would be marked with 1. There is no modulation of the neutral beams but a 3MW NBI ramp ~500ms before the L-H transition.

Database Analysis Methods

EFIT

EFIT is a code used to generate 2D (axisymmetric) plasma equilibria from the Grad-Shafranov equilibrium equation [54]. This tool uses experimental measurements from magnetic field probes and external poloidal flux loops to constrain the solution of the equilibrium equation. Equilibria are constructed for each shot with varying spatial and temporal resolutions, but the standard case is run on a 20ms time base and on a spatial grid of 65x65. For this study, a more highly resolved equilibrium is needed in both space and time. Custom EFITs were made that are tailored to L-modes (i.e. no pedestal) and run on a 1ms time base with a 129x129 spatial

grid. It has been shown that a spatial grid finer than this does not result in significantly lower errors [56]. Checks are performed to make sure that the equilibria make physical sense and include ensuring that the flux surfaces are concentric, that the LCFS has 90-degree intersections at the x-point, and that there are no non-physical profiles in temperature or density (pedestals, upward turn at the edge, etc.). Figure 12 shows a 2D L-mode equilibrium, along with the pressure and safety factor profiles, produced just before the L-H transition for a shot in this database. These files are then fed to the next code to evaluate the resonance and strength of the 3D fields on a range of flux surfaces at the moment just before the transition.

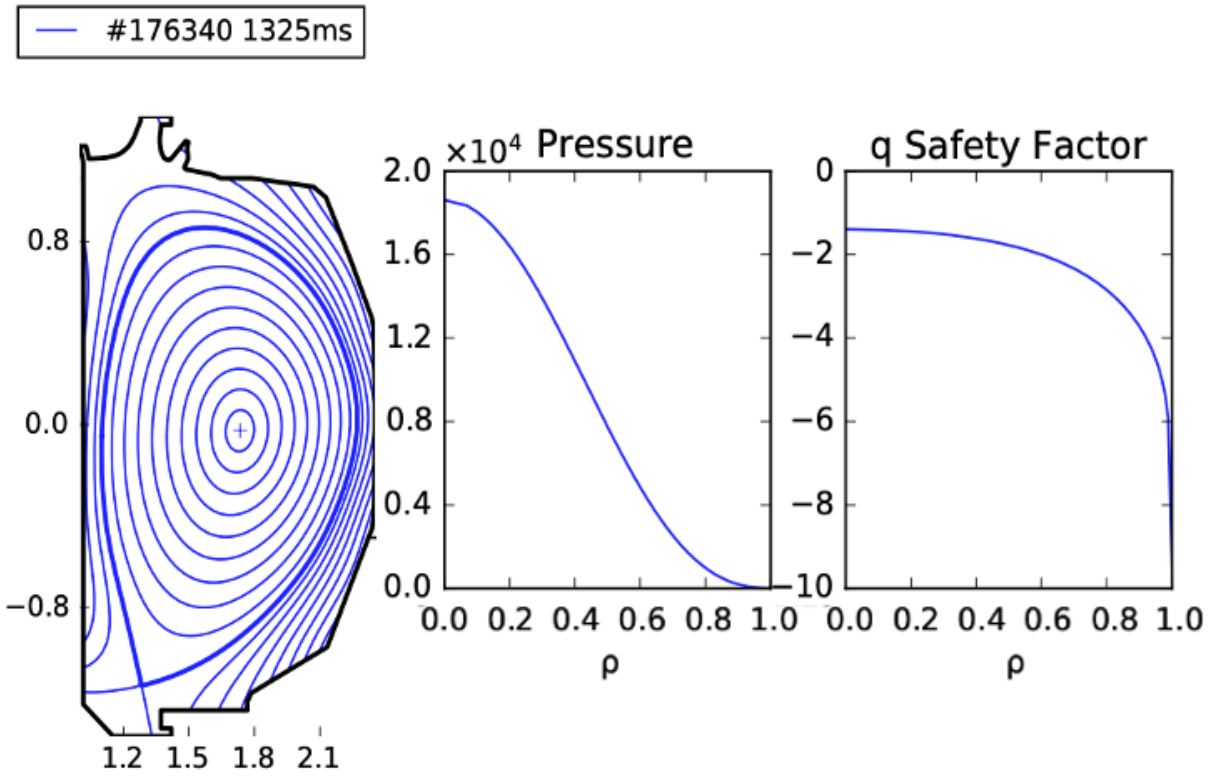

Figure 12: Outputs of EFIT showing a poloidal cross-section of DIII-D and the 2D plasma equilibrium (left) in a conventional lower-null configuration. Plots on the right show pressure and safety factor profiles on a normalized radial axis.

SURFMN

The SURFMN code is used to do a Fourier analysis of the non-axisymmetric magnetic fields as well as perform magnetic island calculations. SURFMN is a vacuum code and does not calculate the self-consistent plasma response that would maintain pressure balance. Written in FORTRAN, it takes 2D (axisymmetric) plasma equilibria from EFIT and imposes the 3D fields from the various sources in DIII-D [55]. A product of this work has been the implementation of SURFMN in OMFIT as its own module, including a GUI, for others to use. As a part of this thesis, updates to the workflow now allow large databases of shots/times to be computed efficiently, usually taking less than 20s for a shot-time pair analysis. This is useful for both database analyses like this one and parameter scans that determine optimal 3D field coil configurations.

Two plotting routines, historically written in IDL, were transcribed to python as part of this work to plot the output files of SURFMN. The first, shown in figure 13, is a spectrogram representing the Fourier analysis. On the x-axis is the poloidal mode number 'm', and on the y-axis is the normalized poloidal flux coordinate Ψ_N. The points are colored by the magnitude of the radial magnetic field component (B_r) in Gauss. The white dashed line veering to the left of the plot is the locus of pitch resonance, q = mn, with the q profile being determined by EFIT. This case shows a strong n = 3 resonant component, as indicated by the large B_r field along the pitch resonance curve. In contrast, figure 14 shows the spectrogram for the largely non-resonant n = 2 component where the B_r magnitude along q is ~10 times less than the resonant n = 3 portion. There is no set definition for how far a magnetic field component must be from the resonance curve to no longer be considered resonant. Therefore for this study, the resonant

component is only considered to be the value directly on the resonance curve. As seen in figure 13, the magnitude of the field does not vary significantly +/- 2 poloidal modes from the pitch resonance line.

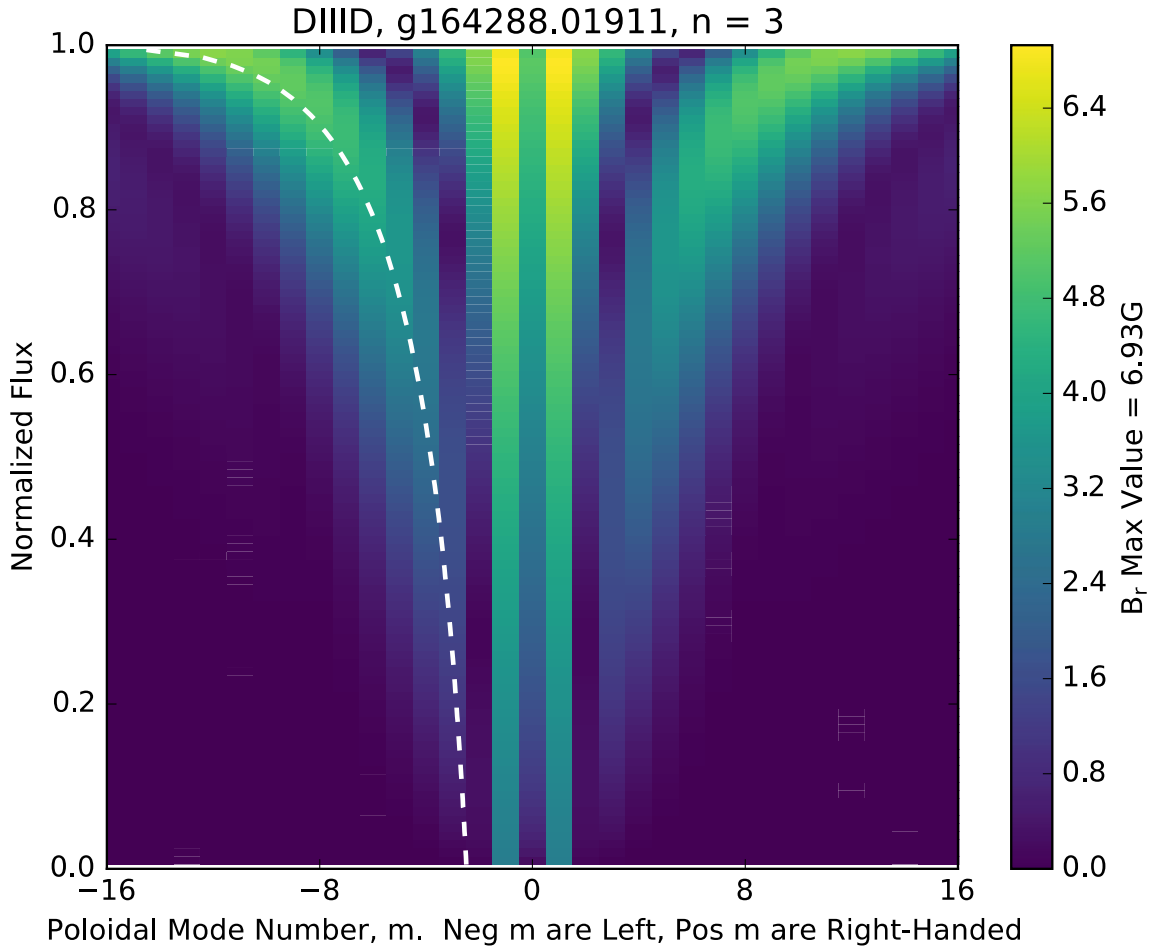

Figure 13: Spectrogram of the radial magnetic field strength at various poloidal modes and normalized poloidal fluxes for a fixed toroidal mode of n = 3. The white dashed line is the pitch resonance line for this particular discharge, which displays a strong resonant component for this toroidal mode.

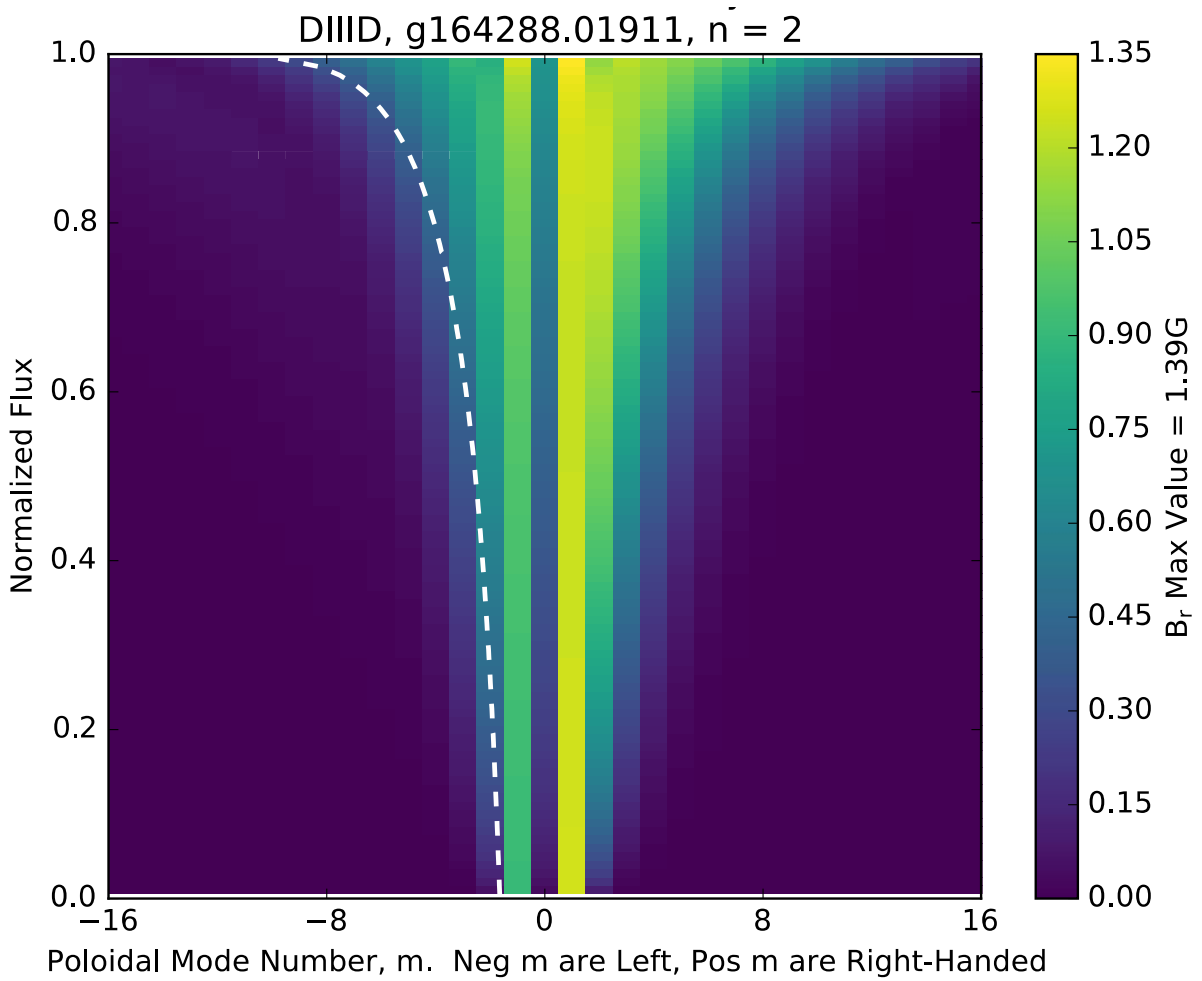

Figure 14: Spectrogram of the radial magnetic field strength at various poloidal modes and normalized poloidal fluxes for a fixed toroidal mode of n = 2. This perturbation represents a non-resonant interaction where the B_r magnitude along q is ~10 times less than the n=3 component at the same Ψ_N.

In addition to the spectrogram, a routine to display vacuum field magnetic island widths vs. a radial coordinate was implemented to show the radial extent of the islands and their overlap, if present. In two dimensions, magnetic islands are closed magnetic flux surfaces and when they overlap, it is thought that a stochastic magnetic field ensues that result in enhanced diffusion of particles radially. Figure 15 shows island width calculations for a particular shot in the database. The black trace is the q profile and the horizontal bars are the island width in Ψ_N.

In this figure, only the n = 1 islands are labeled corresponding to the rational surface (m/n = 4/1, 5/1, etc…) where they exist.

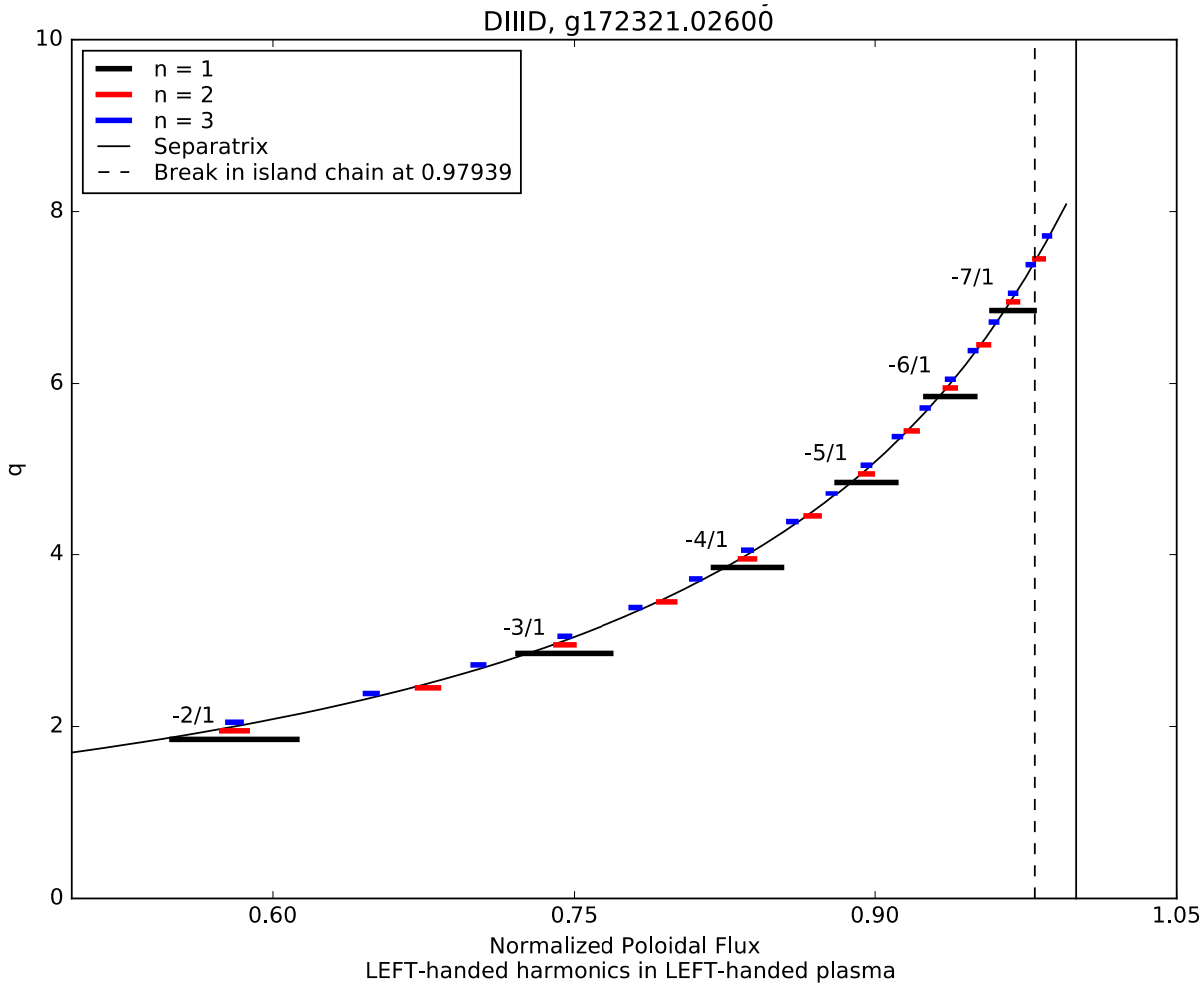

Figure 15: Safety factor 'q' vs. normalized poloidal flux Ψ_N. Island widths are overplotted and colored based on the toroidal mode.

Resonant Perturbation Quantification

Ideally, the E_r profile would be calculated for each transition using charge-exchange recombination (CER) measurements similar to [22]. Next, the closest resonant surface to a chosen point in the E_r profile (potentially the bottom of the well) would be evaluated using a code like M3D-C1 that includes the plasma response to the magnetic perturbations [57].

Unfortunately, the CER analysis to determine the E_r profile in L-mode is not very accurate and has large uncertainties [30]. This means that each discharge would have to be analyzed manually, potentially taking hours to complete a single profile. The next best approach would be to estimate the location of the E_r well using eq. 2 and estimates of the ion pressure profile. It is reasonable to approximate the bottom of the well as near the maximum of the derivative of the ion pressure profile, which corresponds to the first term in eq. 2. For this approach, kinetic equilibria are required to accurately construct the profiles, which, again, are labor intensive. In addition to accurate equilibria, measurement of the inject and intrinsic torque is needed, as it can offset the location of this well due to the $v_\phi B_\theta$ term. The $v_\theta B_\phi$ term of eq. 2 is usually neglected as poloidal velocities are usually an order of magnitude smaller than the toroidal flows, excluding low rotation cases where all three terms can be comparable in magnitude.

Given that there is no consensus on where the RMPs must resonate in the E_r well to affect the power threshold, the fields are evaluated at various radial coordinates instead. In reality, the important radii in this analysis would likely depend on island overlap and the extent of the stochastic region near the scrape-off layer (SOL), which should be calculated with a code that includes plasma response. Furthermore, the effect of 3D fields on the E_r profile is not toroidally or poloidally symmetric, so a measurement restricted to one toroidal angle (like CER) will not capture this [30]. A DIII-D study on the parametric dependence of the edge E_r profile shows the width of the profile to be largely insensitive to a wide range of plasma parameters, with the bottom of the well close to the LCFS [58]. Due to these difficulties, a proxy for evaluating the RMPs in the well is used.

For each discharge, the resonant fields are calculated and recorded at three edge radial coordinates: Ψ_N = 0.95, 0.97, and 0.99. These values are not discrete and are ranges that span ±

0.01 of the described Ψ_N. If there is more than one resonant surface within this range for a particular toroidal mode, the values are averaged and treated as one. The differences between two resonant values in a single range are small, as shown in figure 13. For this study, the range of toroidal modes analyzed is restricted to the n = 1, 2, and 3 modes. This is justified by the coil configuration of DIII-D, where the 6 I-coils are capable of producing the primary modes listed above, with all higher n modes being secondary and of a significantly decreased magnitude. For example, calculating the next 3 higher modes (n = 4, 5, 6) for the same discharge in figure 13 results in a maximum B_r of 0.8G, 1.2G, and 0.8G, respectively. These maximum values are ~10-15% of the n = 3 mode maximum, and the resonant values are an even smaller fraction, as shown in figure 16.

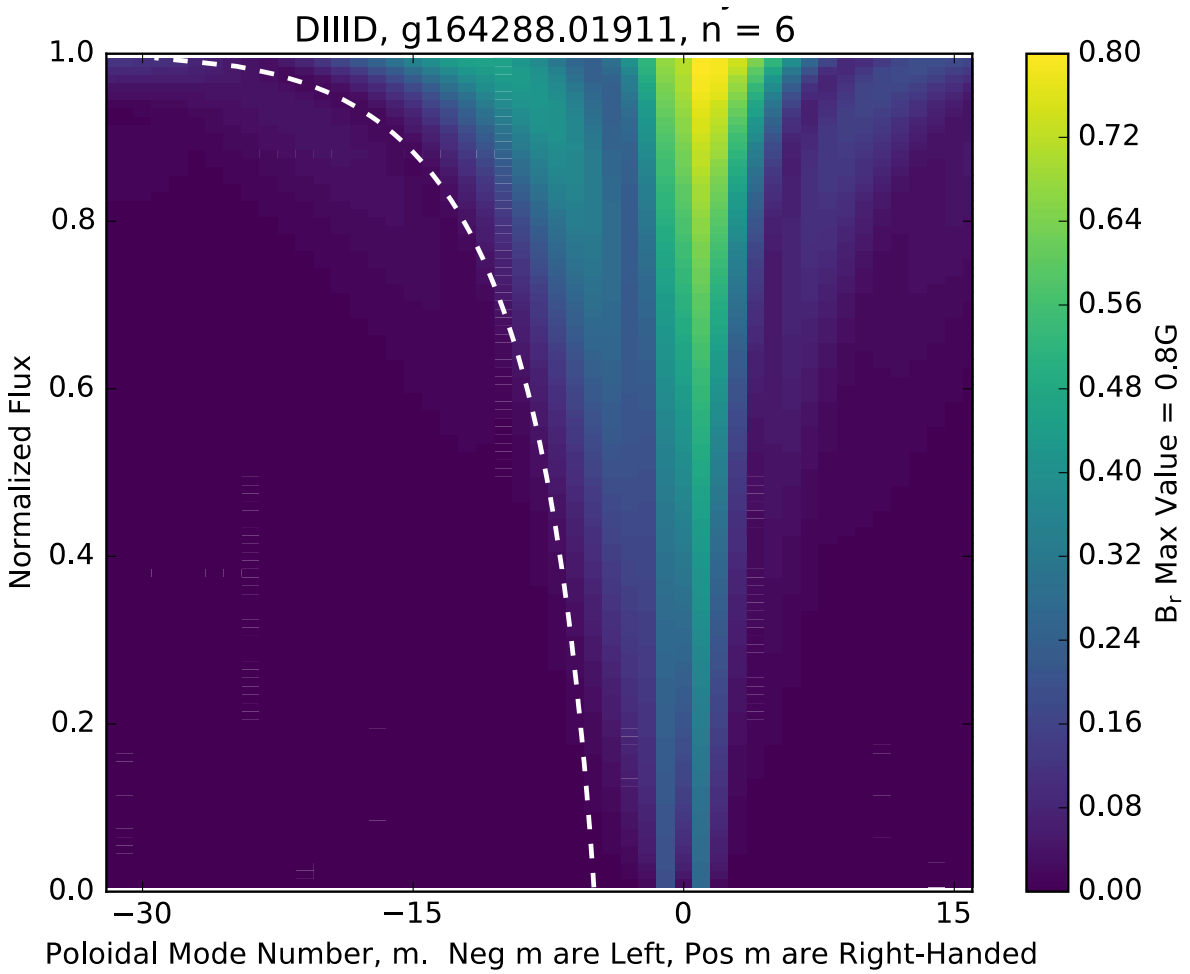

Figure 16: Spectrogram of the n=6 toroidal mode. The white dashed line is the locus of pitch resonance, and the resonant value towards the edge is near zero. For higher n, the edge resonant value is found at larger 'm', in this case, around 30.

Non-Resonant Perturbation Quantification

For each radial coordinate, the non-resonant field is quantified in two ways. The first captures the maximum non-resonant value across all m for the specified Ψ_N. Looking at any of the spectrogram plots, this means finding the y-axis location corresponding to the correct Ψ_N, then going horizontally along the x-axis and recording the largest B_r value, excluding the resonant portion. The second method used records the sum of the non-resonant values at the Ψ_N. Again, the correct Ψ_N is found on the y-axis, and every B_r magnitude in the row (excluding the

resonant value) is summed. This is useful to look at the ratio of resonant to non-resonant fields for a particular perturbation.

Results

Database Demographics

The final DIII-D L-H transition database consists of ~190 transitions, 99 of which have a rating of '1', 32 have a rating of '2', and 61 have a rating of '3'. Table 2 gives more information on the database, including shaping, main ion species, and parameter space accessed. Some definitions are given: drSep is the outboard radial distance to the external second separatrix for single null configurations (positive for upper null and negative for lower null), q95 is the value of the safety factor at Ψ_N = 0.95, kappa is the plasma elongation (defined as $\kappa = (z_{max} - z_{min})/a$, where a is the plasma minor radius and $z_{max,min}$ is the topmost and bottommost z coordinate), and gap (inner/outer) is the gap between the LCFS and the limiting inner or outer machine surface at the magnetic axis.

Table 2: Details of the DIII-D L-H transition database with 192 discharges.

Metric	**Value**
Shots fitting 2008 criteria	60
Upper Single Null	12
Lower Single Null	171

Table 2 continued

Double Null	9
Favorable ion ∇B drift	172
Deuterium plasmas	181
Hydrogen plasmas	6
Helium plasmas	5
Neutral beam power	0 - 6 MW
Electron cyclotron heating power	0 - 3 MW
Plasma current	0.5 - 1.6 MA
Toroidal magnetic field	1 - 2.1 T
drSep	-0.4 - 0.06 m
Plasma surface area	49 - 55 m^2
L-mode line-averaged electron density	1.2 - 5.1x10^{19} m^{-3}
q95	3 - 9
kappa	1.67 - 1.93
gap (inner)	0.02 - 0.18 m
gap (outer)	0.05 - 0.14 m

A conditioned database is formed by using the same selection criteria as the 2008 study and results in 60 transitions; a third have no RMPs, a third has n = 1, 2 RMPs from EFC, and the last third has n = 3 RMP ELM suppression fields. The selection criteria, along with the number of shots removed by the criteria, is listed: single null only – removes 9, favorable ion ∇B drifts – removes 15, $n_{e20} > 0.2$ – removes 75, no purely ohmic transitions– removes 1, gapin/gapout > 0.05m – removes 17, no ECH only – removes 19. The q95, counter-current injection, radiation loss, and kappa constraints remove no discharges. In comparison, the 0-D parameter space spanned by the 2008 study is as follows: BT: 1.3-2.1T, ne20: 0.21-0.57 $x10^{20}$ m^{-3}, S: 60-67 m^2. Transitions from the original database potentially consist of discharges with either no RMPs, or those only from EFC, as RMP ELM suppression was discovered in 2008, and these discharges are from several years prior.

Magnetic Perturbation Database Demographics

Resonant Perturbations

The resonance of magnetic perturbations from I- and C-coils have been evaluated with SURFMN for the entire database. Resonant components are evaluated at Ψ_N = 0.94-0.96, 0.96-0.98, and 0.98-1, with each range not inclusive of the endpoint. Table 3 shows the spread of resonant surfaces for the database with relative magnitudes greater than $1x10^{-8}$.

Table 3: Count of resonant surfaces across three Ψ_N ranges for the database.

Ψ_N	Number of Resonant Surfaces in Database
0.94-0.9599	455
0.96-0.9799	803
0.98-0.999	1339

RMPs with relative magnitudes less than $1x10^{-4}$ (~ELM suppression levels) are omitted given that previous studies show a critical magnitude for effecting the L-H power threshold to be on the order of $3x10^{-4}$ in DIII-D. After this reduction, the number of resonant surfaces totals approximately 400, with most of these being from Ψ_N=0.98 and outwards. The most common toroidal mode in the database is the n = 1 mode likely due to EFC, which occurs on almost every DIII-D discharge. The next most common are the n = 3 RMP ELM suppression fields, followed by the n = 2 modes. Although there are some deliberate n = 2 fields, usually they are a secondary effect of some other applied 3D field, hence the lower relative magnitudes. Figure 17 shows this spread in more detail.

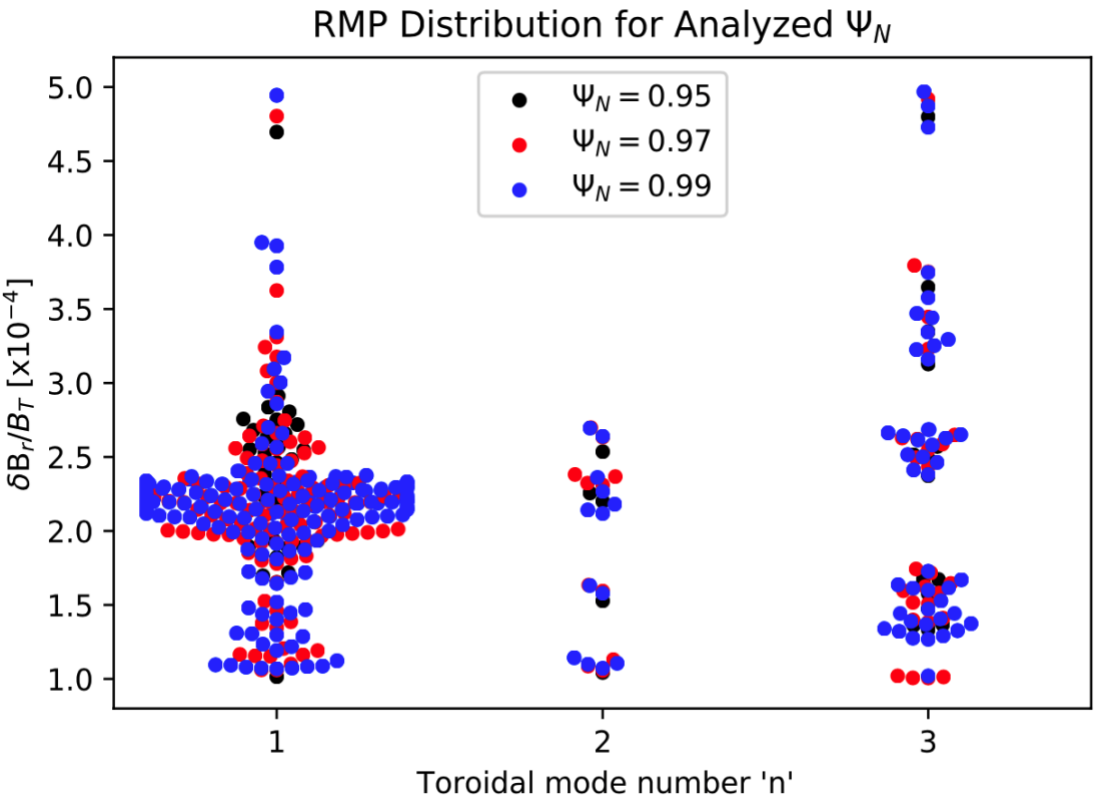

Figure 17: RMP magnitude spread for the three toroidal modes analyzed across Ψ_N. Each circle represents a resonant surface present during a L-H transition. Blue points are surfaces between 0.98-0.99, red are between 0.96-0.98, and black are 0.94-0.96. The horizontal spread of the data is to show the number of surfaces, and in reality, the toroidal mode is only integer-valued.

Looking at each toroidal mode's relative magnitude as a function of Ψ_N further justifies the choice to evaluate the RMP effects on the power threshold at only one Ψ_N, namely 0.99. Figure 18 shows the average relative magnitude of each of the toroidal modes across the analyzed ranges of normalized poloidal flux. A look at any of the toroidal modes shows a near-constant magnitude of the resonant component of the field across the Ψ_N range. This is convenient for this analysis because if an applied field has a resonant component at $\Psi_N = 0.99$, the resonant component further inward has nearly the same magnitude, so 0.99 can be taken as a proxy for the other two ranges. It should be noted that the n = 3 component tends to be slightly

stronger towards the edge, while the n=1 component will be slightly reduced when compared to the inwards components.

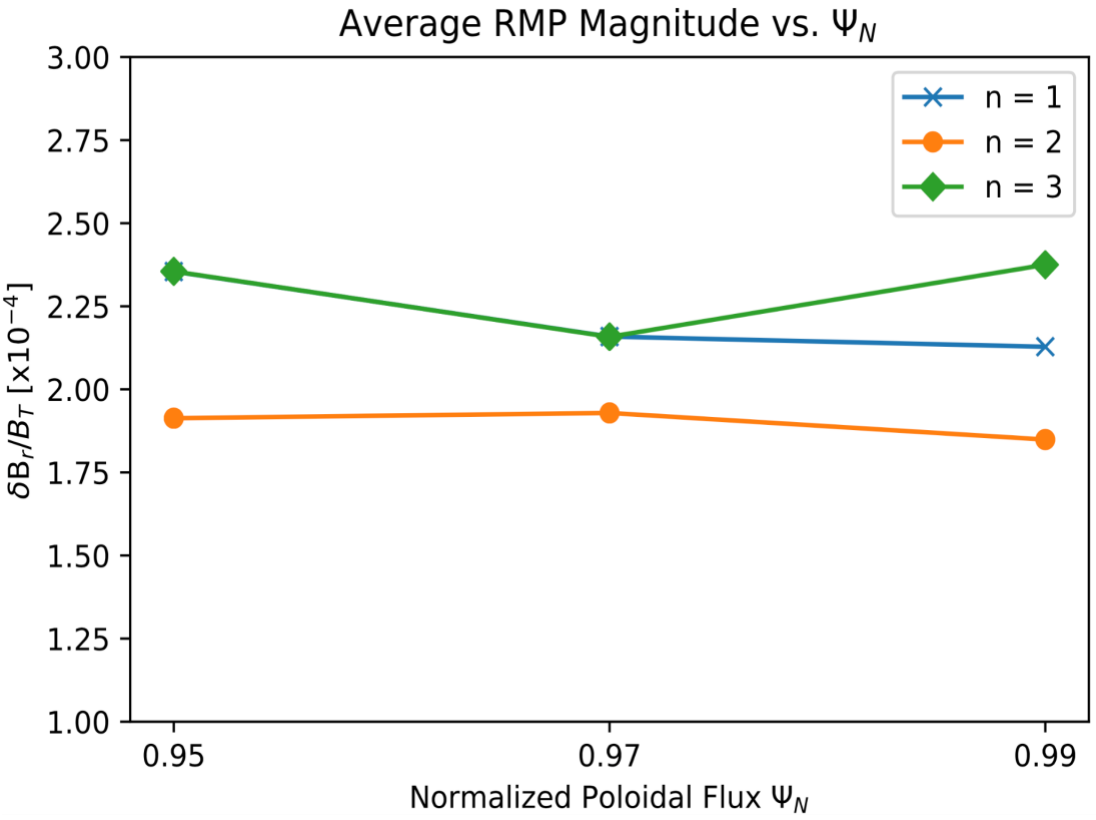

Figure 18: Average RMP magnitude vs. Ψ_N for this database. The n = 1, 2 surfaces slightly decrease in magnitude as they're evaluated at more outward positions. The n = 3 surface shows a slight increase in magnitude near the edge, likely due to deliberate RMP ELM suppression goals.

Non-Resonant Perturbations

The non-resonant fields in this database are similarly documented, and the spread is shown in figure 19. The n = 2, 3 non-resonant components are mostly small, with the majority of the population being around 7.5×10^{-5}, about five times less than the magnitude of n=3 NRMPs found to affect the power threshold. The n = 1 non-resonant components have a wider spread of magnitudes with an average relative magnitude of 3×10^{-4}, which is approximately the strength

found to affect the power threshold for the n = 3 NRMPs. For Ψ_N = 0.95 and 0.97, this distribution of magnitudes is preserved.

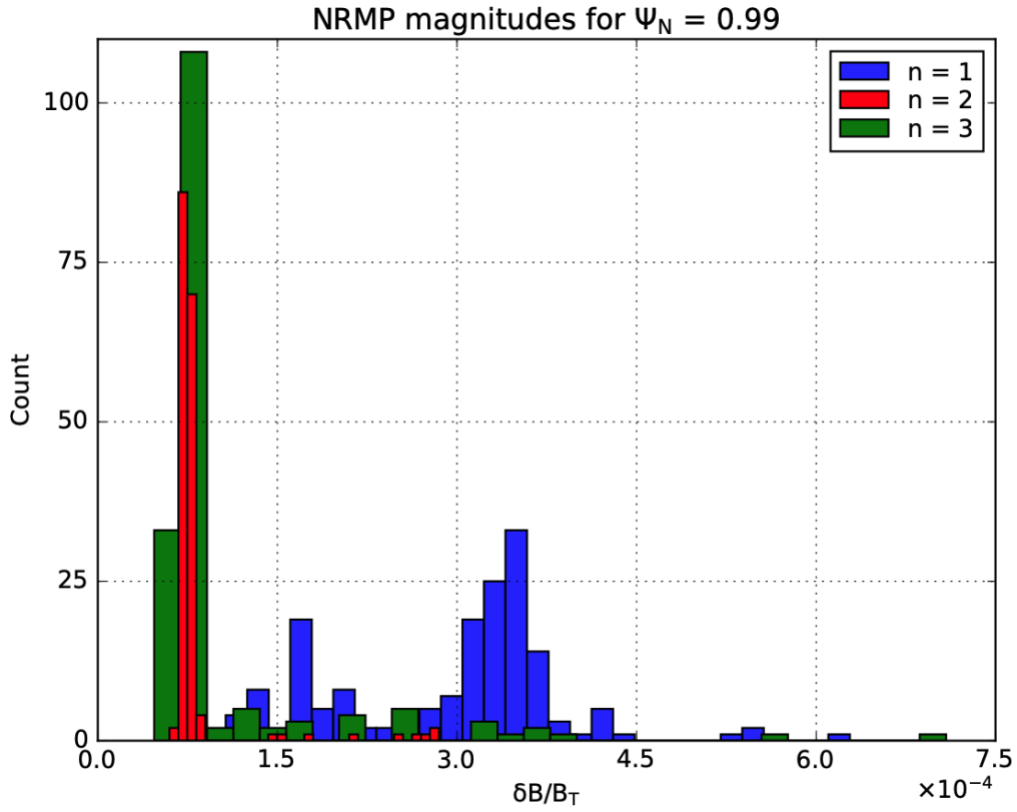

Figure 19: Histogram of relative magnitudes for the non-resonant components of the 3D fields in this database.

The "magnetic perturbation efficiency" is calculated to describe the ratio of resonant to non-resonant fields for each radial location analyzed. Here, this efficiency is described as the ratio of the resonant radial component of the 3D field to the integral of the non-resonant portion across that same Ψ_N. This metric may be useful due to the different effects that resonant and non-resonant fields have on the power threshold. Figure 20 shows this metric for Ψ_N = 0.99. The n =1 mode shows a strong peak of around 5%, which means that for this radial location, only 5% of the applied field is resonant, while 95% is non-resonant. For the n=3 component, the average

efficiency is found to be even lower, around 3%. The distribution of efficiencies changes with Ψ_N as well, tending towards even lower values with decreasing Ψ_N, although the reader should be reminded that these are vacuum approximations.

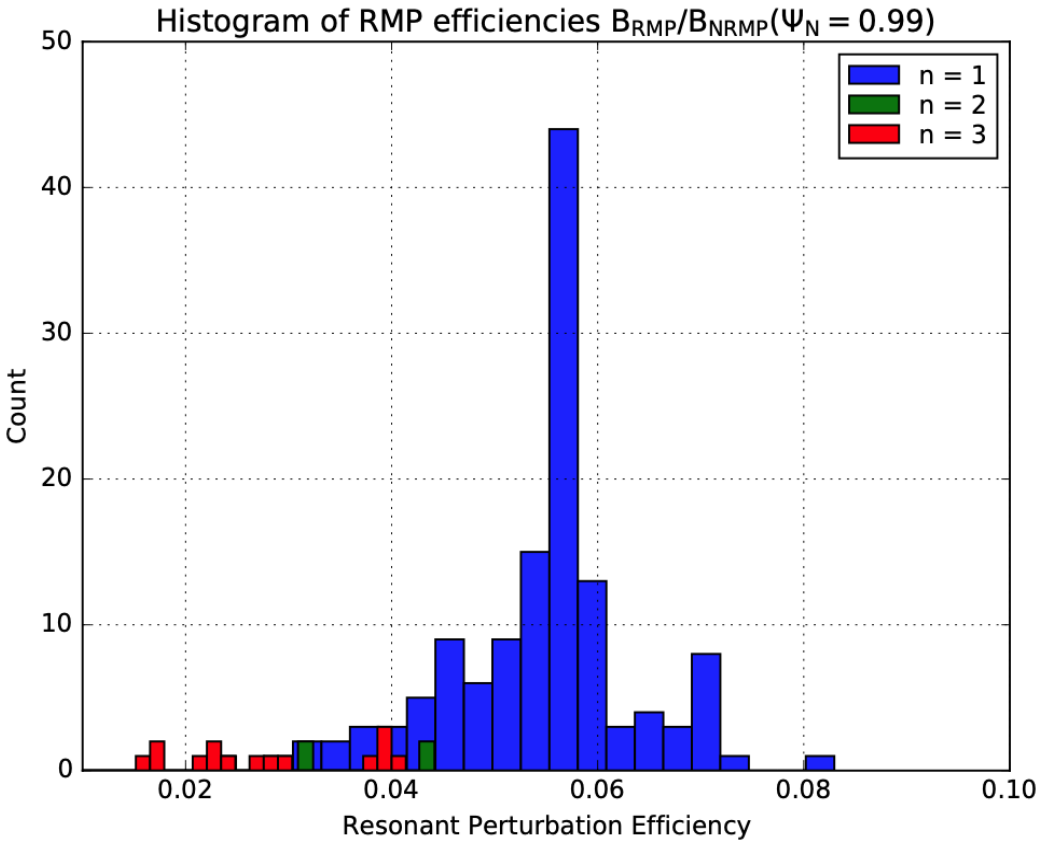

Figure 20: Magnetic perturbation efficiencies for the n=1,2,3 toroidal modes at Ψ_N=0.99.

TRANSP Analysis for Fast Ion Losses

TRANSP runs were attempted to assess the validity of the empirical fast ion loss term ($P_{F,Loss}$) shown in eq. 4. In addition, slowing-down time profiles are calculated to inform the choice of a smoothing time window for the neutral beam injected power. Although TRANSP runs were attempted for all 192 discharges in this database, only 45 converged to a solution. The failures were mostly due to the lack of good edge CER data and a lack of quality impurity density profile fits. Figure 21 shows a comparison of the fast ion losses using the empirical DIII-

D equation and TRANSP calculated values. For high Ip, TRANSP and the empirical equation are in reasonable agreement. As Ip decreases, the agreement between the two methods quickly decreases till the empirical value is ~2 times less than the one predicted by TRANSP. This relation is more clearly seen in figure 22, which shows the fraction of loss power to neutral beam injected power. For the rightmost points, 16% of the injected power is predicted to be lost compared to ~30% when using TRANSP. These results cast doubt on the accuracy of the empirical scaling representing actual losses, even when compared to TRANSP, which does not include the effects of 3D fields. Given that TRANSP is unable to be run on the entire database without considerable work and that the empirical equation is shown to generally agree with (or underpredict) these losses when compared to TRANSP, it is decided to continue to calculate the $P_{F,Loss}$ term with the stated algebraic equation. Any attempt to predict these values with reasonable accuracy given the 3D fields would scale to years of computational time when tackled on the database scale.

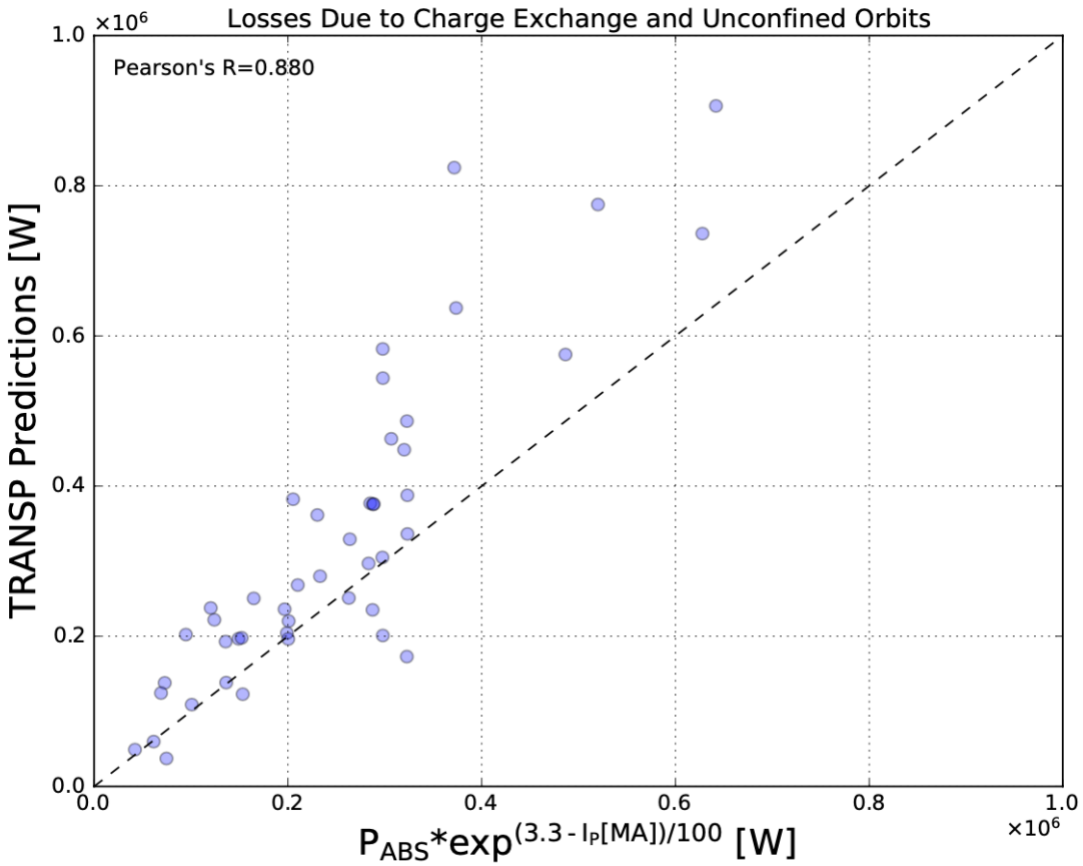

Figure 21: The empirical fast ion loss term used to report $P_{F,Loss}$ values for DIII-D to the 2008 ITPA database is shown on the x-axis. TRANSP calculated values are shown on the y-axis, with the 1:1 line shown in black. For losses less than ~0.3 MW, there is decent agreement. As Ip decreases, the agreement between TRANSP and the empirical model worsens.

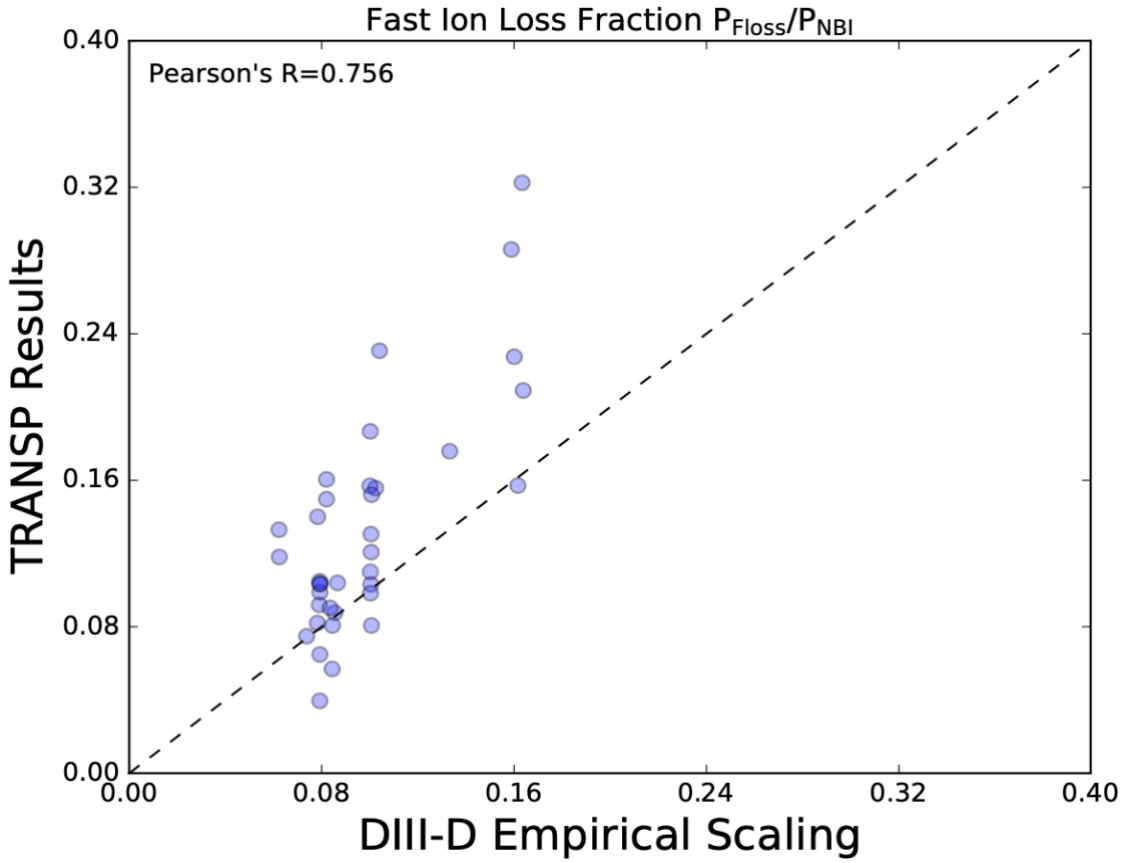

Figure 22: Fast ion losses shown as a ratio of the loss to the input power. Most cases show at least an 8% loss, with some reaching over 30% when TRANSP predictions are taken. TRANSP does not currently account for RMP effects, which have been shown to increase fast ion and prompt neutral beam losses drastically.

Lastly, profiles of the slowing-down times for injected particles are calculated just before the L-H transition. Slowing-down times across the center of the profile, corresponding to a normalized toroidal flux coordinate of 0.5, are averaged just before the transition. In this region, the slowing-down time is 60-100ms across the completed runs. Using this, a gaussian causal smoothing window of 100ms is applied to the neutral beam signal to simulate this characteristic time.

Comparison to the Martin Scaling

First, the new database will be compared to the Martin scaling before potential improvements are made. 3D field data was not supplied to the original 2008 ITPA database, so it is unclear the magnitude to which EFC was being used in the devices. Because of this ambiguity, the database analysis is split into three parts: shots with no RMPs, those with RMPs from EFC, and those with deliberate RMP ELM suppression.

Database with No RMPs

From the conditioned database, 20 L-H transitions happened without RMPs of considerable magnitude, regardless of the source or mode. These transitions are compared to the Martin scaling prediction in figure 23, with $P_{Loss\text{-}08}$ being calculated using eq. 3.

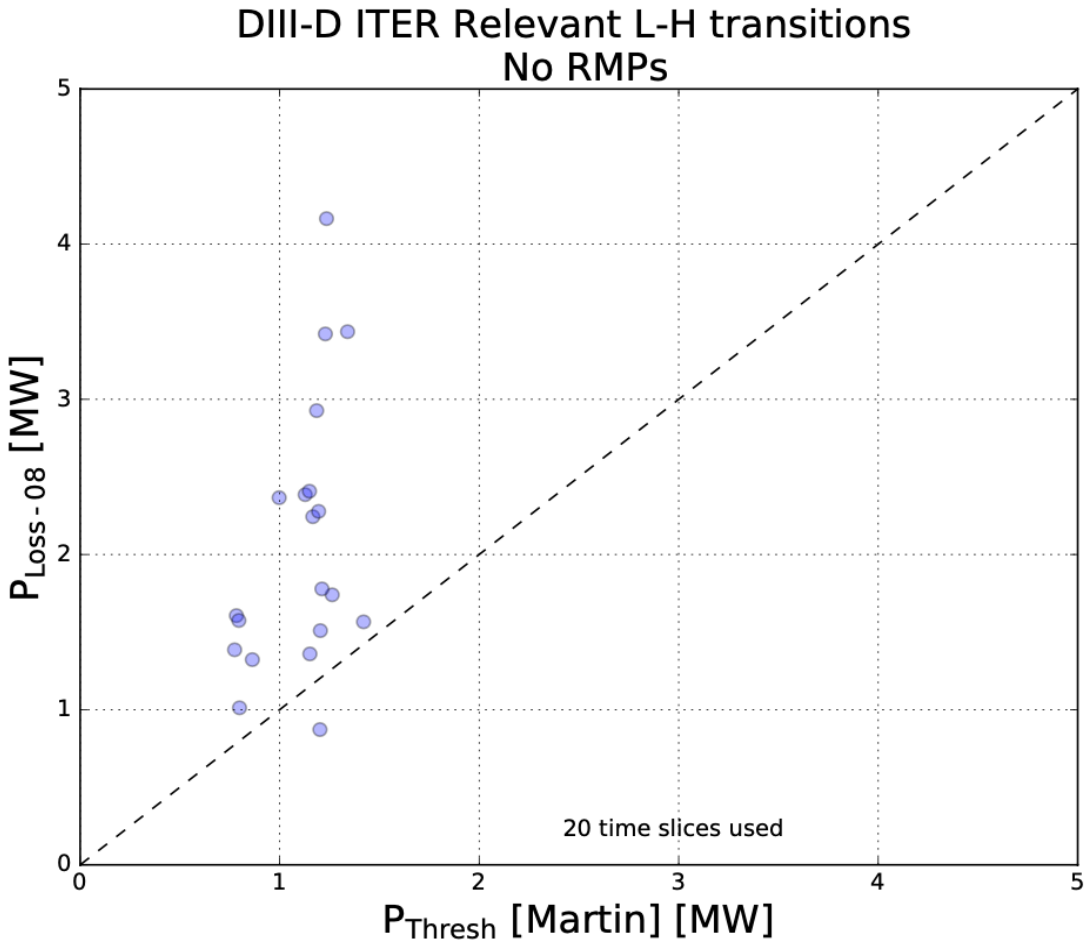

Figure 23: 20 L-H transitions that occurred without RMPs. The x-axis is the transition power predicted by the Martin scaling, and the y-axis is the actual power at the transition. Most of these took two times the predicted power, with one discharge taking four times.

Even in this ideal comparison, some transitions take 4 times the predicted power to transition into H-mode. A non-linear least squares regression to the same 0-D variables used in the Martin scaling results in eq 7., which looks similar to the original scaling eq. 5., although with much larger uncertainties in the exponents. This fitting has a root mean square error (RMSE) of 81% and predicts an H-mode threshold power for ITER (B_T = 5.3T and S = 678m^2) at half density (n_{e20} = 0.5) to be 72 MW, a 40% increase over the Martin scaling prediction.

$$P_{Thresh,no\ RMP} = 0.12 * e^{\pm 17.3} * {B_T}^{0.90\pm0.74} * {n_{e20}}^{0.71\pm0.49} * S^{0.83\pm4.36} \text{ (eq. 7)}$$

Interestingly, most of this subset takes 2-3 times the predicted power to transition. This is in contrast to the original database that has DIII-D having an average power ratio close to 1. Figure 24 is an overlay of the entire 2008 ITPA database used for the Martin scaling shown in red, with the DIII-D shots used in the old ITPA database shown in blue. The shots without n=1,2 or 3 RMPs from this reduced database are overlaid and show a substantial increase in the average power required to transition into the H-mode. Potential reasons for this discrepancy are considered in the discussion section.

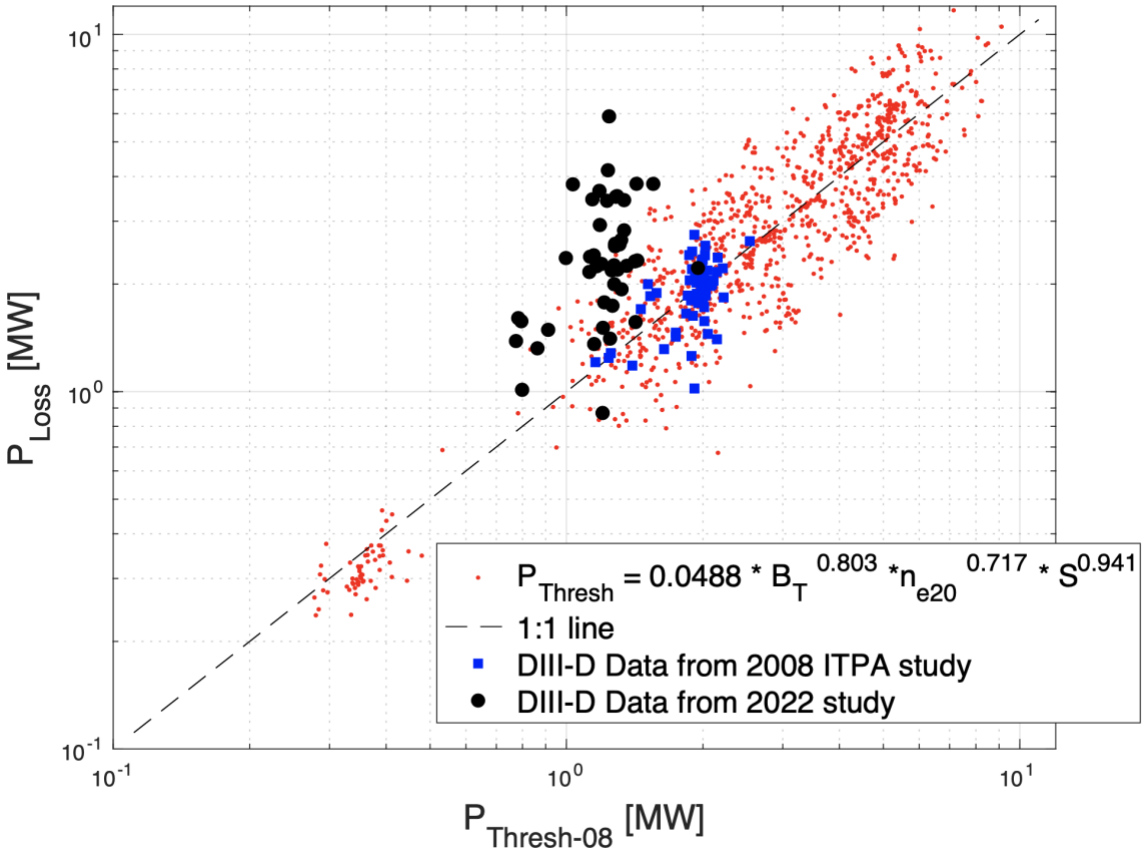

Figure 24: The original ITPA database is shown as red dots, with the blue squares corresponding to the DIII-D data. A subset of the new DIII-D database without any RMPs is overlaid as black circles. The average discharge in the new database took ~2 times the predicted power to transition in H-mode.

It is well known that the H-mode power threshold has a non-monotonic density dependence such that the density is split into a "low" and "high" branch, with a minimum in P_{LH} found at the crossover [23, 33, 34]. [17] discusses potential reasons for the increase in P_{LH} to either side of this minimum. To handle this dependence, the 2008 ITPA database study excluded DIII-D discharges that had an L-mode density lower than $0.2 \times 10^{20}\ m^{-3}$ so that only the high-density branch was modeled. Figure 25 shows the ineffectiveness of this scaling in the low-density branch of DIII-D. As the line-averaged electron density decreases, the agreement between experimental measurements and the empirical prediction quickly falls off.

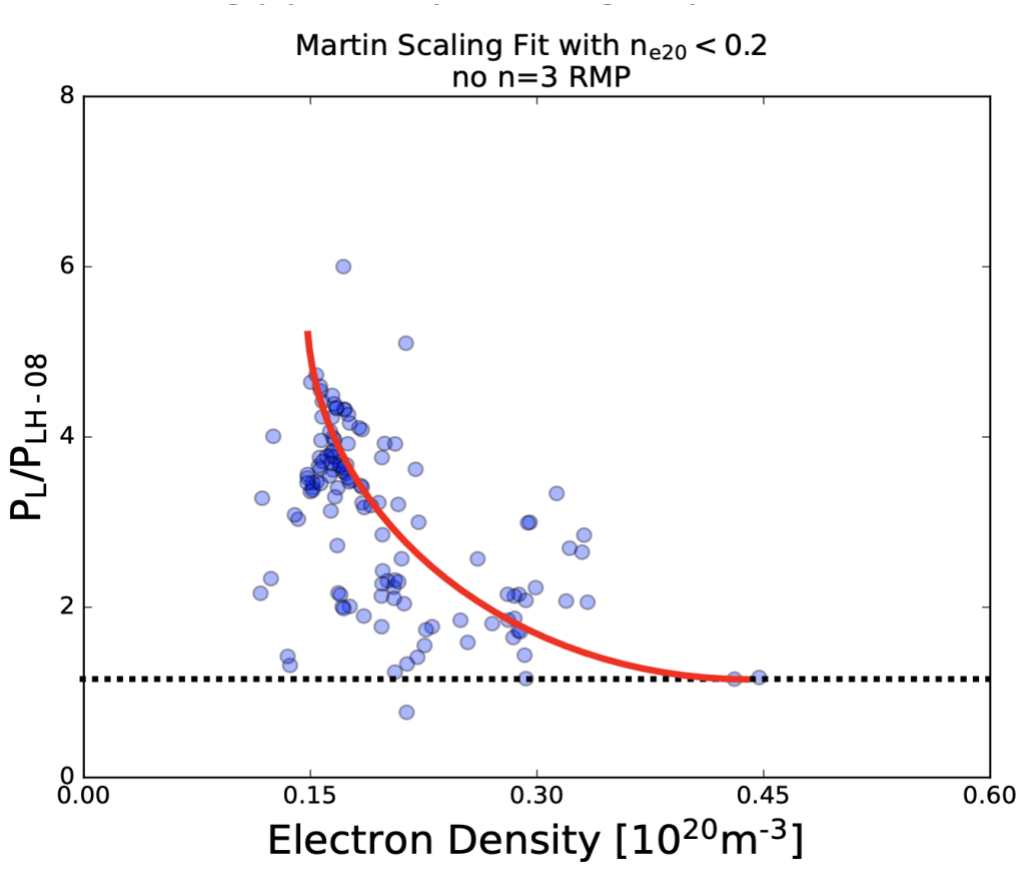

Figure 25: Power ratio vs. electron density for L-H transitions in this database. The red line is to guide the eye and highlights how the scaling breaks down in the low-density branch. This is due to both the non-monotonic density dependence of P_{Thresh} and the original scaling only being fit to the DIII-D discharges with an L-mode density greater than $0.2 \times 10^{20}\ m^{-3}$.

Database Including n = 1 & 2 RMPs from EFC

Although there were no RMP ELM suppression discharges during the time of the 2008 study, EFC was still present on most machines. In DIII-D, EFC fields primarily produce n = 1, with some secondary n = 2, RMPs as a result of attempting to correct the non-axisymmetric irregularities of the machine's field due to the misalignment of coils. From this, a logical comparison would be to next include transitions with n = 1 and 2 RMPs. This subset corresponds to 44 transitions out of the reduced database. Figure 26 shows these transitions plotted against the Martin scaling, again showing a factor of 2-3 increase in the transition power compared to that predicted. The scaling predicts a majority of DIII-D discharges to take 1-2 MW to transition into H-mode, but they often take 1-4MW instead.

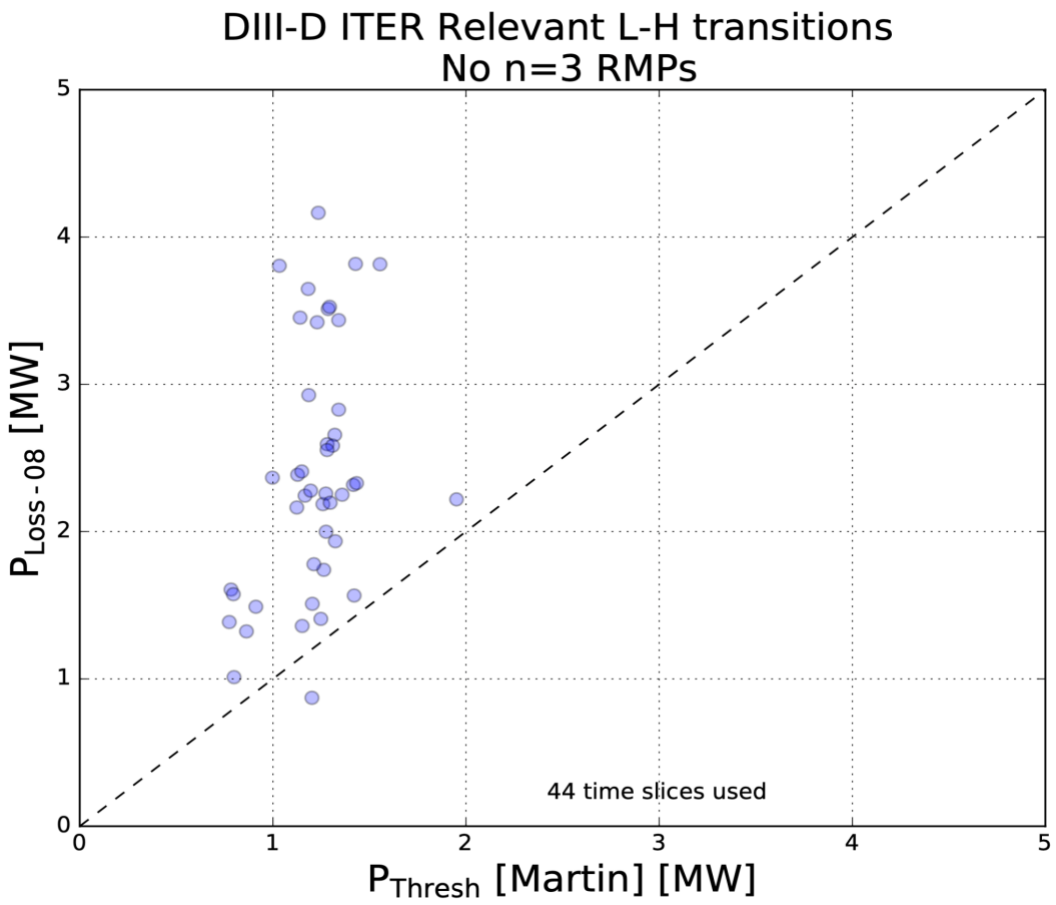

Figure 26: 44 L-H transitions where only n=1 or n=2 RMPs are present. A similar spread is seen where most transitions take 2-3 times the power predicted by the Martin scaling.

Again, a non-linear least squares regression is done to represent this data and is shown in eq. 8. This fitting notably deviates from the previous one and by extension, the Martin scaling. The RMSE is 81%, and the large surface area exponent makes extrapolation to ITER unreasonable, 29 GW. The correlation between parameters ranges from 0.2-0.4, except for that between the coefficient 'A' and the plasma surface area, which has a perfectly negative correlation.

$$P_{Thresh,no\ n=3\ RMP} = 5.1x10^{-6} * e^{\pm 10.35} * {B_T}^{0.52\pm0.33} * {n_{e20}}^{0.52\pm0.21} * S^{3.37\pm2.60} \text{ (eq. 8)}$$

Database Including all RMPs

To see if the Martin scaling is affected by 3D fields, the entire conditioned database is compared in figure 27. These discharges have n = 1, 2, and 3 RMPs from both EFC and ELM suppression. Although a direct comparison to the Martin scaling to judge its effectiveness is unfair, any systematic shift in the data should be easy to spot when compared in this way. A regression analysis is done, and the resulting equation is shown in eq 9.

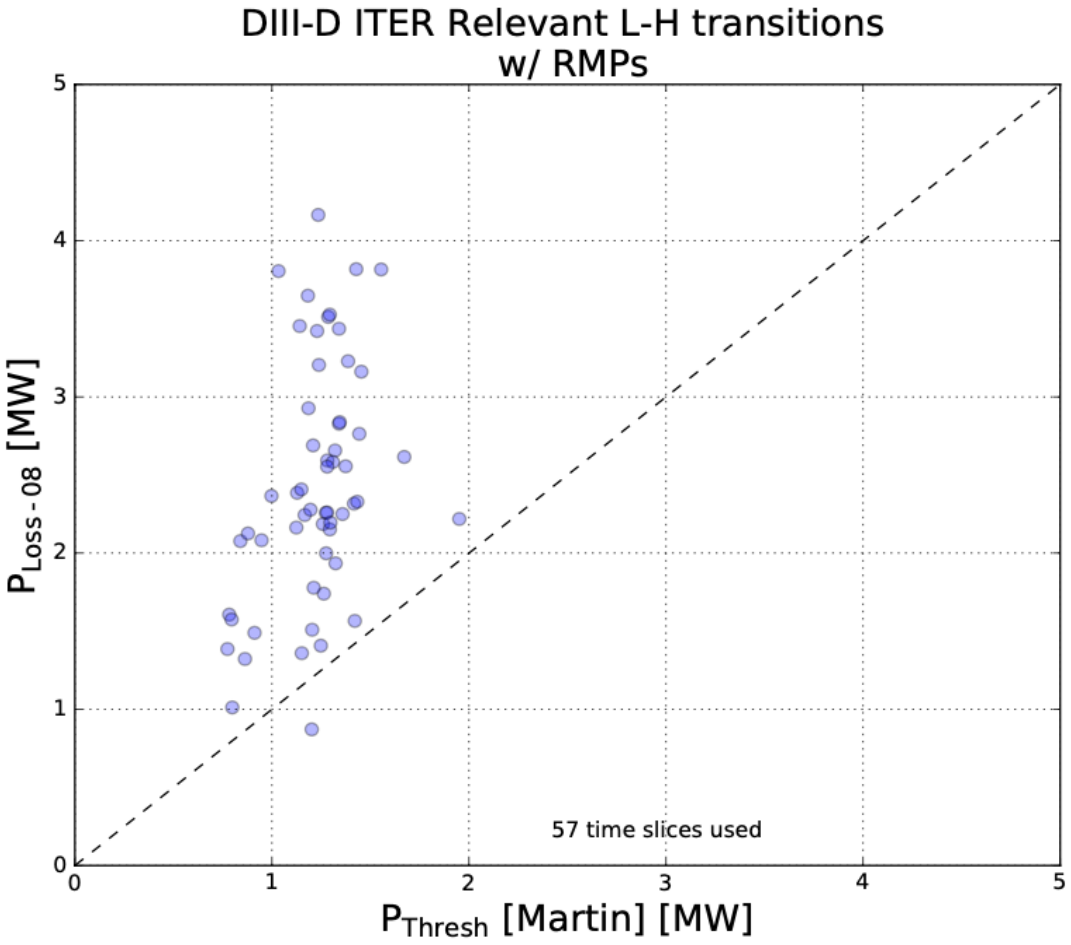

Figure 27: Full database of ITER relevant DIII-D L-H transitions, as determined by the 2008 selection criteria, including those with any RMPs present during the transition. These discharges show the same vertical and horizontal spread as the no-RMP and EFC-only subsets.

$$P_{Thresh,RMP} = 2.4x10^{-6} * e^{\pm 8.71} * {B_T}^{0.51\pm0.28} * {n_{e20}}^{0.52\pm0.18} * S^{3.56\pm2.19}$$ (eq. 9)

The RMSE for this fit is 73%, and the extrapolation to ITER is 47 GW. All parameters have a correlation from 0.2-0.3 except that between 'A' and the plasma surface area, which has a perfectly negative correlation. No systematic change in the power threshold was seen in the points with RMPs when compared in this way.

Fixing Plasma Surface Area Exponent

It is important to note that in this DIII-D database, the plasma surface area only varies from 49-55m^2, about 10%. In contrast, the density varies by a factor of 4 and the toroidal field by a factor of 2. Because of this, it may be appropriate to instead fix only the plasma surface area term from the original scaling. Redoing the previous fits in this way does not improve the RMSE, but it does result in ITER projections that more closely resemble the original estimates. The corresponding regressions are shown below.

$$P_{Thresh,no\ RMP} = 0.075 * e^{\pm 0.51} * {B_T}^{0.89\pm0.61} * {n_{e20}}^{0.708\pm0.45} * S^{0.941}$$ (eq. 10)

$$P_{Thresh,no\ n=3} = 0.079 * e^{\pm 0.28} * {B_T}^{0.59\pm0.34} * {n_{e20}}^{0.55\pm0.21} * S^{0.941}$$ (eq. 11)

$$P_{Thresh,RMP} = 0.080 * e^{\pm 0.24} * {B_T}^{0.57\pm0.28} * {n_{e20}}^{0.56\pm0.18} * S^{0.941}$$ (eq. 12)

3D Field Effects on the Power Threshold Using the Conditioned Database

The effect of 3D fields on the power threshold is explored using several branches of logic with a reduced database of ITER relevant discharges in the DIII-D high-density branch.

Fixing ITPA Database Parameters

In this section, the original scaling is taken as accurate in order to leverage the parameter space accessed by the 2008 ITPA study. The 3D field term is added, and regression is done on the data. Eq. 13 shows a result of this method where the 3D field exponent seems to have a strongly favorable scaling. However, this approach is flawed (RMSE is ~1900%) as it assumes the original scaling accurately represents the data, which it is shown not to in figure 27. With this scaling, and $\delta b/B_T = 4x10^{-4}$ for ITER, an H-mode power threshold is projected to be 2MW – unreasonably small. For this reason, this method is discarded in subsequent sections.

$$P_{Thresh} = 0.0488 * n_{e20}^{0.717} * B_T^{0.803} * S^{0.941} * (1 + \frac{\delta B_{RMP}}{B_T} x10^4)^{-1.9} \, [MW] \; (eq. 13)$$

Full Parameter Fits

In this section, all scaling parameters are free to be fit, and the dependence of the power threshold on 3D fields is assessed. Equation 14 shows the result of this regression, and figure 28 is the corresponding plot. For brevity, uncertainties in the exponents are left out, and the 3D field terms are put into shorthand notation where $B_{R,3} = 1 + \frac{\delta B}{B_T} x10^4$ is the resonant n = 3 component with the other terms following the same format. The RMSE for this regression is 70%, and the

uncertainties are large in the n = 1, 3 non-resonant and the n = 3 resonant components. As expected, the resonant and non-resonant components for each toroidal mode are inversely correlated.

$$P_{Thresh} = 5x10^{-5} * {B_T}^{0.58} * {n_{e20}}^{0.40} * S^{2.79} * {B^{0.11}}_{R,3} * {B^{-0.18}}_{NR,3} * {B^{0.22}}_{R,1} * {B^{-0.14}}_{NR,1}$$

(eq. 14)

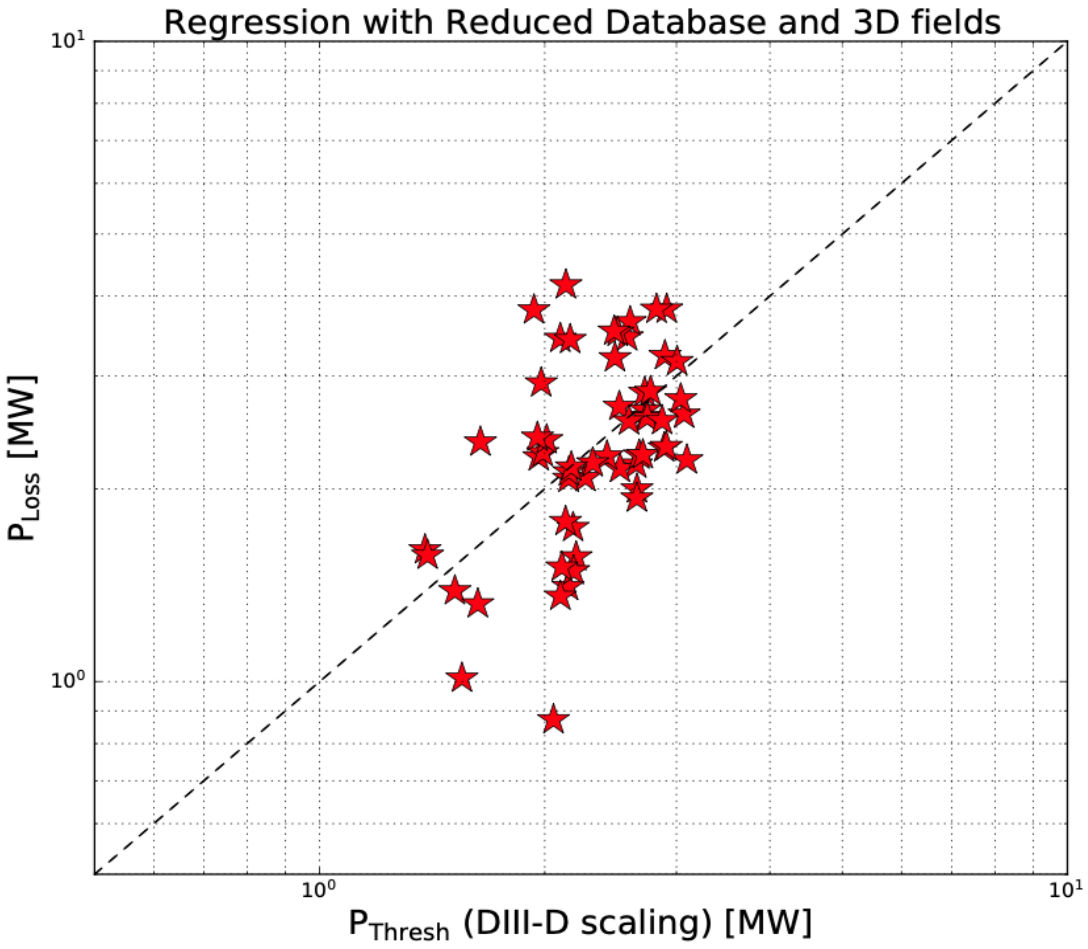

Figure 28: Loss power vs. the L-H power threshold scaling shown in eq. 14 for the points used in the regression. Even with this specialized DIII-D database, a factor of 2 difference between the predicted and the actual power threshold is seen in some points.

3D Field Effect on the Non-monotonic Density Dependence of P_{LH}

It is generally accepted that there is a density for which the power threshold is minimized if all other parameters are fixed. On either side of this minimum, the power required to access H-mode increases. The exact location of this minimum varies by machine, and even within a single machine can change with the main ion species, type of heating (NBI/ECH), neutral beam injected species, and Ip [23]. It is the goal of this section to determine the effect of RMPs and NRMPs on this minimum.

As mentioned, this density minimum is sensitive to many parameters that can easily vary between discharges. For this reason, a subset of discharges is selected, whereas many of these variables are matched as possible. A large grouping of transitions in this database occurs with a plasma current of 1 MA and forms the selection pool for this study. Then, only neutral beam heated transitions are kept. As a baseline, transitions without 3D fields in this subset are fit and shown in figure 29**.** On the y-axis is P_L normalized to 2T to increase the data available [33]. Based on previous studies, it is assumed that the P_L vs. density curve is quadratic [23**,** 33**,** 34].

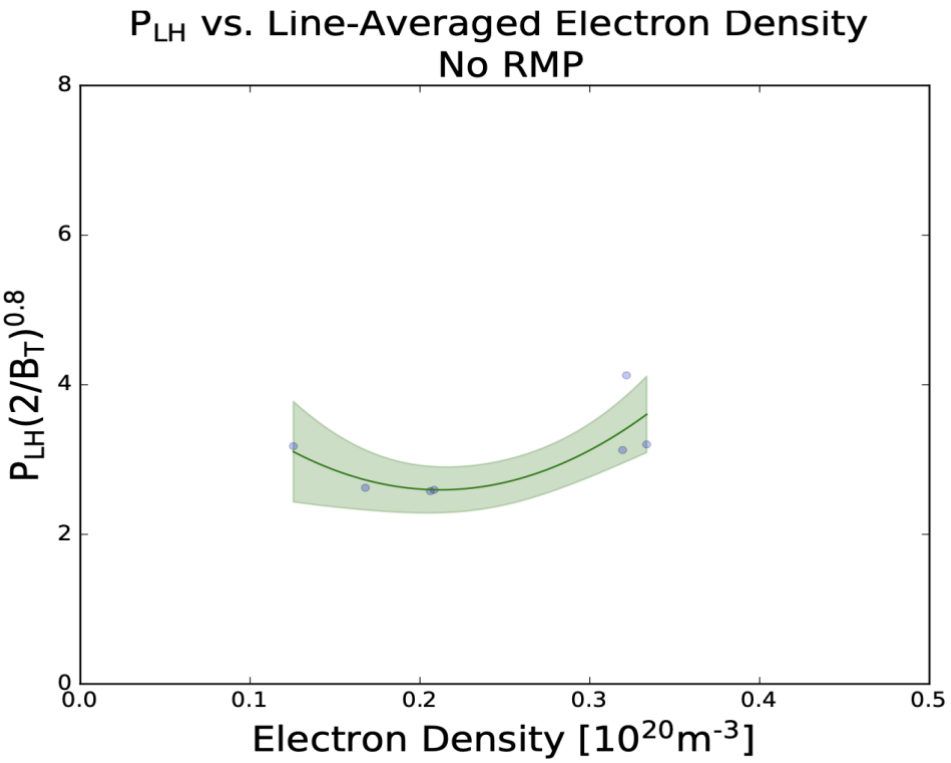

Figure 29: L-H power threshold (normalized to 2T) as a function of line-averaged electron density. A fit to these points is shown with the green shading being uncertainties in the fit. A quadratic fit is assumed, with the minimum occurring around $n_{e20} = 0.2$. All transitions here have no RMPs.

This same routine is repeated but with transitions that have n=1,2, and/or 3 RMPs and is seen in figure 30. Unfortunately, there is not enough data in this restricted range to do a sensitivity analysis of this minimum to the various toroidal modes or amplitudes, although all of the relative amplitudes seen here are ~$1x10^{-4}$. Looking at the fit, the minimum is not drastically different from the case where there are no RMPs. The density value at the minimum appears to be around $0.2x10^{20}$ m^{-3}, and the corresponding power is about 2MW.

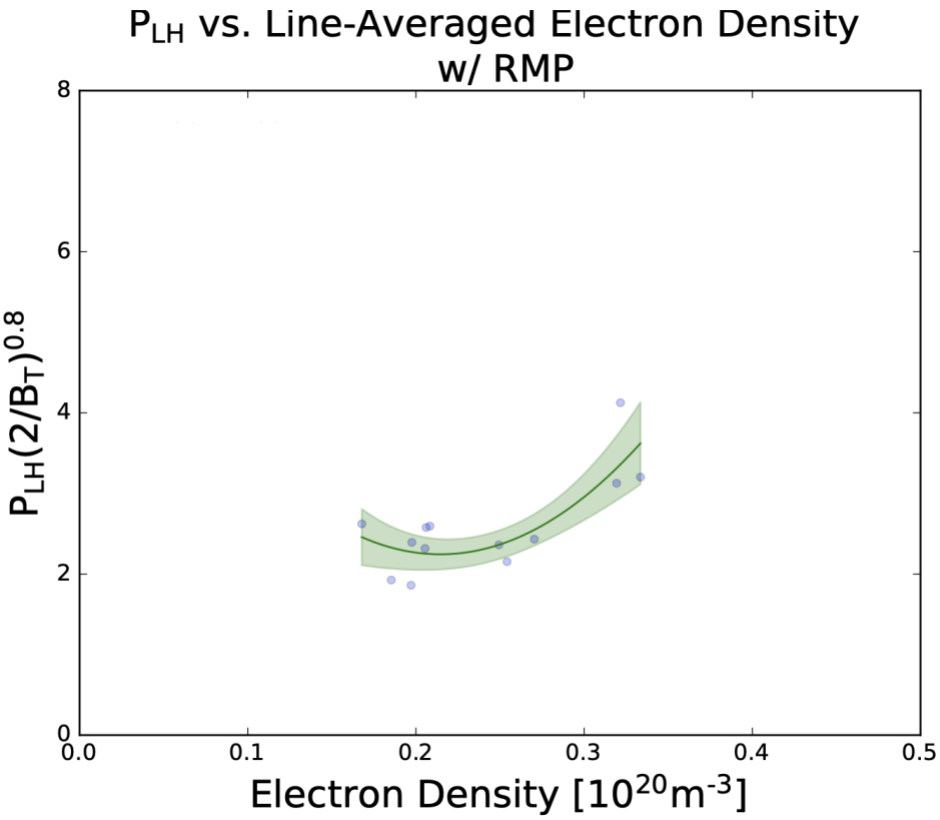

Figure 30: L-H power threshold (normalized to 2T) as a function of line-averaged electron density. A fit to these points is shown with the green shading being uncertainties in the fit. A quadratic fit is assumed, with the minimum occurring around n_{e20}=0.2. Transitions here have a mix of n=1,2, and 3 RMPs with a relative magnitude of ~1x10^{-4}.

3D Field Effects on the L-H Power Threshold Using the Full Database

Refitting using the entire database and the updated P_{Loss} term (with the core radiated power subtracted and fast ion losses neglected) does not grant any decrease in RMSE, but it does drastically increase the uncertainties in the exponents. For example, when only removing transitions in the DN configuration, those with the ion ∇B drift direction away from the X-point and those in the low-density branch results in the fitting shown in eq 15. with an RMSE of 73% but uncertainties upwards of 500% and in the case of the surface area component, almost 2200%.

$$P_{Thresh,no\ n=3} = 5.31 * e^{\pm 9.07} * {B_T}^{0.05\pm 0.31} * {n_{e20}}^{0.40\pm 0.20} * S^{-0.11\pm 2.28}$$ (eq. 15)

Refitting and including the low-density branch drastically increases the uncertainty in the density exponent (to ~400%) as expected.

Other Trends and Database Observations

Non-monotonic Density Dependence of P_{LH}

Several tokamaks have shown a non-monotonic density dependence of P_{LH}, and how this density minimum changes with various parameters [23**,** 33**,** 34]. The dependence of this minimum on plasma parameters (elongation, Ip, X-point height, inner/outer gap, q95, etc.) is examined for this database. Of all of the parameters, only the plasma current showed any systematic trend. For increasing plasma current, an increase in both the minimum threshold power and the density at which this minimum occurs is observed, which is consistent with [33]. Figure 31 shows the full L-H transition database, colored by the plasma current.

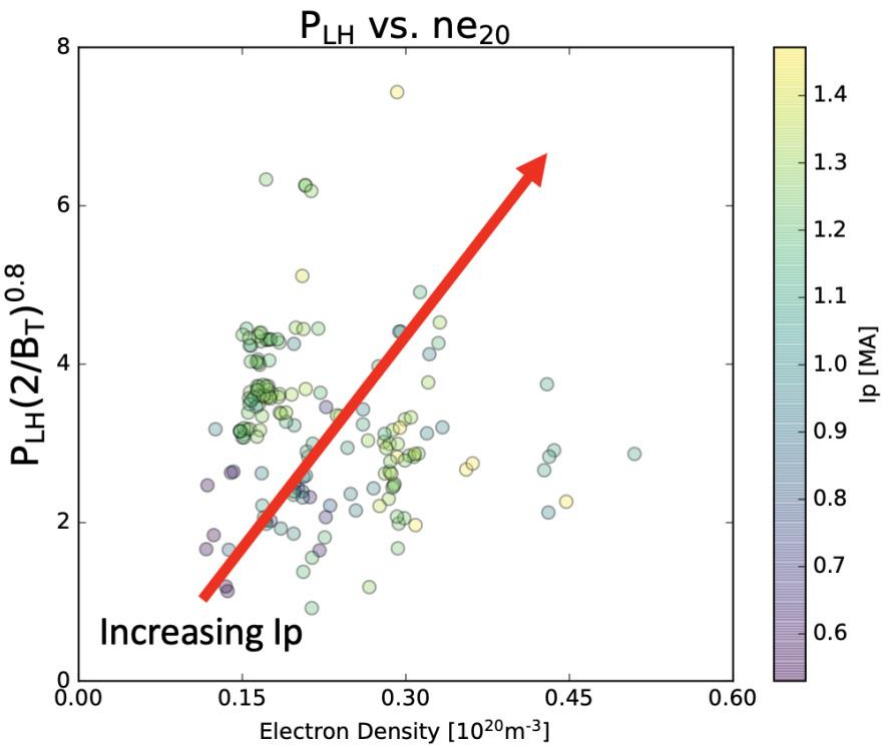

Figure 31: L-H power threshold (normalized to 2T) as a function of the line-averaged electron density with the points colored by the plasma current. As Ip increases, the minimum threshold power, as well as the density at which the minimum occurs, increases. The clarity of the Ip trend speaks to the potential significance, despite the variety in operating scenarios.

Dependence of P_{LH} on the Main Ion Species

The few cases in this database where the main ion species is not deuterium do not give a wide enough span in parameter space to do any meaningful regression. Instead, the correction factor to account for the main ion mass is assessed. This correction term of $m = 2/A_{eff}$ is added to the Martin scaling to account for the scaling being done with deuterium plasmas [59]. This factor considers the A_{eff} of the main ion and treats it as a multiplier, doubling the transition power for hydrogen and reducing it by a factor of 2 for helium. Figure 32 shows the database spread for the power ratio for each main gas species found in the database, with the average power ratio for deuterium being 2.6, 4.9 for hydrogen, and 1.6 for helium. These trends are approximately

consistent with the correction factor, despite zero conditioning of this database and a large spread of plasma parameters.

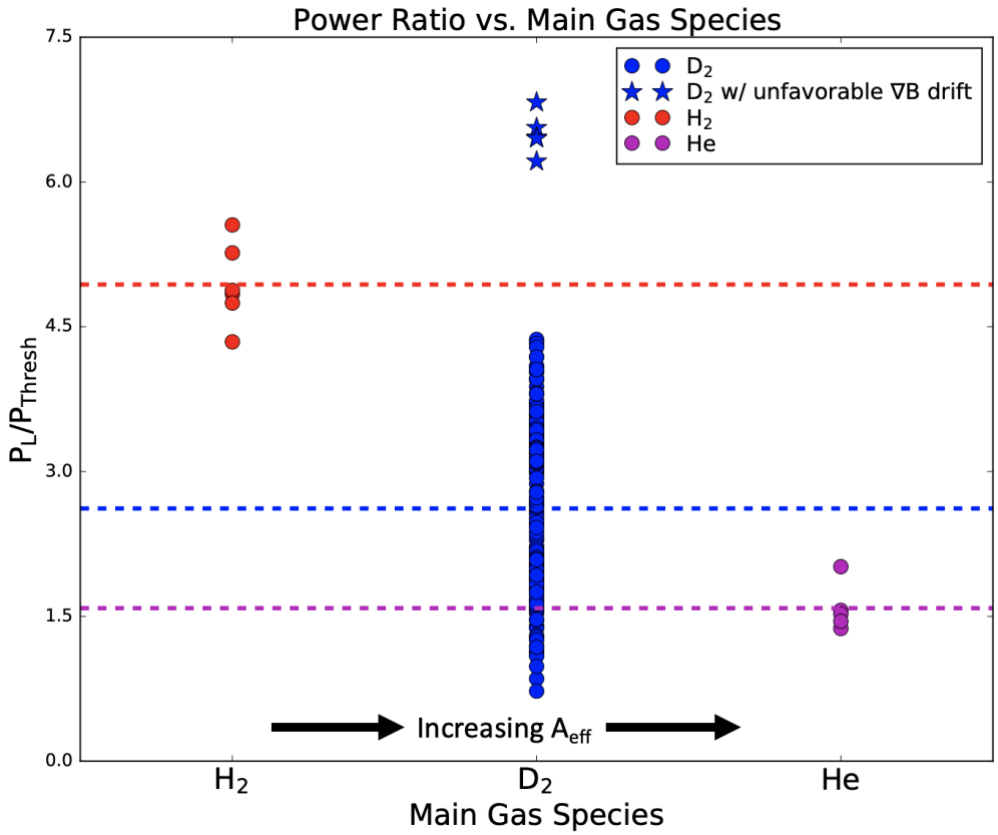

Figure 32: Power ratio of $P_{Loss}/P_{Thresh\text{-}08}$ vs. main gas species, with the horizontal dashed lines representing the average power ratio for each species. The average power ratio for each species approximately follows the trend expected from the correction factor of $2/A_{eff}$. The blue stars are deuterium discharges with unfavorable ion ∇B drift showing ~2 times the average power to transition when compared to other deuterium shots.

Discussion

Systematic Differences Between Studies

A striking systematic difference between the DIII-D data in the 2008 ITPA study and the data presented here is that the new DIII-D database requires more power to access the H-mode on average. Figure 33 shows the power ratio of P_L/P_{Thresh} for the transitions in this database. Having a higher power threshold than predicted is not something unique to this database study. Previous DIII-D L-H transition studies that have been carefully planned and executed have also shown that the power threshold can be well above that predicted by the previous scaling when non-captured parameters are varied [22**,** 23**]**. Several potential reasons for this discrepancy have been identified, all of which are related to the plasma shape.

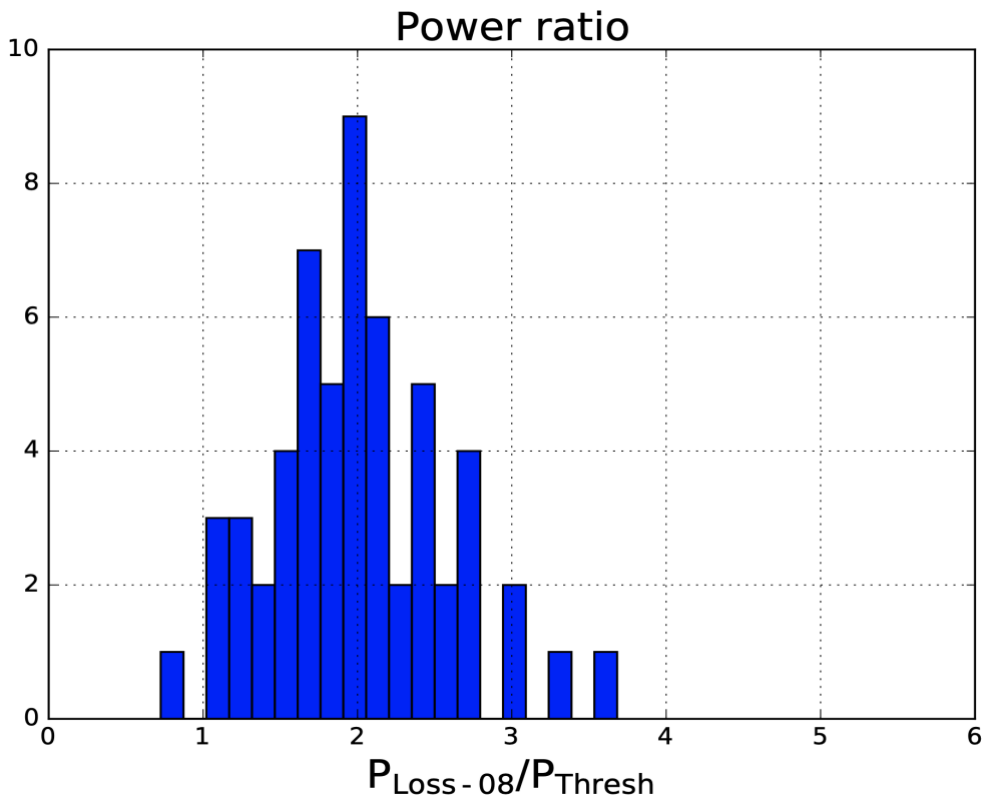

Figure 33: Histogram of the power ratio ($P_{L\text{-}08}/P_{Thresh\text{-}08}$) for this database. The average discharge took twice the power predicted to transition into the H-mode.

This database has an increased triangularity at the diverted end of the plasma and an overall smaller plasma surface area, both of which may be due to the addition of a baffle in the diverter region. Triangularity in this context is used to describe the shape of the poloidal cross-section of the LCFS. For an LSN plasma, the lower triangularity (δ_{lower}) is defined as $\delta_{lower} = \frac{R_{Geo} - R_{lower}}{a}$, where R_{Geo} is the geometric major radius, R_{lower} is the major radius of the lower X-point, and a is the minor radius of the plasma [60]. Table 4 shows the minimum, maximum, and average lower triangularities for LSN plasmas in this and the 2008 ITPA database. The average lower triangularity of this database is twice that of the previous one. Figure 34 shows two representative LCFS where the blue trace has a similar triangularity to the 2008 database, and the pink trace has a similar triangularity to this database. Triangularity is closely tied with the X-

point height, which has been shown to affect the L-H power threshold. Previous studies on DIII-D have shown that an increase in the X-point height leads to an increase in the H-mode threshold, sometimes by a factor of two, potentially due to an increase in the neutral particle recycling at the outer midplane [23].

Table 4: Lower Triangularity for the two databases.

	2008 ITPA DIII-D Database	2022 DIII-D Database
Minimum δ_{lower}	0.29	0.40
Maximum δ_{lower}	0.44	0.81
Average δ_{lower}	0.33	0.66

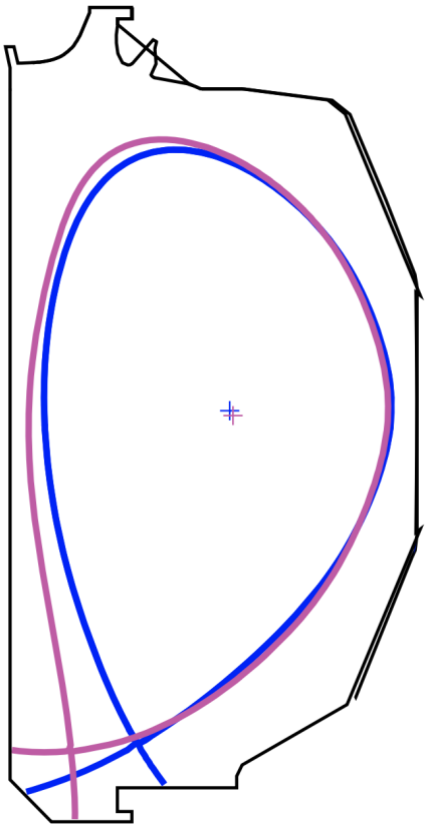

Figure 34: Two equilibria overplotted, both with an δ_{upper} of ~0.26. The pink trace has a larger δ_{lower} of 0.75 while the blue equilibrium has a δ_{lower} of 0.46. This difference in triangularity results in the pink equilibrium having a longer distance from the X-point to the floor directly below than the blue one.

The second systematic difference between the databases is the variation in plasma surface area. The plasmas in this database have a surface area from 49-55m^2, while the 2008 conditioned database has DIII-D plasmas in the 60-67m^2 range. This 20% difference in surface area may be partly attributed to the addition of a baffle in the DIII-D divertor region, as shown in figure 35. However, discharges in the non-conditioned 2008 database span from 47-66 m^2 and the reason for their exclusion is not obviously clear. The shot numbers in the 2008 study are in the 80000 range, this baffle was added around 124000, and the earliest shot in the current study is 139000.

A 25% decrease in the surface area gives an ~20% lower prediction in the power threshold if the Martin scaling is used.

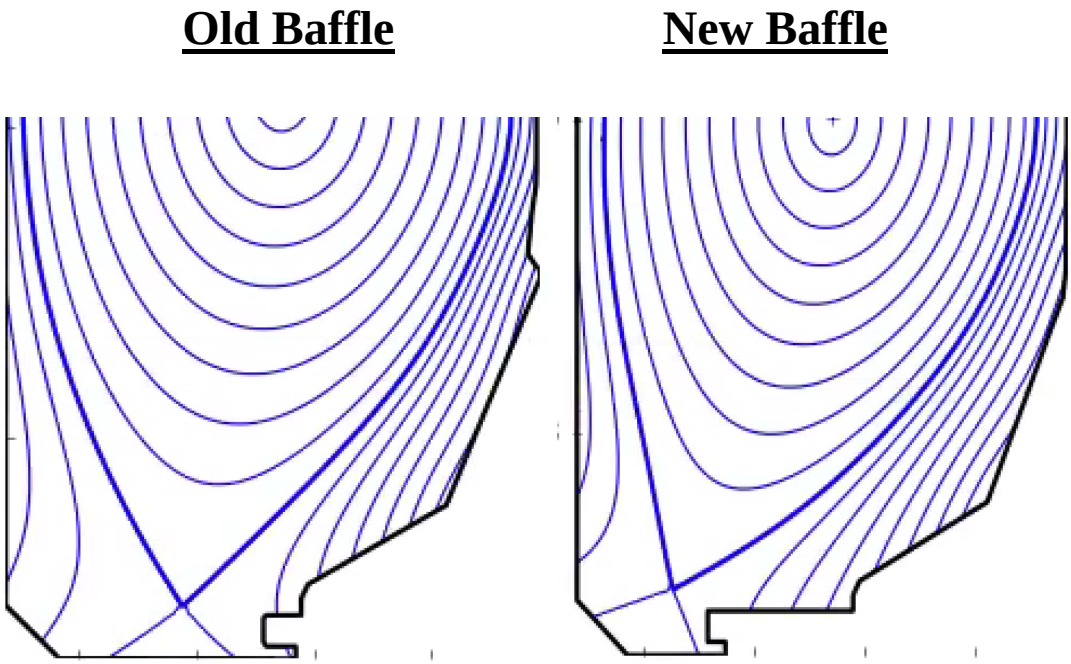

Figure 35: Two DIII-D discharges (84026 and 170072) showing the addition of the lower divertor shelf that happened around shot 124000. All discharges in this database happen after the addition of this extended shelf which may explain the systematic decrease in plasma surface area. An increase in triangularity is seen in the right equilibrium as a result of the baffle.

Potential Implications of Underpredicting the Fast Ion Loss Term

Estimates of the fast ion losses calculated using equation 4 are shown to generally agree with TRANSP values as Ip increases but underpredict these losses as Ip decreases (figure 21 & 22). 3D fields are shown to increase fast ion losses through several channels (prompt, charge exchange) and given that TRANSP does not include these 3D field effects, it is assumed that most estimates of the $P_{F,Loss}$ term are an underestimate. The implications of this underestimate would mean that the L-H transition power was overestimated in both this and previous studies. While this would seem a positive outcome, as the transition happens at a lower power than

expected, these losses would need to be reduced to see a difference. The reduction of these losses and alternate scenarios are topics currently being explored.

Differences Between Regressions With and Without 3D Fields

A noticeable difference is seen in the regressions when transitions with RMPs are added, regardless of the source or toroidal mode. The regression without any RMPs (eq. 7), resembles the original Martin scaling, while the subsequent regressions with RMPs (eq. 8 and 9) show a strong deviation in the surface area dependency, from 0.8 to 3.5. The range of parameter space accessed does not vary considerably between the different subsets of discharges (no RMP, n=1,2 only, etc.) so that is not the reason for the change. There are many possible sources for this change, but the most obvious would be from the 3D fields themselves. One potential explanation would be that 2D axisymmetric codes like EFIT actually underpredict the plasma surface area. Previous experiments and numerical modeling shows evidence for the deformation of the separatrix due to 3D fields [61]. This deformation would not be captured in any 2D axisymmetric code and could potentially mean a larger boundary which would give an underprediction of the power threshold if the 2008 ITPA scaling is used with 2D estimates of the plasma surface area. Additionally, RMPs are shown to increase fast ion losses drastically. If these losses are proportional to the surface area, then the threshold power should drastically increase with the presence of RMPs, which would explain the increase in surface area dependence.

RMP and NRMP Effect on the L-H Power Threshold

Despite the relatively large RMSE and uncertainties in the fits, trends seen in the regressions are discussed in the following section.

Dependence on the n = 3 Mode

Based on the regression shown in eq. 14, n = 3 RMPs can increase the power threshold by 15-25% when present in ELM suppression magnitudes (~3-6x10^{-4}) during the L-mode. An increase in the threshold of this size is consistent with previous work done with single shot comparisons [22]. The L-H power threshold seems to be more sensitive to the non-resonant n = 3 components. Considering the average non-resonant relative magnitude seen in figure 19 is ~1x10^{-4}, this corresponds to a decrease of 10-15%. However, in the cases with strong non-resonant components (~7x10^{-4}), the power threshold can decrease by 30%. Other work has also shown n = 3 NRMPs to decrease the power threshold, although the same reduction is seen with a smaller relative magnitude, potentially due to the vacuum approximation used here [63].

Dependence on the n = 1 Mode

Similarly to the n = 3 mode, the resonant n = 1 fields tend to increase the power threshold while the non-resonant components work to decrease it. However, in DIII-D, the n=1 mode differs from the n=3 mode in the power threshold sensitivity and the distribution of resonant vs. non-resonant field magnitudes. The regression shows that the power threshold is more sensitive to the n=1 resonant mode than the n = 3 resonant mode, as dictated by the difference in exponents (0.22 and 0.11, respectively). In addition to this, figures 17 and 19 display the distribution of relative magnitudes for the 3D field database. The n = 3 RMP magnitudes are

semi-uniformly distributed from 1-5x10^{-4} while the n = 1 RMPs are mostly situated around 2-2.5x10^{-4}, presumably the magnitude used for EFC. For the NRMPs, the average n = 3 component is low, around 1x10^{-4}. However, this distribution changes for the n = 1 mode, which has a broad peak around 3x10^{-4}. For the n = 1 RMPs with the mean magnitude, an increase of ~30% is seen, and for the NRMPs, a decrease of ~20% is seen for the mean relative magnitudes.

0-D Database Approach is Not Effective for L-H Power Threshold Scaling Laws

Despite the attempt to carefully curate a database to produce a robust DIII-D L-H transition scaling law, the best case regression has an RMSE of 70% with large uncertainties in the parameter exponents. The inability of these 0-D parameters to capture the physics at the necessary level is shown in several other ways. Figure 36 shows the rest of the database of L-H transitions overplotted on those used for the regression analysis. This dataset includes the entire density span and only excludes non-deuterium discharges, DN configurations, and those with an unfavorable ion ∇B drift direction. Although the full database largely falls within that used for the regression, using this full dataset for the regression leads to large uncertainties, averaging 300%, with an increase in RMSE. This is due to the lack of data conditioning that would normally filter out dissimilar scenarios. This regression is likely not applicable for other machines that access parameter space outside of that shown here, and possibly even those that do, as the surface area term is nearly cubed and would drastically affect the H-mode threshold prediction.

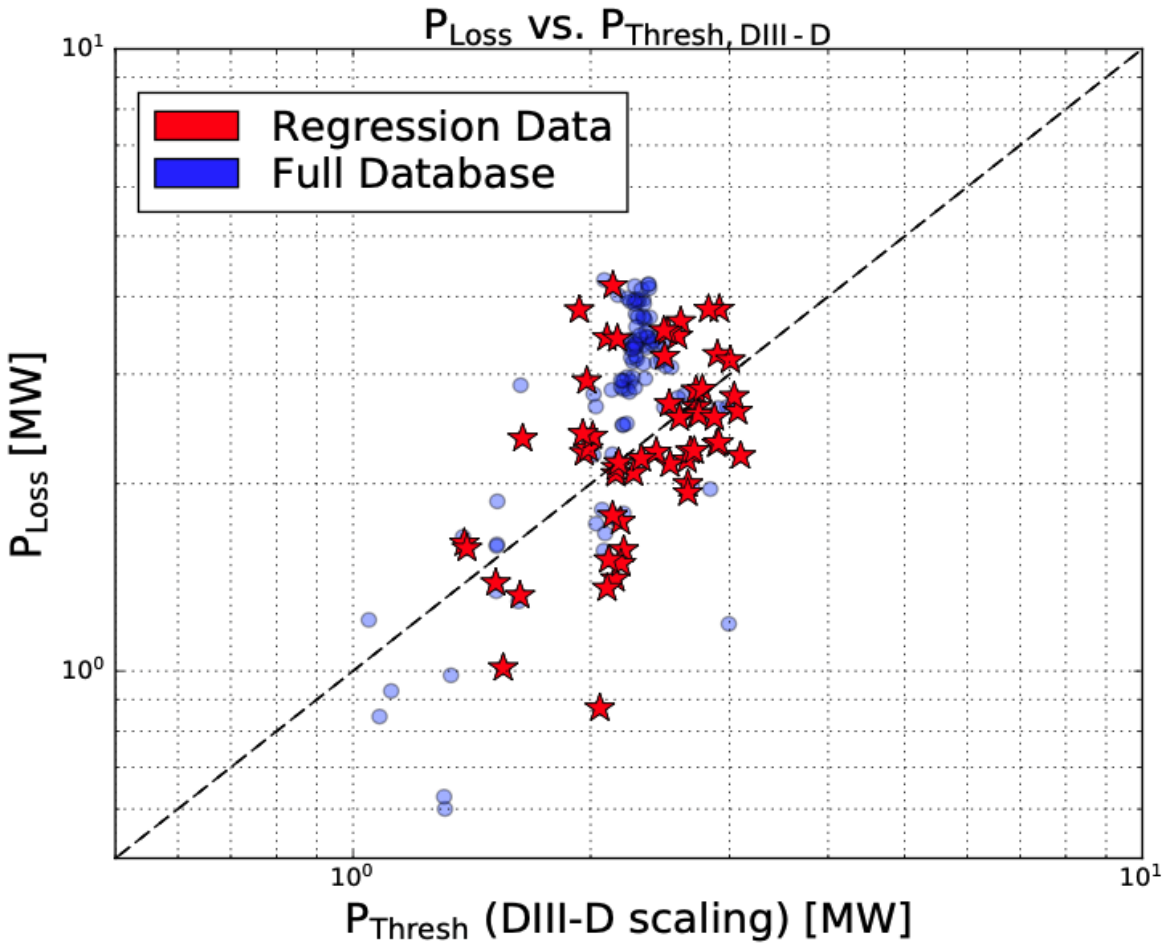

Figure 36: P_{Loss} vs. $P_{Thresh,DIII-D}$ for the entire database of deuterium discharges in a single-null configuration with favorable ion ∇B drift direction. The red stars are conditioned data used for the regression analysis, and the blue points are the rest of the database. Opacity of the blue points represents the number density of transitions in that region.

By comparing two discharges with nearly the same 0-D scaling parameters, it is shown that these values do not capture the physics necessary to reasonably predict the power threshold, even in a conditioned database. DIII-D shot 139979 and shot 139997 both have a predicted power threshold (from the Martin scaling) of ~1.25MW, but the first discharge transitioned with P_{Loss} = 1.4MW while the second transitioned at P_{Loss} = 4.2 MW. Both are neutral beam heated transitions, with nearly the same elongation and q95 value. The 0-D parameters used in the scaling for these discharges are shown in table 5. Two possible explanations for this difference

are the variations in X-point height and strike point location. The shot that transitioned with less power (139979) has an X-point that is ~5cm lower than its counterpart. [23] observed that for otherwise identical DIII-D discharges, the one with an X-point height ~16cm lower transitioned at a power half that of the other discharge. Although the direction of this trend is consistent with previous work, the magnitude of the effect observed here is a factor of 3 decrease. Furthermore, shot 139979 has a strike point that potentially hits the outer vertical divertor surface, whereas shot 139997 has a strike point that clearly strikes the bottom divertor floor. A study on EAST saw a drastic difference in ELM-ing characteristics as well as electron and current density profiles in the H-mode when the strike point was moved from a vertical to a horizontal surface [24]. Figure 37 shows the equilibrium of shot 139979 right before the L-H transition where the outer strike point is less than 1cm from hitting the bottom corner of the vertical face of the baffle. Given the accuracy of the 2D EFITs are on the centimeter scale [62] and that the corrugation of the separatrix from 3D fields is not accounted for, it is possible that this strike point actually hits the vertical surface. The strike point location may affect the L-H transition physics similarly to the X-point height, by modifying the neutral particle recycling and pedestal fueling characteristics. In addition to modifying fueling physics, the presence of an X-point has been shown to affect the flux-surface averaged Reynolds stress when compared to cases with no X-point [64**,** 65]. A reasonable extrapolation would be to consider that the location of this X-point could also modify this stress, which has been shown to be a key player in triggering the L-H transition [17].

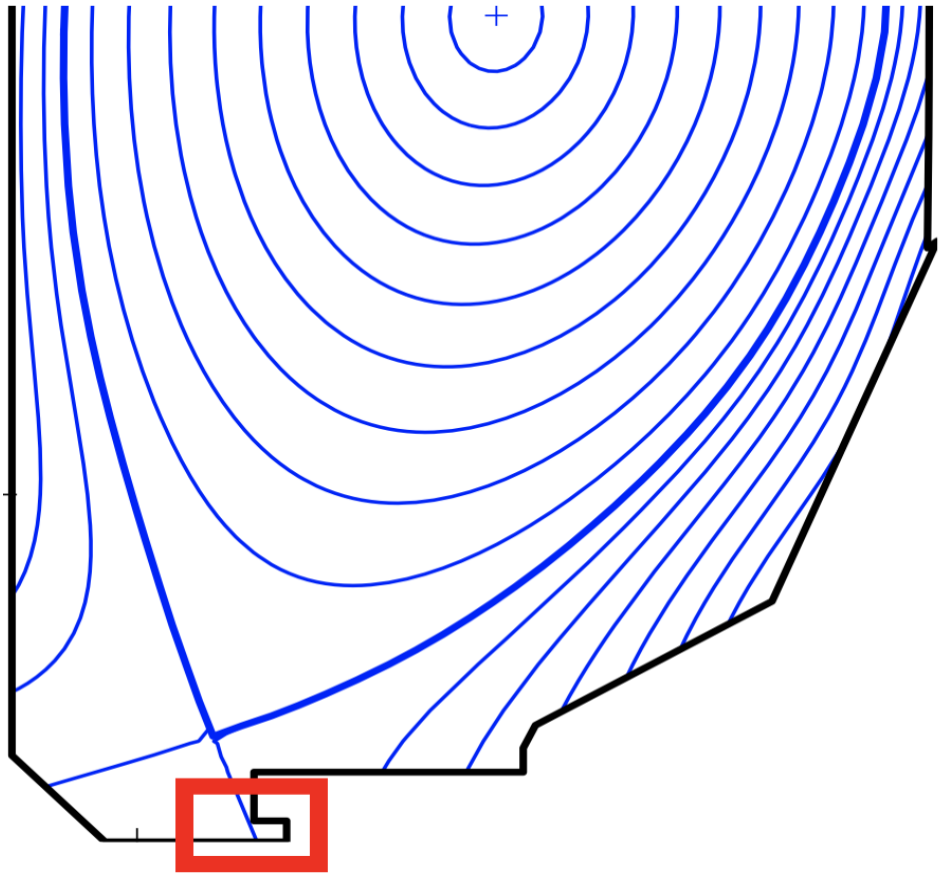

Figure 37: Equilibrium of shot 139979 that transitioned into the H-mode with power 3 times less than a comparable discharge. It is possible that the outer strike point actually strikes the vertical face of the divertor shelf (region in the red box), modifying the neutral particle recycling and reducing the L-H power threshold.

Table 5: 0-D parameter comparison for two discharges that transitioned at different powers.

shot	B_T	Plasma Surface Area	Density	$P_{Thresh-08}$	$P_{Thresh-actual}$
139979	1.7T	~54m^2	0.29x$10^{20}m^{-3}$	1.25 MW	1.4 MW
139997	2T	~54m^2	0.22x$10^{20}m^{-3}$	1.24 MW	4.2 MW

Even with the Martin scaling accessing a relatively wide range of parameter space, there still remains large uncertainty in the actual H-mode threshold for ITER. Figure 38 shows the

same plot from the original paper published in 2008 but plotted on a regular scale instead of a log-log. A rapid divergence from the prediction is seen as the power threshold increases, a feature also seen in the regression in this thesis. This is concerning given the needed extrapolation to reach ITER parameter space, as shown in figure 39. For a density of n_{e20} =1x10^{20} m^{-3}, the toroidal field of 5.3T, and a plasma surface area of 678 m^2, the 95% confidence interval spans from 45 to 160MW. Given the large uncertainty in this scaling, there is thus a risk that the heating systems in ITER may be insufficient to access the H-mode. Given the need for ITER to operate in H-mode in order to reach its stated goal of Q = 10, it would seem highly advisable to develop a physics-based understanding of the transition threshold sufficient to guide experimental planning for ITER.

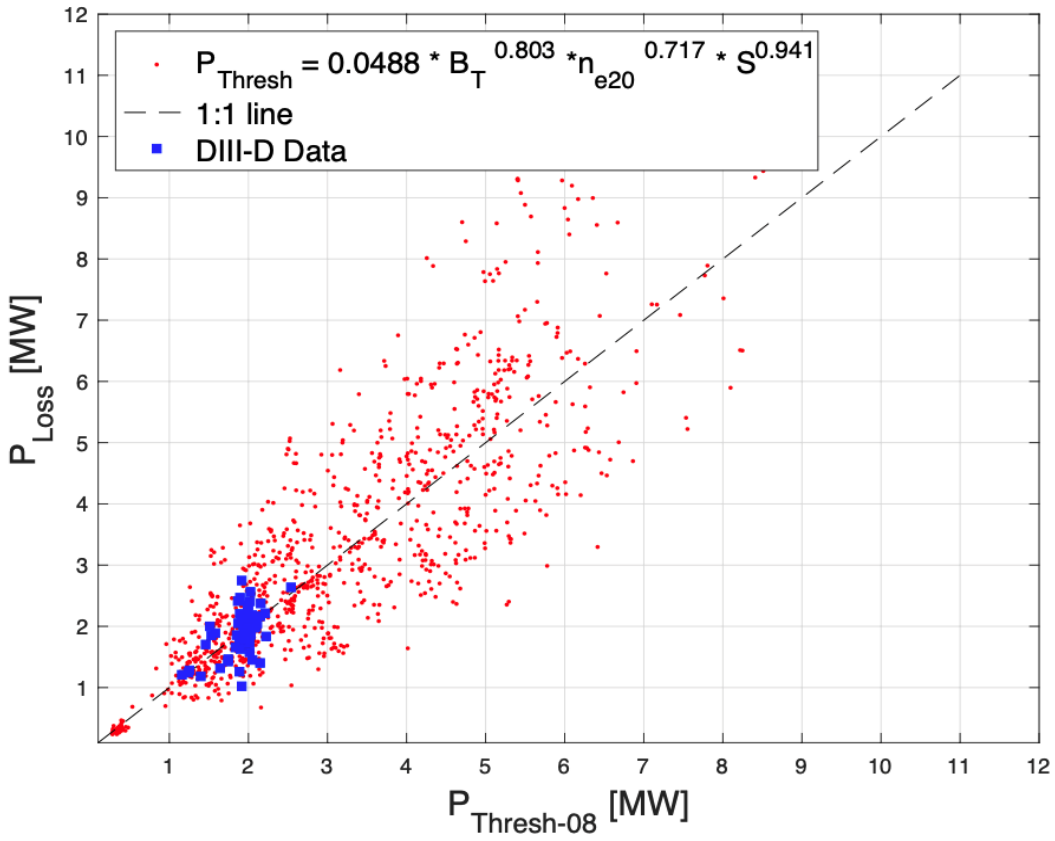

Figure 38: Loss power vs. L-H threshold power for the 2008 ITPA database study. To declutter the plot, the symbols that denote specific machines are removed (except for DIII-D). A rapid divergence from the prediction is seen as the threshold power increases.

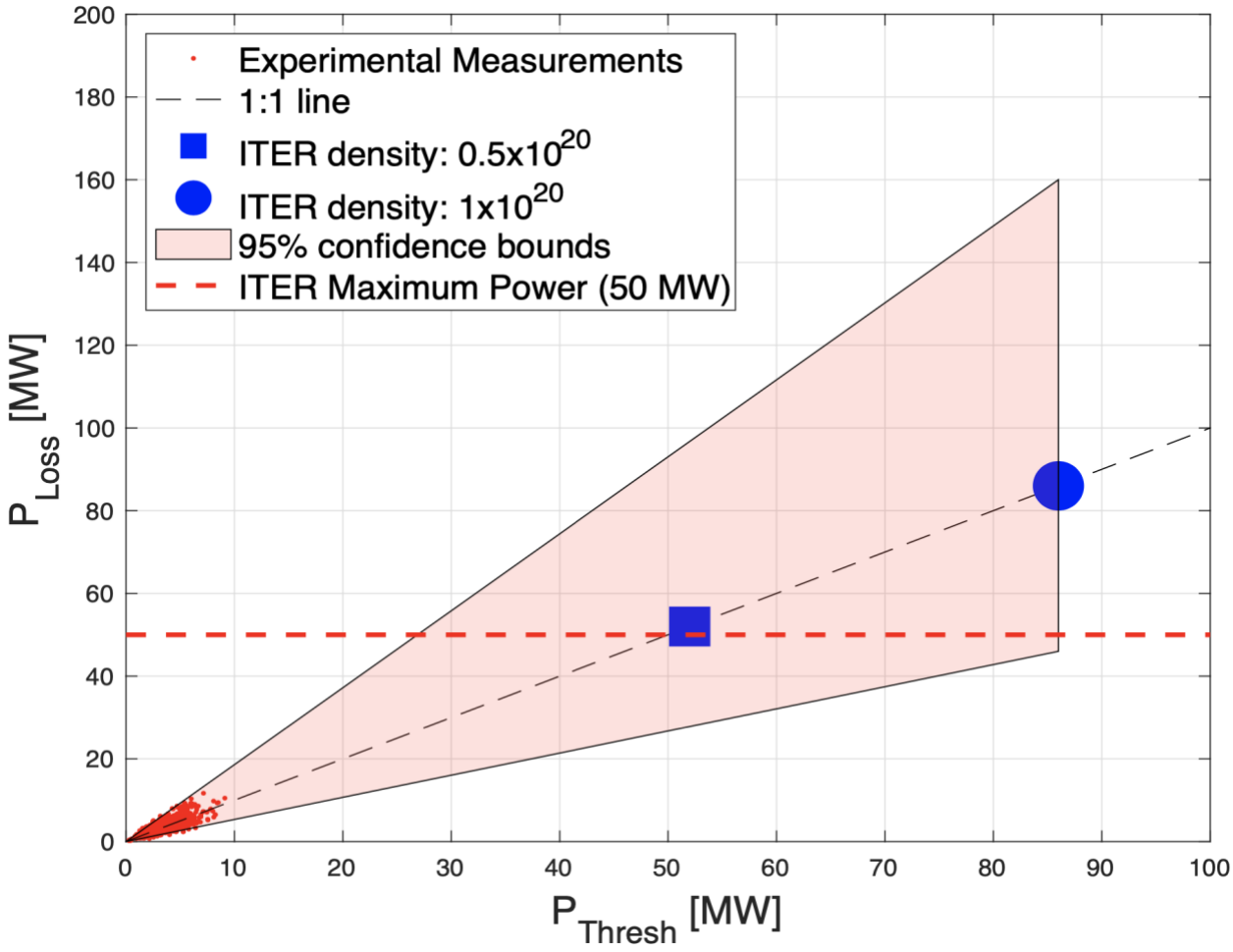

Figure 39: P_{Loss} vs. $P_{Thresh,08}$ for the 2008 ITPA database and the corresponding extrapolation to ITER, given the resulting scaling. The red dots in the lower left corner is the data used for the regression and the two blue points are potential ITER scenarios at various densities. The red shading is the 95% confidence interval, which spans from 45-160MW at n_{e20}=1x10^{20} m^{-3}.

Conclusion

In this study, we demonstrate that even when a database is carefully constructed and conditioned from a single device, a 0-D regression done in this way does not capture the necessary physics to produce a robust model for the prediction of the L-H power threshold.

George Box says: “Since all models are wrong the scientist must be alert to what is importantly wrong. It is inappropriate to be concerned about mice when there are tigers abroad.” If the regression is to be believed, it points to 3D fields having a small, but not-insignificant, effect on the L-H power threshold. However, it should be pointed out that other parameters have the ability to change the threshold by multiples, not percentages. Time since the most recent boronization, X-point height, ion ∇B drift direction, and heating method are a few examples of some of the major deciders in the L-H threshold. Experiments that look solely at individual mechanisms are important to understanding the underlying physics of the L-H transition, but if the goal is to build a device that requires H-mode operations in order to reach its scientific objective (e.g. Q=10), then an understanding of how each of these interacts with each other is essential. As an example, many studies have looked at the non-monotonic density dependence of P_{LH} and how it is affected by individual control knobs. It is possible that the combination of these observations in an operation scenario is not purely the sum of the individual effects, as the underlying physics is likely coupled. Similarly, the L-H power threshold may be lowered by one mechanism and raised by another, and yet their combination may not equal a net-zero effect.

Recommendations for Future Work

Although these regressions point to a certain reduction/increase in the power threshold via 3D fields, it is difficult to isolate a single-n resonant or non-resonant field in reality. Tailoring the applied perturbations to be predominantly one or the other and seeing the effect would be an interesting experiment. Furthermore, calculating the E_r profiles along with evaluating the plasma response to the perturbations would be a good step toward a more physics-rooted approach to evaluating the RMPs for this database. Seeing the differences on a database scale between the

distributions of efficiencies and magnitudes would also be valuable. To further increase the fidelity of many parameters in the database, a set of representative profiles can be constructed and fed to TRANSP, as was done in [66].

If the regression is to be believed, n=1 EFC fields may be increasing the L-H power threshold considerably. [67] shows a non-negligible radial field as a result of field errors and EFC. Determining if there are strong resonant or non-resonant components from the EFC coils and exploring how perfect the EFC is on DIII-D is a logical next step. It should be noted that empirically determined EFC algorithms are known not to correlate with the cancellation of the error fields in the SURFMN vacuum model.

As shown, the non-monotonic density dependence is sensitive to many parameters which makes it difficult to assess the effect of 3D fields. A dedicated study where as many relevant plasma parameters are fixed as possible (Ip, heating power and scheme, etc.) and scans of the toroidal mode and magnitude are performed would give further insight.

Exceptions to the L-H power threshold scaling, both this one and the Martin's, offer great opportunities for a closer inspection as to why these discharges either took many times more or many times less the predicted power to transition. Already great candidates are the discharges marked with a '1' confidence level in this database. In these discharges, the power is either constant at the transition (signifying some other parameter triggers the transition), or there has been an extended time (~200ms) between the last power increase.

Comparing future DIII-D L-H transitions to this scaling to determine its robustness in relation to the Martin scaling is also of interest. In figure 36 it is shown that a majority of the unconditioned database falls within the points used for the regression. These "unconditioned" points only have three criteria: no double null, favorable ion ∇B drift direction, and deuterium

plasmas only, compared to the 9 used in the Martin scaling. The usefulness of this is questionable, as the importance of predicting the power threshold in a machine that has plenty of auxiliary power, like DIII-D, is unclear. As an extension of this work, comparing this scaling to transitions seen in similar machines (COMPASS and AUG) would give insight into the failures of restricting the regression to only DIII-D. Ideally, the principle of similarity should be exploited for future regressions. Creating a database of discharges that are matched in all dimensionless parameters may offer more insight

Appendix

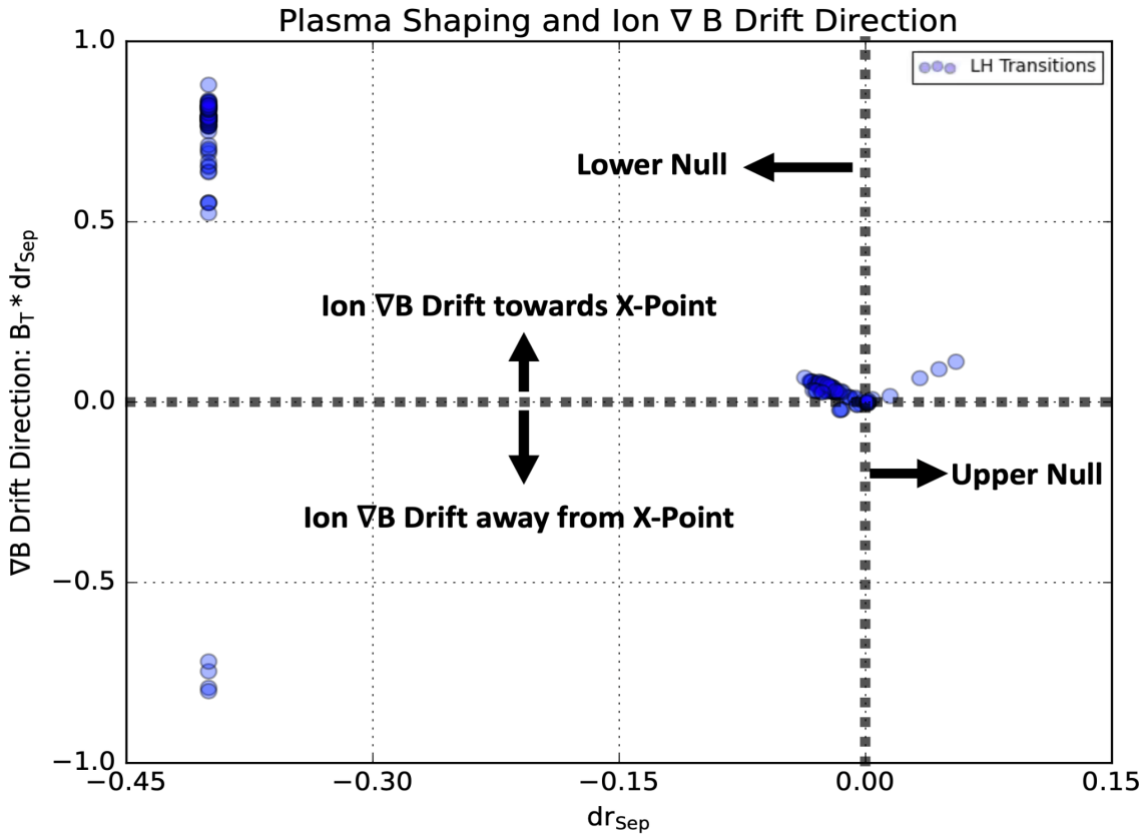

Figure 40: Table used to sort between upper, lower, and double null configurations as well as determine the ion drift direction. The transitions used in this study are all above the zero line on the y-axis.

OMFIT: The "One modeling framework for integrated tasks (OMFIT) is a comprehensive integrated modeling framework which has been developed to enable physics codes to interact in complicated workflows, and support scientists at all stages of the modeling cycle. The OMFIT development follows a unique bottom-up approach, where the framework design and capabilities organically evolve to support progressive integration of the components that are required to accomplish physics goals of increasing complexity." [51].

TokSearch: A “tool in the General Atomics TokSys control design and analysis suite. This tool provides the ability to rapidly perform arbitrary, parallelized queries of archived tokamak shot data (both raw and analyzed) over large numbers of shots. The TokSearch query API borrows concepts from SQL, and users can choose to implement queries in either MATLAB or Python.” [50].

References

[1] U.S. Energy Inform. Administration. Annual Energy Review, Appendix E1. 2011. url: https: //www.eia.gov/totalenergy/data/monthly/pdf/sec12_24.pdf

[2] Chen, F. (2016). *Introduction to Plasma Physics and Controlled Fusion*. Cham Springer International Publishing.

[3] Wesson, J., & Campbell, D. J. (2011). *Tokamaks*. Oxford University Press.

[4] Lawson, J. D. (1957). Some Criteria for a Power Producing Thermonuclear Reactor. *Proceedings of the Physical Society. Section B*, *70*(1), 6–10. https://doi.org/10.1088/0370-1301/70/1/303

[5] Phillips, J. E., & Easterly, C. E. (1980, December 1). *Sources of tritium*. Www.osti.gov. https://www.osti.gov/servlets/purl/6867774

[6] Kitsunezaki, A., Shimizu, M., Ninomiya, H., & Kuriyama, M. (2002). JT-60 Program. *Fusion Science and Technology*, *42*(2-3), 179–184. https://doi.org/10.13182/fst02-a226

[7] Peacock, N. J., Robinson, D. C., Forrest, M. J., Wilcock, P. D., & Sannikov, V. V. (1969). Measurement of the Electron Temperature by Thomson Scattering in Tokamak T3. *Nature*, *224*(5218), 488–490. https://doi.org/10.1038/224488a0

[8] Strait, E. J., & DIII-D Team. (2009). DIII-D research in support of ITER. *Nuclear Fusion*, *49*, 104008. https://doi.org/10.1088/0029-5515/49/10/104008

[9] *ITER - the way to new energy*. (n.d.). ITER. https://www.iter.org

[10] Creely, A. J., Greenwald, M. J., Ballinger, S. B., Brunner, D., Canik, J., Doody, J., Fülöp, T., Garnier, D. T., Granetz, R., Gray, T. K., Holland, C., Howard, N. T., Hughes, J. W., Irby, J. H., Izzo, V. A., Kramer, G. J., Kuang, A. Q., LaBombard, B., Lin, Y., & Lipschultz, B. (2020). Overview of the SPARC tokamak. *Journal of Plasma Physics*, *86*(5). https://doi.org/10.1017/s0022377820001257

[11] Greenwald, M., Terry, J. L., Wolfe, S. M., Ejima, S., Bell, M. G., Kaye, S. M., & Neilson, G. H. (1988). A new look at density limits in tokamaks. *Nuclear Fusion*, *28*(12), 2199–2207. https://doi.org/10.1088/0029-5515/28/12/009

[12] Wagner, F., Becker, G., Behringer, K., Campbell, D., Eberhagen, A., Engelhardt, W., Fussmann, G., Gehre, O., Gernhardt, J., Gierke, G. v., Haas, G., Huang, M., Karger, F., Keilhacker, M., Klüber, O., Kornherr, M., Lackner, K., Lisitano, G., Lister, G. G., & Mayer, H. M. (1982). Regime of Improved Confinement and High Beta in Neutral-Beam-Heated Divertor Discharges of the ASDEX Tokamak. *Physical Review Letters*, *49*(19), 1408–1412. https://doi.org/10.1103/physrevlett.49.1408

[13] Burrell, K. H., Ejima, S., Schissel, D. P., Brooks, N. H., Callis, R. W., Carlstrom, T. N., Colleraine, A. P., DeBoo, J. C., Fukumoto, H., Groebner, R. J., Hill, D. N., Hong, R.-M. ., Hosogane, N., Jackson, G. L., Jahns, G. L., Janeschitz, G., Kellman, A. G., Kim, J., Lao, L. L., & Lee, P. (1987). Observation of an improved energy-confinement regime in neutral-beam–heated divertor discharges in the DIII-D tokamak. *Physical Review Letters*, *59*(13), 1432–1435. https://doi.org/10.1103/physrevlett.59.1432

[14] Evans, T. E., Orlov, D. M., Wingen, A., Wu, W., Loarte, A., Casper, T. A., Schmitz, O., Saibene, G., Schaffer, M. J., & Daly, E. (2013). 3D vacuum magnetic field modelling of the ITER ELM control coil during standard operating scenarios. *Nuclear Fusion*, *53*(9), 093029. https://doi.org/10.1088/0029-5515/53/9/093029

[15] Evans, T. E., Moyer, R. A., Thomas, P. R., Watkins, J. G., Osborne, T. H., Boedo, J. A., Doyle, E. J., Fenstermacher, M. E., Finken, K. H., Groebner, R. J., Groth, M., Harris, J. H., La Haye, R. J., Lasnier, C. J., Masuzaki, S., Ohyabu, N., Pretty, D. G., Rhodes, T. L., Reimerdes, H., & Rudakov, D. L. (2004). Suppression of large edge-localized modes in high-confinement DIII-D plasmas with a stochastic magnetic boundary. *Physical Review Letters*, *92*(23), 235003. https://doi.org/10.1103/PhysRevLett.92.235003

[16] Masline, R., Bykov, I., Moyer, R. A., Orlov, D. M., Wingen, A., Guterl, J., Rudakov, D. L., Wampler, W. R., Wang, H. Q., & Watkins, J. (2022). Misalignment of magnetic field in DIII-D assessed by post-mortem analysis of divertor targets. *Nuclear Fusion*. https://doi.org/10.1088/1741-4326/ac9cf1

[17] Malkov, M. A., Diamond, P. H., Miki, K., Rice, J. E., & Tynan, G. R. (2015). Linking the micro and macro: L-H transition dynamics and threshold physics. *Physics of Plasmas*, *22*(3), 032506. https://doi.org/10.1063/1.4914934

[18] Wagner, F. (2007). A quarter-century of H-mode studies. *Plasma Physics and Controlled Fusion*, *49*(12B), B1–B33. https://doi.org/10.1088/0741-3335/49/12b/s01

[19] Tynan, G. R., Cziegler, I., Diamond, P. H., Malkov, M., Hubbard, A., Hughes, J. W., Terry, J. L., & Irby, J. H. (2016). Recent progress towards a physics-based understanding of the H-mode transition. *Plasma Physics and Controlled Fusion*, *58*(4), 044003. https://doi.org/10.1088/0741-3335/58/4/044003

[20] Biglari, H., Diamond, P. H., & Terry, P. W. (1990). Influence of sheared poloidal rotation on edge turbulence. *Physics of Fluids B: Plasma Physics*, *2*(1), 1–4. https://doi.org/10.1063/1.859529

[21] Ryter, F., Barrera Orte, L., Kurzan, B., McDermott, R. M., Tardini, G., Viezzer, E., Bernert, M., & Fischer, R. (2014). Experimental evidence for the key role of the ion heat channel in the physics of the L–H transition. *Nuclear Fusion*, *54*(8), 083003. https://doi.org/10.1088/0029-5515/54/8/083003

[22] Schmitz, L., Kriete, D. M., Wilcox, R. S., Rhodes, T. L., Zeng, L., Yan, Z., McKee, G. R., Evans, T. E., Paz-Soldan, C., Gohil, P., Lyons, B., Petty, C. C., Orlov, D., & Marinoni, A. (2019). *L–H* transition trigger physics in ITER-similar plasmas with applied $n = 3$ magnetic perturbations. *Nuclear Fusion*, *59*(12), 126010. https://doi.org/10.1088/1741-4326/ab36bf

[23] Gohil, P., Evans, T. E., Fenstermacher, M. E., Ferron, J. R., Osborne, T. H., Park, J. M., Schmitz, O., Scoville, J. T., & Unterberg, E. A. (2011). L–H transition studies on DIII-D to determine H-mode access for operational scenarios in ITER. *Nuclear Fusion*, *51*(10), 103020. https://doi.org/10.1088/0029-5515/51/10/103020

[24] Xu, G., Lin, X., Yang, Q., Wang, Y., Jia, G., Li, N., Yan, N., Chen, R., Xu, X., Guo, H., Wang, L., Zang, Q., Zhang, T., Jin, Y., & Wan, B. (n.d.). *Small-ELM-regime access facilitated by new tungsten divertor on EAST*. Retrieved October 26, 2022, from https://indico.fusenet.eu/event/28/contributions/264/attachments/278/635/EPSpaper2022-Xu.pdf

[25] Yan, Z., Mckee, G. R., Gohil, P., Schmitz, L., Holland, C., Haskey, S. R., Grierson, B. A., Ke, R., Rhodes, T., & Petty, C. (2019). Safety factor and turbulence dynamics dependence of the L-H power threshold on DIII-D. *Physics of Plasmas*, *26*(6), 062507. https://doi.org/10.1063/1.5091701

[26] McKee, G. R., Gohil, P., Schlossberg, D. J., Boedo, J. A., Burrell, K. H., deGrassie, J. S., Groebner, R. J., Moyer, R. A., Petty, C. C., Rhodes, T. L., Schmitz, L., Shafer, M. W., Solomon, W. M., Umansky, M., Wang, G., White, A. E., & Xu, X. (2009). Dependence of the L- to H-mode power threshold on toroidal rotation and the link to edge turbulence dynamics. *Nuclear Fusion*, *49*(11), 115016. https://doi.org/10.1088/0029-5515/49/11/115016

[27] Gohil, P., Jernigan, T. C., Osborne, T. H., Scoville, J. T., & Strait, E. J. (2010). The torque dependence of the H-mode power threshold in hydrogen, deuterium and helium plasmas in DIII-D. *Nuclear Fusion*, *50*(6), 064011. https://doi.org/10.1088/0029-5515/50/6/064011

[28] Andrew, Y., Hawkes, N. C., O'Mullane, M. G., Sartori, R., Baar, M. de, Coffey, I., Guenther, K., Jenkins, I., Korotkov, A., Lomas, P., Matthews, G. F., Matilal, A., Prentice, R., Stamp, M., Strachan, J., Vries, P. de, & Contributors, J. E. (2004). JET divertor geometry and plasma shape effects on the L–H transition threshold. *Plasma Physics and Controlled Fusion*, *46*(5A), A87–A93. https://doi.org/10.1088/0741-3335/46/5a/009

[29] Andrew, Y., Bähner, J.-P., Battle, R., & Jirman, T. (2019). H-Mode Power Threshold Studies on MAST. *Plasma*, *2*(3), 328–338. https://doi.org/10.3390/plasma2030024

[30] Schmitz, L. (2022, July).

[31] Carlstrom, T. N., & Groebner, R. J. (1996). Study of the conditions for spontaneous H(high)-mode transitions in DIII-D. *Physics of Plasmas*, *3*(5), 1867–1874. https://doi.org/10.1063/1.871982

[32] Yan, Z., McKee, G., Kriete, D. M., Schmitz, L., Gohil, P., Holland, C., Haskey, S. R., Grierson, B. A., Wilcox, R., Rhodes, T., & Petty, C. (2021). Turbulence Flow Dynamics and Mode Structure Impacts on the L-H Transition [Review of *Turbulence Flow Dynamics and Mode Structure Impacts on the L-H Transition*]. In *28th IAEA Fusion Energy Conference*.

[33] Ryter, F., Rathgeber, S. K., Barrera Orte, L., Bernert, M., Conway, G. D., Fischer, R., Happel, T., Kurzan, B., McDermott, R. M., Scarabosio, A., Suttrop, W., Viezzer, E., Willensdorfer, M., & Wolfrum, E. (2013). Survey of the H-mode power threshold and transition physics studies in ASDEX Upgrade. *Nuclear Fusion*, *53*(11), 113003. https://doi.org/10.1088/0029-5515/53/11/113003

[34] Ma, Y., Hughes, J. W., Hubbard, A. E., LaBombard, B., Churchill, R. M., Golfinopolous, T., Tsujii, N., & Marmar, E. S. (2012). Scaling of H-mode threshold power and L–H edge conditions with favourable ion grad-*B*drift in Alcator C-Mod tokamak. *Nuclear Fusion*, *52*(2), 023010. https://doi.org/10.1088/0029-5515/52/2/023010

[35] Willensdorfer, M., Plank, U., Brida, D., Cavedon, M., Conway, G. D., Ryan, D. A., Suttrop, W., Buchholz, R., Dunne, M., Fischer, R., Griener, M., Hobirk, J., Kasilov, S., Kirk, A., McDermott, R. M., Pütterich, T., Tardini, G., & Yu, Q. (2022). Dependence of the L–H power threshold on the alignment of external non-axisymmetric magnetic perturbations in ASDEX Upgrade. *Physics of Plasmas*, *29*(3), 032506. https://doi.org/10.1063/5.0073841

[36] Connor, J. W., & Wilson, H. R. (1999). A review of theories of the L-H transition. *Plasma Physics and Controlled Fusion*, *42*(1), R1–R74. https://doi.org/10.1088/0741-3335/42/1/201

[37] Fundamenski, W., Militello, F., Moulton, D., & McDonald, D. C. (2012). A new model of the L–H transition in tokamaks. *Nuclear Fusion*, *52*(6), 062003. https://doi.org/10.1088/0029-5515/52/6/062003

[38] Martin, Y. R., Takizuka, T., & Group, the I. C. H-mode. T. D. (2008). Power requirement for accessing the H-mode in ITER. *Journal of Physics: Conference Series*, *123*, 012033. https://doi.org/10.1088/1742-6596/123/1/012033

[39] Shimada, M., Campbell, D. J., Mukhovatov, V., Fujiwara, M., Kirneva, N., Lackner, K., Nagami, M., Pustovitov, V. D., Uckan, N., Wesley, J., Asakura, N., Costley, A. E., Donné, A. J. H., Doyle, E. J., Fasoli, A., Gormezano, C., Gribov, Y., Gruber, O., Hender, T. C., & Houlberg, W. (2007). Chapter 1: Overview and summary. *Nuclear Fusion*, *47*(6), S1–S17. https://doi.org/10.1088/0029-5515/47/6/s01

[40] Hughes, J. (2020, November).

[41] Leonard, A. W., Meyer, W. H., Geer, B., Behne, D. M., & Hill, D. N. (1995). 2D tomography with bolometry in DIII-D[a)]. *Review of Scientific Instruments*, *66*(2), 1201–1204. https://doi.org/10.1063/1.1146006

[42] St. John, H and Taylor, T S and Lin-Liu, Y R and Turnbull, A D, Plasma Physics and Controlled Nuclear Fusion Research, vol. 3, p. 603 (1994)

[43] Matthews, G. F. (2013). Plasma operation with an all metal first-wall: Comparison of an ITER-like wall with a carbon wall in JET. *Journal of Nuclear Materials*, *438*, S2–S10. https://doi.org/10.1016/j.jnucmat.2013.01.282

[44] Maggi, C. F., Weisen, H., Hillesheim, J. C., Chankin, A., Delabie, E., Horvath, L., Auriemma, F., Carvalho, I. S., Corrigan, G., Flanagan, J., Garzotti, L., Keeling, D., King, D., Lerche, E., Lorenzini, R., Maslov, M., Menmuir, S., Saarelma, S., Sips, A. C. C., & Solano, E. R. (2017). Isotope effects on L-H threshold and confinement in tokamak plasmas Related content Explaining the isotope effect on heat transport in L-mode with the collisional electron-ion energy exchange. *Plasma Physics and Controlled Fusion*, *60*(1). https://doi.org/10.1088/1361-6587/aa9901

[45] Breslau, J., Gorelenkova, M., Poli, F., Sachdev, J., Pankin, A., Perumpilly, G., Yuan, X., & Glant, L. (2018, June 27). *TRANSP*. Www.osti.gov. https://www.osti.gov/biblio/1489900

[46] White, R. B., & Chance, M. S. (1984). Hamiltonian guiding center drift orbit calculation for plasmas of arbitrary cross section. *Physics of Fluids*, *27*(10), 2455. https://doi.org/10.1063/1.864527

[47] Van Zeeland, M. A., Ferraro, N. M., Grierson, B. A., Heidbrink, W. W., Kramer, G. J., Lasnier, C. J., Pace, D. C., Allen, S. L., Chen, X., Evans, T. E., García-Muñoz, M., Hanson, J. M., Lanctot, M. J., Lao, L. L., Meyer, W. H., Moyer, R. A., Nazikian, R., Orlov, D. M., Paz-Soldan, C., & Wingen, A. (2015). Fast ion transport during applied 3D magnetic perturbations on DIII-D. *Nuclear Fusion*, *55*(7), 073028. https://doi.org/10.1088/0029-5515/55/7/073028

[48] Weiland, M., Bilato, R., Collins, C. S., Heidbrink, W. W., Liu, D., & Van Zeeland, M. A. (2019). Simulation of neutron emission in neutral beam injection heated plasmas with the real-time code RABBIT. *Nuclear Fusion*, *59*(8), 086002. https://doi.org/10.1088/1741-4326/ab1edd

[49] Garcia-Munoz, M., Äkäslompolo, S., Asunta, O., Boom, J., Chen, X., Classen, I. G. J., Dux, R., Evans, T. E., Fietz, S., Fisher, R. K., Fuchs, C., Geiger, B., Hoelzl, M., Igochine, V., Jeon, Y. M., Kim, J., Kim, J. Y., Kurzan, B., Lazanyi, N., & Lunt, T. (2013). Fast-ion redistribution and loss due to edge perturbations in the ASDEX Upgrade, DIII-D and

KSTAR tokamaks. *Nuclear Fusion*, *53*(12), 123008. https://doi.org/10.1088/0029-5515/53/12/123008

[50] Sammuli, B. S., Barr, J. L., Eidietis, N. W., Olofsson, K. E. J., Flanagan, S. M., Kostuk, M., & Humphreys, D. A. (2018). TokSearch: A search engine for fusion experimental data. *Fusion Engineering and Design*, *129*, 12–15. https://doi.org/10.1016/j.fusengdes.2018.02.003

[51] Meneghini, O., Smith, S. P., Lao, L. L., Izacard, O., Ren, Q., Park, J. M., Candy, J., Wang, Z., Luna, C. J., Izzo, V. A., Grierson, B. A., Snyder, P. B., Holland, C., Penna, J., Lu, G., Raum, P., McCubbin, A., Orlov, D. M., Belli, E. A., & Ferraro, N. M. (2015). Integrated modeling applications for tokamak experiments with OMFIT. *Nuclear Fusion*, *55*(8), 083008. https://doi.org/10.1088/0029-5515/55/8/083008

[52] Colchin, R. J., Hillis, D. L., Maingi, R., Klepper, C. C., & Brooks, N. H. (2003). The Filterscope. *Review of Scientific Instruments*, *74*(3), 2068–2070. https://doi.org/10.1063/1.1537038

[53] Grierson, B. A., Burrell, K. H., Crowley, B., Grisham, L., & Scoville, J. T. (2014). High speed measurements of neutral beam turn-on and impact of beam modulation on measurements of ion density. *Review of Scientific Instruments*, *85*(10), 103502. https://doi.org/10.1063/1.4896514

[54] Lao, L. L., St. John, H., Stambaugh, R. D., Kellman, A. G., & Pfeiffer, W. (1985). Reconstruction of current profile parameters and plasma shapes in tokamaks. *Nuclear Fusion*, *25*(11), 1611–1622. https://doi.org/10.1088/0029-5515/25/11/007

[55] Kostuk, M., Uram, T. D., Evans, T., Orlov, D. M., Papka, M. E., & Schissel, D. (2018). Automatic Between-Pulse Analysis of DIII-D Experimental Data Performed Remotely on a Supercomputer at Argonne Leadership Computing Facility. *Fusion Science and Technology*, *74*(1-2), 135–143. https://doi.org/10.1080/15361055.2017.1390388

[56] Schaffer, M. J., Menard, J. E., Aldan, M. P., Bialek, J. M., Evans, T. E., & Moyer, R. A. (2008). Study of in-vessel nonaxisymmetric ELM suppression coil concepts for ITER. *Nuclear Fusion*, *48*(2), 024004. https://doi.org/10.1088/0029-5515/48/2/024004

[57] Ferraro, N. M. (2012). Calculations of two-fluid linear response to non-axisymmetric fields in tokamaks. *Physics of Plasmas*, *19*(5), 056105. https://doi.org/10.1063/1.3694657

[58] Gohil, P., Burrell, K. H., & Carlstrom, T. N. (1998). Parametric dependence of the edge radial electric field in the DIII-D tokamak. *Nuclear Fusion*, *38*(1), 93–102. https://doi.org/10.1088/0029-5515/38/1/308

[59] Righi, E., Bartlett, D. V., Christiansen, J. P., Conway, G. D., Cordey, J. G., Eriksson, L.-G., Esch, H. P. L. D., Fishpool, G. M., Gowers, C. W., Haas, J. C. M. de, Harbour, P. J., Hawkes, N. C., Jacquinot, J., Jones, T. T. C., Kerner, W., King, Q. A., Lowry, C. G.,

Monk, R. D., Nielsen, P., & Rimini, F. G. (1999). Isotope scaling of the H mode power threshold on JET. *Nuclear Fusion*, *39*(3), 309–319. https://doi.org/10.1088/0029-5515/39/3/302

[60] Luce, T. C. (2013). An analytic functional form for characterization and generation of axisymmetric plasma boundaries. *Plasma Physics and Controlled Fusion*, *55*(9), 095009. https://doi.org/10.1088/0741-3335/55/9/095009

[61] Orlov, D. M., Moyer, R. A., Evans, T. E., Wingen, A., Buttery, R. J., Ferraro, N. M., Grierson, B. A., Eldon, D., Watkins, J. G., & Nazikian, R. (2014). Comparison of the numerical modelling and experimental measurements of DIII-D separatrix displacements during H-modes with resonant magnetic perturbations. *Nuclear Fusion*, *54*(9), 093008. https://doi.org/10.1088/0029-5515/54/9/093008

[62] L. Schmitz , Z. Yan, L. Zeng, P.H. Diamond,G.R. McKee, C. S. Chang, T.L. Rhodes, B. Wilcox, C. Paz-Soldan, T.E. Evans, B. Lyons, D. Orlov, S. Haskey, P. Gohil, B. Grierson, C.C Petty. UCSD/UCLA/UCI Plasma Seminar December 1, 2020

[63] Lao, L. L., Brennan, D. P., Chu, M. S., Evans, T. E., La Haye, R. J., Luxon, J. L., Luce, T. C., Petrie, T. W., Schaffer, M. J., Strait, E. J., Taylor, T. S., Wade, M. R., & You, K. I. (2003). SEPARATRIX LOCATION AND ERROR FIELD [Review of *Separatrix Location and Error Field*]. In *Post-APS Error Magnetic Field Workshop*.

[64] Fedorczak, N., Diamond, P. H., Tynan, G., & Manz, P. (2012). Shear-induced Reynolds stress at the edge of L-mode tokamak plasmas. *Nuclear Fusion*, *52*(10), 103013. https://doi.org/10.1088/0029-5515/52/10/103013

[65] Manz, P., Stegmeir, A., Schmid, B., Ribeiro, T. T., Birkenmeier, G., Fedorczak, N., Garland, S., Hallatschek, K., Ramisch, M., & Scott, B. D. (2018). Magnetic configuration effects on the Reynolds stress in the plasma edge. *Physics of Plasmas*, *25*(7), 072508. https://doi.org/10.1063/1.5037511

[66] Grierson, B. A., Van Zeeland, M. A., Scoville, J. T., Crowley, B., Bykov, I., Park, J. M., Heidbrink, W. W., Nagy, A., Haskey, S. R., & Liu, D. (2021). Testing the DIII-D co/counter off-axis neutral beam injected power and ability to balance injected torque. *Nuclear Fusion*, *61*(11), 116049. https://doi.org/10.1088/1741-4326/ac2872

[67] Wilks, T. M., Stacey, W. M., & Evans, T. E. (2013). Analysis of toroidal phasing of resonant magnetic perturbation effects on edge transport in the DIII-D tokamak. *Physics of Plasmas*, *20*(5), 052505. https://doi.org/10.1063/1.4804350